A New Method
of Determining the Reversible Magnetization Loop
# of Bulk High-Temperature Superconductors

Yu. S. Ermolaev and I. A. Rudnev

Moscow Engineering Physics Institute (State University), Moscow, 115409 Russia
Received February 27, 2004

Abstract—A new method of calculation of the magnetization loop of bulk high-temperature superconductors is proposed which employs the results of measurements of the magnetic levitation force. © *2004 MAIK "Nauka/Interperiodica".*

Recently, there has been increasing interest in developing applications of bulk high-temperature superconductors (HTSCs) such as magnetic bearings, energy storage systems, magnetic suspension systems, and superconducting magnets [1–3]. For designing and operating such systems, it is necessary to know a number of HTSC parameters. This poses a problem of developing methods for rapid and reliable determination of the properties of HTSCs, since the traditional techniques used for measuring the critical temperatures, critical currents, and magnetizations of bulk HTSCs encounter considerable difficulties.

Below, we describe a new method for rapid and reliable evaluation of the reversible magnetization loop of bulk HTSCs using the results of measurements of the levitation force.

The proposed method is based on the comparison of experimental and calculated dependences of the magnetic levitation force on the distance between a superconductor and a permanent magnet. The algorithm of calculation of the magnetic levitation force will be described first for two limiting cases (complete diamagnetism and complete flux trapping) and then for an intermediate case, which will allow a partly trapped field to be calculated using the experimentally measured levitation force. Then, a comparison of the experimental and calculated dependences will be used for determining the distribution of currents in the superconductor and calculating the magnetization due to a field of these currents.

The calculations will be performed for a real configuration comprising a magnet and a coaxial cylindrical superconductor of greater radius spaced by the distance z. The permanent NdFeB magnet used in our experiments had the following characteristics: radius, $R = 7 \times 10^{-3}$ m; height, $d = 8 \times 10^{-3}$ m; surface current,

$J_{\mathrm{m}} = 9.6 \times 10^5$ A/m. The last value was determined by measuring the force of interaction between two magnets spaced $(1.5–3.0) \times 10^{-4}$ cm apart, having almost coinciding axes of symmetry.

In the calculation, the permanent magnet is considered as a cylindrical surface of radius R and height h carrying a current with linear density J_{m}. The corresponding magnetic field is determined using the Biot–Savard relation. The subsequent calculations of forces will use the radial component of this magnetic field:

$$H_r(r, z) = \frac{1}{4\pi} J_{\mathrm{m}} R \int_0^{2\pi} \cos(\varphi)$$
$$\times \sum_{k=0}^{1} (1 - 2k)((z + kd)^2 + r^2 + R^2 - 2rR\cos(\varphi))^{-1/2} d\varphi, \quad (1)$$

where r is the distance from the symmetry axis of the system.

The calculation of magnetization will require the field at the axis:

$$H_z(z)$$
$$= \frac{1}{2} J_{\mathrm{m}} \sum_{k=0}^{1} ((2k - 1)z + kd)((z + kd)^2 + R^2)^{-1/2}. \quad (2)$$

Let us calculate the distribution of currents induced in the superconductor. The total current J_φ consists of two components: the shield current ($J_{\varphi \text{ shield}}$) and the current corresponding to the trapped field ($J_{\varphi \text{ trapped}}$). The former current and the force of its interaction with the applied field are determined using the method described in [4]. In order to simplify the
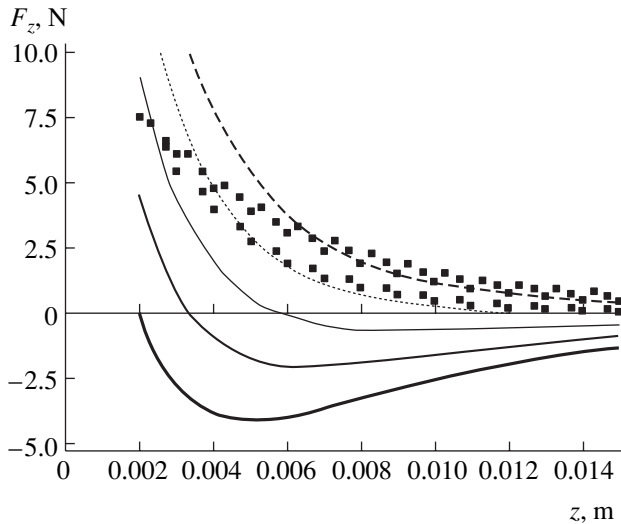
Fig. 1. A family of $F_z(z, \alpha)$ curves calculated for various values of the parameter α (top to bottom): 0; 0.25; 0.5; 0.75; and 1. Black squares present experimental $F_z(z)$ values determined in several cycles of measurements of the magnetic levitation force (only every third experimental point is plotted).
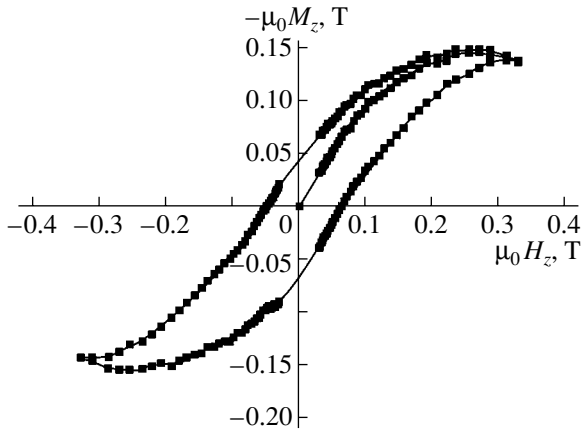

Fig. 2. Plot of the magnetization versus applied field calculated by formula (4) using the data presented in Fig. 1.

calculation, the superconductor is approximated by a flat surface of infinite radius. Since the real superconductor radius was 2.5 times that of the magnet, this approximation virtually does not reduce the accuracy of calculations.

The shield current induced on the superconductor surface has the linear density $J_{\varphi\,shield}(r, z) = 2H_r(r, z)$. This value corresponds to the condition of field discontinuity on the surface of a superconductor occurring in the Meissner state, whereby the field inside the superconductor is $B = 0$ and that outside is $B_r = 2\mu_0 H_r$, where $\mu_0 = 4\pi \times 10^{-7}$ N/m is the magnetic constant.

The current corresponding to the trapped field is described in terms of the maximum applied field (the maximum field that can be trapped by a superconductor): $J_{\varphi\,trapped}(r) = -2H_r(r, z_0)\alpha$, where z_0 is the minimum distance between magnet and superconductor (in our case, $z_0 = 2 \times 10^{-3}$ m). The coefficient α is an important parameter in our calculations which determines the trapped field as a fraction of the maximum possible value. This description of the trapped field is used for the following reasons:

(i) the force of interaction between a current and an applied field is readily determined using the Ampère law;

(ii) use of the linear current density does not require analysis of the trapped field distribution in depth of the superconductor;

(iii) the superconductor cooled in the absence of a magnetic field (zero-field cooling) has no trapped field and $\alpha = 0$;

(iv) when the superconductor is cooled in a magnetic field (at a distance of z_0), the force (and, hence, J_{φ}) is zero, which holds for $\alpha = 1$.

The interaction between the current J_{φ} and an applied field at each point of the superconductor surface is described by the Ampère law, and the total force is determined by integrating over the entire surface:

$$
\begin{aligned}
F_z(z) &= 2\pi\mu_0 \int_0^\infty J_{\varphi}(r, z) H_r(r, z) r\,dr \\
&= 2\pi\mu_0 \int_0^\infty (H_r(r, z) - H_r(r, z_0)\alpha) H_r(r, z) r\,dr.
\end{aligned}
\tag{3}
$$

The value of α is determined from the condition that the calculated total force $F_z(z)$ is equal to the value $F_{z\,exp}(z)$ measured in experiment: $F_z(z, \alpha) = F_{z\,exp}(z)$. Figure 1 shows a family of $F_z(z, \alpha)$ curves, calculated for the parameter α varied in the interval $0 < \alpha < 1$, in comparison to the experimental data obtained in several cycles of measurements of the magnetic levitation force as a function of the distance z.

In the general case, the magnetization is defined as the field of currents J_{φ}. However, since the current J_{φ} (both the shield and trapped-field components) is related to the field discontinuity on crossing the superconductor surface, it is possible to use the expression $\mu_0 M = B - \mu_0 H$, where $B = \alpha\mu_0 H(r, z_0)$ is the field trapped in the superconductor. Since the applied field is inhomogeneous, let us determine the magnetization at the axis of symmetry on the superconductor surface. Expressing α through the experimental force and sub-

stituting it into equations for the field components, we obtain the final expression for the magnetization:

$$\mu_0 M_z = \mu_0 H_z(z_0) \frac{F_{z\,exp}(z) - 4\pi\mu_0 \int\limits_0^\infty H_r^2(r,z)\,r dr}{4\pi\mu_0 \int\limits_0^\infty H_r(r,z) H_r(r,z_0)\,r dr} - \mu_0 H_z(z). \quad (4)$$

We have measured the magnetic levitation force $F_z(z)$ (Fig. 1) as a function of the distance between a permanent magnet and a sample of textured $YBa_2Cu_3O_{7-x}$ ceramics. The measurements were performed using an experimental setup described in [5]. In the course of $F_z(z)$ measurements, the polarity of the magnet was reversed after accomplishing each cycle. Using this procedure, it was possible to calculate the magnetization for the magnetic field varied between negative and positive limits. The results of calculation of the magnetization loop using the proposed algorithm are presented in Fig. 2.

In conclusion, we have described and demonstrated the use of a new method of calculation of the reversible magnetization loop of bulk HTSCs using the results of measurements of the levitation force as a function of the distance between the superconductor and the magnet.

REFERENCES

1. J. R. Hull, Supercond. Sci. Technol. **13**, R1 (2002).
2. N. Koshizuka, F. Ishikawa, and F. Nasu, Physica C **378–381**, 11 (2002).
3. Z. Ren, J. Wang, and S. Wang, Physica C **378–381**, 873 (2002).
4. A. A. Kordyuk, V. V. Nemoshkalenko, and R. V. Viznichenko, Appl. Phys. Lett. **75**, 1595 (1999).
5. Yu. S. Ermolaev and I. A. Rudnev, Prib. Tekh. Éksp. **47** (2004) (submitted).

Translated by P. Pozdeev

Modeling the Behavior of Complex Media by Jointly Using Discrete and Continuum Approaches

S. G. Psakhie, A. Yu. Smolin*, Yu. P. Stefanov, P. V. Makarov, and M. A. Chertov

Institute of Strength Physics and Materials Science, Siberian Division, Russian Academy of Sciences, Tomsk, 634055 Russia

* e-mail: asmolin@ispms.tsc.ru

Received March 1, 2004

Abstract—We propose a new approach to modeling the behavior of heterogeneous media, according to which such objects are represented as composed of regions of two types, one being described within the framework of a discrete, and the other, a continuum approach. This joint approach is promising for the numerical modeling of complex media with strongly different properties of components. Possibilities of the proposed method were verified by studying the propagation of elastic waves in a two-component medium with a discrete component, modeled by the method of movable cellular automata, and a continuum component described by a system of equations of motion of continuum solved by the finite difference method. The results of calculations show that this approach provides adequate description of the propagation of elastic waves in complex media and does not introduce nonphysical distortions at the boundaries where the two models are matched. © *2004 MAIK "Nauka/Interperiodica".*

Investigation of the laws governing the behavior of complex media under the action of various external factors is necessary for solving many basic, technological, and engineering problems. An important part in such investigations belongs to methods and approaches developed by computational mechanics. For a long time, most numerical methods were based on the approaches developed within the framework of the mechanics of continuum. It should be noted that application of the methods of continuum mechanics to description of the process of deformation encounters considerable difficulties in the presence of local straining, discontinuities, intense vortex deformations, and agitation of masses. These problems are especially significant in the case of highly porous and heterogeneous materials and composites with strongly different properties of components.

Discrete approaches capable of explicitly modeling the processes involving agitation of masses were developed predominantly for the investigation of granulated and friable media [1–4], in which the basic elements can be modeled by particles. For this reason, most of these investigations use the equations of motion in the form typical of the method of particles [4] and the interaction forces are calculated within the framework of the model of hard or soft spheres. However, this formalism does not provide correct description of the behavior of continuous isotropic media.

The numerical method of movable cellular automata (MCA) extensively developed in recent years [5–9] is free of this disadvantage. While using a discrete approach, this method is based on the equations of motion, which are different from classical equations. In

particular, it was shown [7] that, when the characteristic automaton size tends to zero, the MCA formalism allows a transition to the relations of continuum mechanics. The main advantage of this method is the possibility of explicitly modeling both the motion of continuous media and the agitation of masses, including the formation of discontinuities of various types (from the generation of individual defects to the main crack propagation). This circumstance for the first time provides prerequisites for jointly using discrete and continuum approaches within the framework of a common computational scheme, thus combining the advantages of both approaches for solving problems related to modeling of complex objects containing explicit zones of intense straining and fracture.

This paper is devoted to the joint use of discrete and continuum approaches, which is important for the development of computational mechanics. The new approach is based on two methods successfully used in recent years. The first method, based on the continuum approach, is the finite difference method of solution of the dynamical problems of elastoplastic deformation of continuous media, and the second is the MCA method based on the discrete description.

Since both methods employed in the proposed approach are well known [5, 6, 10], we will only consider the questions pertaining to their joint use. The model medium (Fig. 1) is considered to be composed of regions of two types—continuous (grid) and discrete (MCA). Each node of the grid, occurring at the boundary (interface) where the two models are matched, is set into correspondence with a certain interfacial automaton (element of the MCA model). In the simplest case,
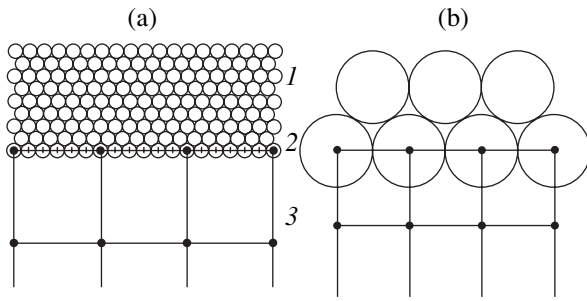
Fig. 1. Matching of the continuous and discrete regions of a model complex medium in the cases when the size of movable cellular automata is (a) smaller than and (b) equal to the grid pitch: (*1*) MCA; (*2*) interface; (*3*) grid.

the automaton size is equal to the grid pitch and there are no additional automata between the interfacial grid nodes.

In order to provide for a correct joint description of consistent behavior of the continuous and discrete regions, it is necessary to ensure continuity of the state parameters on the passage across the interface. In this study, the motion of two models was matched in the step of calculation of the velocities of interfacial nodes. For these nodes, the finite difference equation of motion was written in the form taking into account all forces acting upon the matched interfacial nodes and automata.

The five-step computational algorithm is as follows:

1. Calculate the stress-strained state in the continuous region, including the velocities and coordinates of nodes.

2. Calculate the velocities of interfacial nodes, in contrast to those of the internal nodes, using the equations of motion involving forces acting from the discrete region.

3. Call a subroutine realizing the MCA method, introduce the coordinates and velocities of matched interfacial nodes and automata, and set the integration step.

4. Perform the MCA integration step (for smaller automata, several steps) to calculate the new positions and velocities of all automata, including those matched with interfacial nodes.

5. Introduce new data on the matched interfacial automata into the grid model and set a new time step for the integration.

In order to check for the possibility of jointly using the discrete and continuum approaches within the framework of a common computational scheme and verify the algorithm, we studied the propagation of elastic waves in a two-component medium with a free surface, involving only one linear boundary where the two models have to be matched (Fig. 2). The mechanical characteristics of continuous and discrete media were taken to be identical, so that the medium was formally homogeneous and the interface should not be manifested. It should be noted that numerical methods used in this study were previously successfully applied to description of dynamical processes, including the propagation of elastic waves [8, 9, 11–13].

In the first stage, we considered the propagation of a plane elastic wave with a front parallel to the line of matching. The results of calculations showed that the wave crossing the boundary in both possible directions did not give rise to a reflected wave and the pulse shape was not distorted. This was evidence that the algorithm of joint use of the two methods ensured complete momentum transfer in the absence of shear strain.

In the second stage, we studied a more complicated problem involving the generation and propagation of waves of all types in the medium with a free surface. For this purpose, a region on the surface of an elastic medium occupying a half-space was subjected to a short pulse of a local vertical load. The pulse source was either arranged symmetrically on the line of matching the grid and MCA regions (case 1) or displaced into one of these regions (case 2). We analyzed the detailed
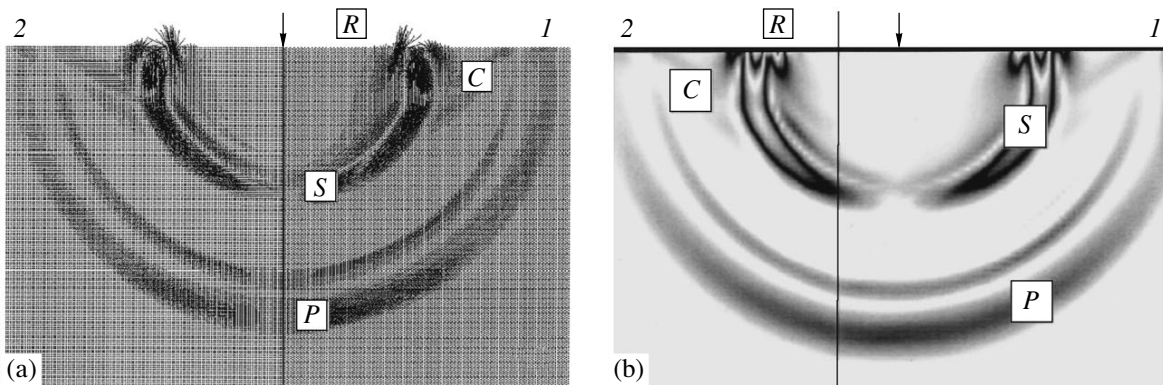

Fig. 2. Wave field patterns observed when the pulse source is (a) arranged symmetrically relative to the interface (indicated by the arrow) and (b) shifted toward the discrete region: (*1*) MCA; (*2*) grid. See the text for explanation.

pattern of propagation of waves of all types and the symmetry of the displacement velocity field. The tests were performed for both square and close (hexagonal) packing of automata in the discrete region.

In both cases, the pulsed action resulted in the formation of longitudinal (P) and transverse (S) waves at a certain distance from the pulse source, which propagated with different velocities (Fig. 2). The presence of the free surface leads to the formation of so-called conical and surface waves. As can be seen in Fig. 2, the conical (C) wave is manifested only in the region where the longitudinal wave interacts with the free surface. The C-wave front extends from the point where the P wave emerges on the surface to the tangency point on the S-wave front. The surface Rayleigh (R) wave propagates at the free surface, lagging slightly behind the S wave. The R wave has an elliptical polarization and rapidly decays with depth.

As is known, the passage of a wave across the interface of two media possessing different mechanical properties or across the surface of discontinuity of displacements (see, e.g., [13]) gives rise to the formation of reflected and refracted waves. In all cases under consideration, the results of our calculations showed no significant distortion of wave fronts (Fig. 2). Nor did we observe significant secondary (reflected, refracted, or conical) waves.

Thus, the results of numerical simulation of the propagation of elastic waves in a combined medium modeled using the continuum and discrete approaches confirmed the possibility of jointly using these methods for description of the elastic behavior of complex media. Good prospects of the proposed approach and algorithms of its realization were confirmed by the results of test calculations, which showed that no artificial or induced effects arise even in cases of complex, dynamically developing elastic displacements in a complex medium with a free surface. The proposed method can be especially useful for solving problems involving numerical simulation of the behavior of complex media with strongly different physical properties of components. Such problems are not only considered in materials science and machine building but also frequently encountered in problems of geomechanics and the mechanics of soils and rocks.

REFERENCES

1. P. A. Cundall and O. D. Strack, Geotechnique **1** (29), 47 (1979).
2. S. Luding, Phys. Rev. E **52**, 4442 (1995).
3. O. R. Walton, Mech. Mater. **16**, 239 (1993).
4. H. J. Herrmann and S. Luding, Continuum Mech. Thermodyn. **10**, 189 (1998).
5. S. G. Psakhie, Y. Horie, S. Yu. Korostelev, *et al.*, Izv. Vyssh. Uchebn. Zaved. Fiz. **38** (11), 58 (1995).
6. S. G. Psakhie, G. P. Ostermeyer, A. I. Dmitriev, *et al.*, Fiz. Mezomekh. **3** (2), 5 (2000).
7. S. G. Psakhie, M. A. Chertov, and E. V. Shil'ko, Fiz. Mezomekh. **3** (3), 93 (2000).
8. S. G. Psakhie, Y. Horie, G. P. Ostermeyer, *et al.*, Theor. Appl. Fract. Mech. **37**, 311 (2001).
9. S. G. Psakhie, V. V. Ruzhich, O. P. Smekalin, *et al.*, Fiz. Mezomekh. **4** (1), 67 (2001).
10. M. L. Wilkins, in *Methods of Computational Physics*, Ed. by B. Alder, S. Fernbach, and M. Rotenberg (Academic, New York, 1964; Mir, Moscow, 1967), pp. 212–263.
11. M. M. Nemirovich-Danchenko and Yu. P. Stefanov, Geol. Geofiz. **36** (11), 96 (1995).
12. Yu. P. Stefanov, Fiz. Mezomekh. **1** (2), 81 (1998).
13. Yu. P. Stefanov, Theor. Appl. Fract. Mech. **34**, 101 (2000).

Translated by P. Pozdeev

The Synthesis and Photoelectric Properties of Si–$(Si_2)_{1-x}(ZnS)_x$ Epitaxial Structures

B. Sapaev and A. S. Saidov

Physicotechnical Institute, "Solar Physics" Research and Production Corporation,
Academy of Sciences of the Republic of Uzbekistan, Tashkent, Uzbekistan
e-mail: amin@physic.uzsci.net
Revised manuscript received January 28, 2004

Abstract—Epitaxial layers of $(Si_2)_{1-x}(ZnS)_x$ ($0.08 \leq x \leq 0.92$) solid solutions were grown by liquid phase epitaxy from a tin-based solution melt confined between two horizontal polycrystalline silicon substrates. The morphology, photoelectric properties, and current–voltage characteristics of the epilayers have been studied. The obtained $(Si_2)_{1-x}(ZnS)_x$ layers exhibit homogeneous depth–concentration profiles of components. The photosensitivity interval extends from 1.05 to 3.0 eV, which makes the obtained structures a promising material for photo- and optoelectronic devices. © *2004 MAIK "Nauka/Interperiodica".*

In recent years, a large number of new chemical compounds and solid solutions possessing semiconductor properties have been synthesized. Most important and promising semiconducting materials for photo- and optoelectronic devices are offered by solid solutions based on the elementary semiconductor Si and the photosensitive compound ZnS.

The high value of these solutions is primarily due to the fact that their bandgap widths can be varied within broad limits, from 1.12 to 3.57 eV. The spectral range of photosensitivity of $(Si_2)_{1-x}(ZnS)_x$ solid solutions extends from infrared to ultraviolet, which allows the electric, photoelectric, and optical characteristics to be controlled in a broad range. It was reported [1] that ZnS:Cu films exhibiting bright blue, green, and yellow photoluminescence were synthesized on glass and ceramic substrates using a chemical nonvacuum deposition method. The emissive properties of these films strongly depend on the copper concentration and the conditions (substrate structure and temperature) of film formation. Recent investigation [2] of the electroluminescent properties of ZnS:Cu layers showed that such films have good prospects for use in electroluminescent displays.

In this context, the growth of ZnS films of cheap silicon substrates and the investigation of properties of such structures is of considerable importance. This paper presents data on the synthesis and properties of electric and photoelectric properties of $(Si_2)_{1-x}(ZnS)_x$ solid solutions grown by liquid phase epitaxy (LPE) from a tin-based solution melt confined between (111)-oriented single crystal silicon substrates (KDB grade) with a resistivity of 1.0–10.0 Ω cm.

Since the obtained epitaxial films were of the *n* type, we selected *p*-type substrates in order to obtain *p–n* heterojunctions. The technology of epitaxial growth from a limited volume of solution melt was described in detail elsewhere [3]. Using this technique, we obtained for the first time epilayers of $(Si_2)_{1-x}(ZnS)_x$ solid solutions by LPE on silicon substrates. Disk-shaped substrates with a thickness of $d \approx 350$–400 μm were cut from a Czochralski grown single crystal ingot with a diameter of $d = 20$ mm and a resistivity of $\rho \approx 1.0$–
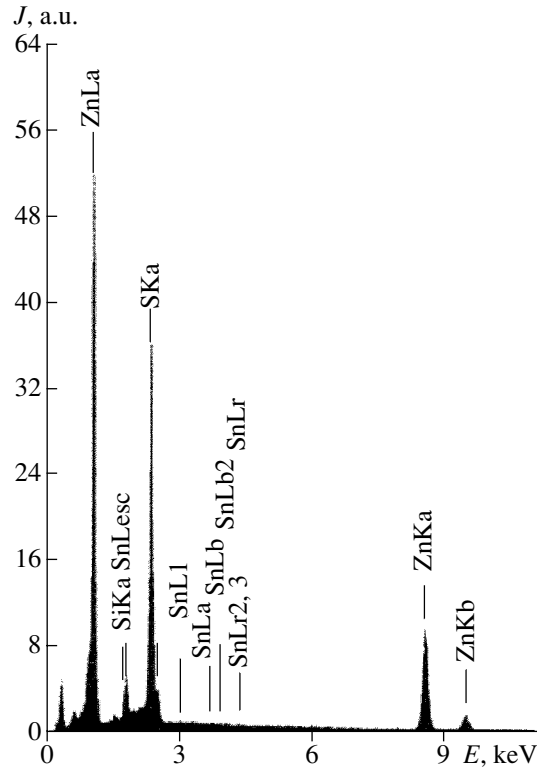

Fig. 1. Surface composition of a $(Si_2)_{1-x}(ZnS)_x$ epilayer by X-ray emission data obtained with a Jeol JSM 5910LV type microprobe.

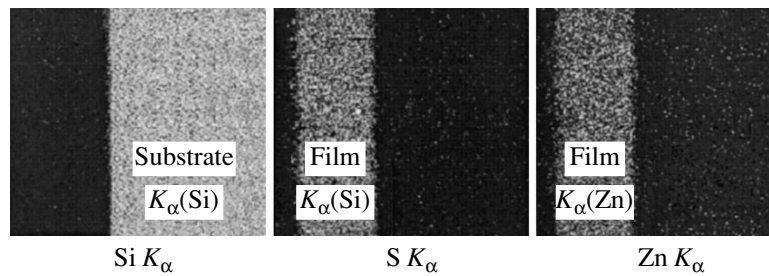**Fig. 2.** Scanning elemental images of cleavages of $(Si_2)_{1-x}(ZnS)_x$ epilayers measured using a Jeol JSM 5910LV type microprobe.
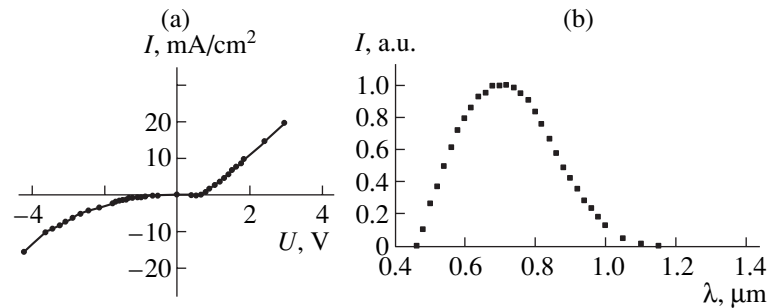

Fig. 3. The typical (a) current–voltage characteristic and (b) photosensitivity spectrum of p-Si–n-$(Si_2)_{1-x}(ZnS)_x$ heterostructures.

10.0 Ω cm. The optimum composition of the solution melt was selected based on the results of preliminary investigation of Si–ZnS solutions and the published data [4, 5]. The films of $(Si_2)_{1-x}(ZnS)_x$ solid solutions were grown from a tin-based solution melt confined between two substrates. The process was conducted in an atmosphere of palladium-purified molecular hydrogen (H_2). In order to determine the optimum regime, we have studied the dependence of the thickness and structure of $(Si_2)_{1-x}(ZnS)_x$ epilayers on the growth conditions (crystallization onset temperature, cooling rate, and spacing between parallel substrates). Growth at a cooling rate of 0.7–1.0 K/min and an optimum gap of 1−1.5 mm ensured the formation of mirror-smooth epilayers.

We have also used an X-ray microprobe of the Jeol JSM 5910LV type (Japan) for scanning of the surface (Fig. 1) and cleavages (Fig. 2) of $(Si_2)_{0.08}(ZnS)_{0.92}$ epilayers. Scanning images of the sample surface showed that the epitaxial films contain no macroscopic defects or metal inclusions. The component elements are homogeneously distributed both in plane and in depth of the epilayer.

Figure 3 shows the results of measurements of the current–voltage (I–U) characteristic and the spectral sensitivity of obtained epilayers in p-Si–$(Si_2)_{1-x}(ZnS)_x$ heterostructures. As can be seen from Fig. 3a, the slope of the I–U curve after breakdown of the p–n junction is determined by a large contact resistance. The spectral characteristic in Fig. 3b shows that a short-wavelength photosensitivity boundary occurs at 0.45 μm instead of

the expected value of 0.4 μm, which can be explained by a relatively large film thickness. The long-wavelength boundary is observed at 1.1 μm, which is evidence of Si-rich composition of $(Si_2)_{1-x}(ZnS)_x$ solid solution formed at the heterojunction.

Thus, we have grown $(Si_2)_{1-x}(ZnS)_x$ ($0.08 \leq x \leq 0.92$) solid solutions by liquid phase epitaxy from a limited volume of tin-based solution melt. The photosensitivity range of the obtained solid solutions corresponds to the interval of photon energies from 1.05 to 3.0 eV, which makes the obtained structures a promising material for photo- and optoelectronic devices.

REFERENCES

1. S. V. Svechnikov, L. V. Zav'yalova, N. N. Roshchina, *et al.*, Fiz. Tekh. Poluprovodn. (St. Petersburg) **34**, 1178 (2000) [Semiconductors **34**, 1128 (2000)].

2. V. S. Khomchenko, L. V. Zav'yalova, N. N. Roshchina, *et al.*, Zh. Tekh. Fiz. **72** (8), 44 (2002) [Tech. Phys. **47**, 978 (2002)].

3. B. Sapaev, A. S. Saidov, and U. T. Davlatov, Vestn. Gulistansk. Gos. Univ., No. 1, 50 (2001).

4. V. M. Andreev, L. M. Dolginov, and D. N. Tret'yakov, *Liquid-Phase Epitaxy in Technology of Semiconductor Devices* (Sov. Radio, Moscow, 1975) [in Russian].

5. M. Hansen and K. Anderko, *Constitution of Binary Alloys* (McGraw-Hill, New York, 1965; Metallurgiya, Moscow, 1970), Vol. 2.

Translated by P. Pozdeev

Ionization Parameters of Some Nitro Compounds on the Surface of Alkali Metal Oxide Bronze

V. I. Kapustin*, V. S. Petrov, and A. A. Chernousov

Moscow Institute of Radio Engineering, Electronics, and Automation (Technical University), Moscow, 117454 Russia
** e-mail: kapustin@mirea.ru*
Received March 17, 2004

Abstract—The efficiency and activation energy of the selective ionization of some nitro compounds (TNT, HMX, RDX, etc.) on the surface of sodium–vanadium oxide bronze under atmospheric conditions have been evaluated for the first time. © 2004 MAIK "Nauka/Interperiodica".

The phenomenon of selective ionization of amine molecules on the heated surface of oxidized refractory metals under atmospheric conditions has been known since the 1970s, but an adequate physical interpretation of the experimental results was given only recently by Bannykh *et al.* [1]. The same paper pointed out for the first time that a new phenomenon—selective ionization of amine molecules on the heated surface of sodium–vanadium oxide bronze under atmospheric conditions—takes place as well.

Investigations of the surface ionization of the molecules of organic nitro compounds at relatively low temperatures under atmospheric conditions must take into account peculiarities both in the electron structure of nitro groups of these compounds and in the surface structure of alkali metal oxide bronzes. Indeed, this surface under certain condition may contain weakly bound alkali metal ions (AMIs) characterized by increased mobility of diffusion over interstitial sites of the crystal lattice of oxide bronzes. The surface of such bronzes, containing active centers of the AMI type, may initiate surface reactions involving the capture of AMIs by nitro groups of a nitro compound. This is related to the fact that nitrogen atoms in organic molecules of this class form so-called semipolar bonds with two oxygen atoms. This bond possesses a large dipole moment capable of capturing AMIs (without electron exchange) via the reaction

$$\{AMI\} + M \Leftrightarrow (M + Na)^+$$
$$\Leftrightarrow (M - R - H + Na)^+ + (R + H)_{gas}. \qquad (1)$$
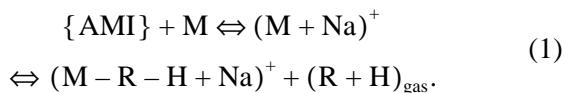
Since the Saha–Langmuir equation is inapplicable to reaction (1), the rate I_i of the surface ionization of nitro compounds (the ion current) can be calculated using the method of absolute reaction rates as

$$I_i(T) = A \frac{P^n}{T^{5/2}} \exp\left(-\frac{\Delta E}{kT}\right), \qquad (2)$$

where A is a constant, P is the partial pressure of organic molecules at the oxide surface, ΔE is the ionization activation energy, and n is the reaction order determined by the multiplicity of bonds between adsorbed molecules and the oxide surface.

We have studied the surface ionization parameters of a series of nitro compounds using a drift spectrometer described in [2]. The samples of solutions of these organic compounds were applied onto the surface of a bronze spiral heated by dc electric current. The regime
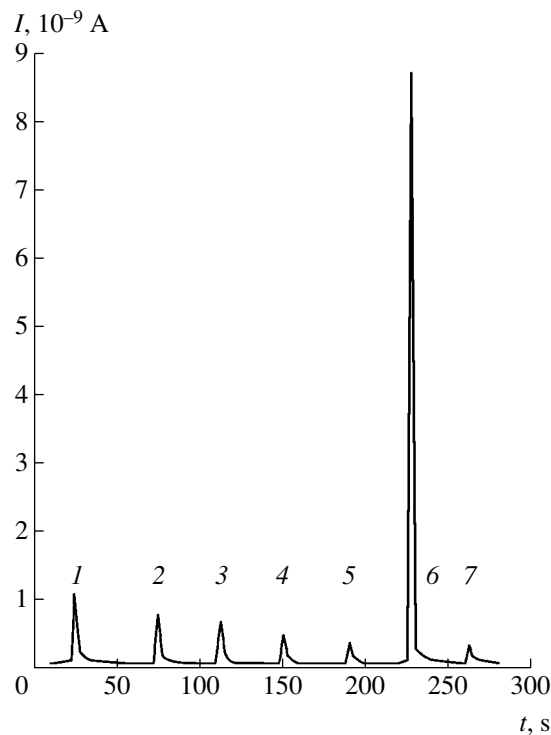
Ion current peaks observed during the ionization of some nitro compounds on the surface of sodium–vanadium oxide bronze: (*1*) trinitrotoluene (TNT); (*2*) octogen (HMX); (*3*) hexogen (RDX); (*4*) tetryl; (*5*) tetraethyl nitrile; (*6*) ammonium nitrate; (*7*) picric acid.

Surface ionization parameters of some nitro compounds on the heated surface of sodium–vanadium oxide bronze

Compound	TNT	HMX	RDX	Tetryl	Tetraethyl nitrile	Ammonium nitrate	Picric acid
Ionization efficiency, C/mol	0.24	0.22	0.10	0.060	0.020	0.64	0.020
Ionization activation energy, eV	0.90	1.35	0.40	–	–	1.05	–

of heating was selected so that the sample evaporation time was about 5–10 s. The ionization efficiency was determined using the area under the ion current peak (proportional to the charge transferred to the ion current collector), the mass of the sample, and the molecular weights of organic compounds.

The typical ion current peaks observed for the ionization of trinitrotoluene (TNT), octogen (HMX), hexogen (RDX), tetryl, tetraethyl nitrile, ammonium nitrate, and picric acid are presented in the figure. The values of the ionization efficiencies for these organic compounds at an emitter temperature of 420°C are listed in the table. The table also presents the activation energies calculated using the results of ionization efficiency measurements at various temperatures of the ion emitter.

As can be seen from the experimental data, the efficiency of selective ionization of the series of nitro compounds studied on the surface of sodium–vanadium oxide bronze is relatively high, while the activation energies for the surface ionization of nitro compounds are comparable with the values reported for the surface of oxidized refractory metals [1].

REFERENCES

1. O. A. Bannykh, K. B. Povarova, V. I. Kapustin, *et al.*, Dokl. Akad. Nauk **385**, 200 (2002).
2. O. A. Bannykh, K. B. Povarova, V. I. Kapustin, *et al.*, Naukoemkie Tekhnol. **3** (4), 37 (2002).

Translated by P. Pozdeev

Generation of Subnanosecond 10-GHz Pulses in High Peak and High Average Power Mode

S. D. Korovin, S. K. Lyubutin, G. A. Mesyats, V. V. Rostov*, S. N. Rukin,
B. G. Slovikovsky, M. R. Ul'maskulov, K. A. Sharypov, V. G. Shpak,
S. A. Shunailov, and M. I. Yalandin**

Institute of High-Current Electronics, Siberian Division, Russian Academy of Sciences, Tomsk, Russia;
Institute of Electrophysics, Ural Division, Russian Academy of Sciences, Yekaterinburg, Russia
e-mail: * rostov@lfe.hcei.tsc.ru; ** yalandin@iep.uran.ru
Received March 18, 2004

Abstract—The regime of excitation of microwave pulses in a 10-GHz range at a pulse duration of 0.8 ns and a peak power of ~2 GW has been studied in a relativistic backward wave oscillator with an extended periodic slow-wave system. A pulsed electron accelerator generating high-current electron beams (3 GW, ~600 keV, ~5 kA, 7 ns) at a repetition rate of 700 Hz and a pulse train width of 1 s has been developed based on a high-voltage generator with inductive energy storage, a semiconductor current interrupter, and a pulse-sharpening hydrogen-filled discharge gap. Optimization of the regime of the field-particle interaction allowed an average microwave power of 2.5 kW to be obtained at a transport magnetic field strength reduced below the cyclotron resonance value. © *2004 MAIK "Nauka/Interperiodica".*

Previous experimental investigations of the regimes of nonstationary generation of high-power electromagnetic radiation in relativistic microwave generators of the backward wave oscillator (BWO) type [1–6] confirmed theoretical predictions [7–9] that short (on the scale of the interaction space length) radiation pulses can be obtained provided that the electron beam current significantly exceeds the start value. Under certain conditions, the peak power level of such pulses is not limited by the driving electron beam power. The full width at half maximum (FWHM) of the envelope of these pulses usually does not exceed ten periods of the microwave signal, which significantly increases the electric strength of the slow wave system (SWS) and allows the use of small-size high-current electron accelerators with a current pulse duration of several nanoseconds.

Preliminarily, we have studied the regimes of generation of rarely repeated subnanosecond gigawatt microwave pulses in the 10-GHz range [4, 6]. In these experiments, the factors of the electron beam power conversion into microwave $K \approx 1.4$–1.8 at a peak power of up to 3 GW were obtained using transport magnetic field strengths as high as $B_Z \approx 2.5$–3 T, that is, above the conditions of cyclotron resonance with the backward wave. An analogous regime was recently realized [5] using a small-size oscillator operating in the millimeter wavelength range ($B_Z = 6.5$ T; $K = 1.5$). Previously [3], generation at a repetition frequency of up to 3500 Hz and a power conversion factor of about 0.5 was achieved for subnanosecond 38-GHz microwave pulses at $B_Z = 2$ T (i.e., below the cyclotron resonance value) using a spe-

cially designed hybrid modulator ensuring the formation of stable accelerating pulses [10].

The present study was aimed at assessing the possibility of increasing the conversion factor in relatively low magnetic fields and obtaining subnanosecond gigawatt pulses in the 10-GHz range at a high repetition rate.

According to the results of the aforementioned investigations, the main factor limiting the power conversion in low magnetic fields is related to the development of strong transverse oscillations of electrons in the backward wave field. This negative effect is enhanced on the background of nonoptimized structural characteristics of the electron beam formed by an explosive-emission injector in a weak magnetic field. For the 10-GHz range and particle energies on the order of 500 keV, there only exists a rather narrow interval of magnetic fields below the cyclotron resonance value ($B_Z \sim 0.5$–0.6 T) in which a tubular electron beam can be obtained with transverse oscillations within acceptable limits. Further decrease of the magnetic field deteriorates the electron beam structure, while an increase also gives no advantages, since the transverse oscillations of electrons in the backward wave may grow up to a level leading to their significant losses on the SWS walls.

However, the problem's solution can be facilitated by providing decompression of the electron beam, which can be achieved by placing the explosive emission cathode into a stronger field and by expanding the beam at the SWS entrance, where the focusing field is maintained on a low level [11]. Another idea developed in this study consists in optimizing the rate of energy
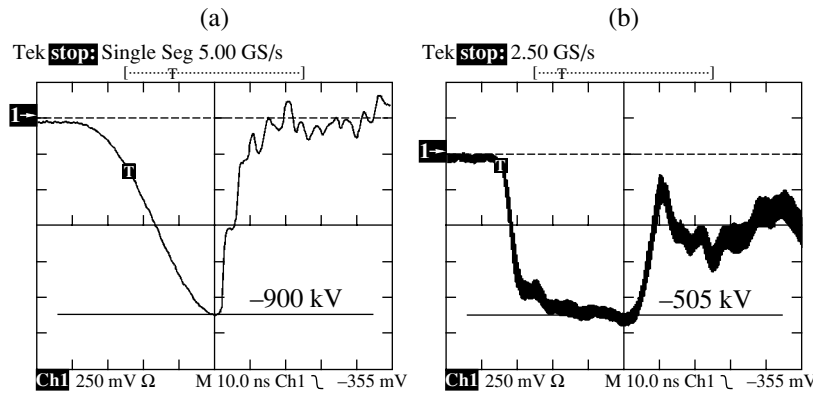
Fig. 1. Typical oscillograms of (a) a charging voltage in the 50-Ω pulse forming line of the hybrid modulator and (b) a voltage pulse in the 75-Ω transmitting line (measured in the envelope signal accumulation regime at a repetition rate of 700 Hz and registered by a Tektronix TDS684B oscillograph).

uptake from the electron beam along the entire SWS length so as to ensure localization of the maximum high-frequency field amplitude of the oncoming pulse at the beginning of the SWS. It was demonstrated [9] that this condition corresponds to a linear growth of the electromagnetic pulse power as it propagates from the collector to cathode end of the SWS. If the electron current ceases by the moment of the pulse arrival to the microwave reflector, we may hope both to provide the optimum energy uptake from the "working" part of the beam and to minimize the losses of pulse energy for pumping transverse electron oscillations in the course of nonsynchronized (wake field) interaction. Besides the appropriate longitudinal distribution of coupling between electrons and the synchronous mode, it is also important to select the optimum electron beam pulse duration and the pulse front width.

The accelerating voltage pulses at a high repetition rate were formed using a hybrid high-voltage modulator analogous to that used in [3], based on a charging device (driver) with solid-state commutators and an output stage comprising an inductive energy storage and a current interrupter based on SOS diodes [12]. Stable voltage pulses formed by a driver of the S-5N type [13] with a pulse front width of about 40 ns were used to charge a coaxial pulse forming line (50 Ω, 75 pF) to a voltage of 850–900 kV (Fig. 1a). After switching of a two-electrode pulse-sharpening discharger (filled with hydrogen at 50 bar), a voltage pulse with FWHM ~ 7 ns and a front width of ≤1 ns (Fig. 1b) was fed to a coaxial transmitting line (TL) having a wave impedance of 75 Ω. The accelerating voltage pulse, supplied from TL to a vacuum electron accelerator diode with a characteristic impedance of 120 Ω, had an amplitude of 500–520 kV and a peak power of ~3.5 GW. It should be noted that neither gas circulation in the discharge gap nor hydrogen cooling systems were used. Nevertheless, no decrease in the accelerating pulse voltage was observed for the pulse forming line commutated at an energy of 25–30 J, a repetition rate of up to 730 Hz, and

a pulse train width of 1 s, while the total scatter of pulse amplitude did not exceed 5–7%.

The oscillator was numerically modeled using the particle-in-cell method (PIC code KARAT) [14]. The numerical tests were performed for an SWS accommodating 30 corrugation periods with a median diameter of $2R \approx 1.4\lambda$, a lumped band-stop reflector, and an electron injector in which the accelerating voltage pulse shape was close to real profiles. The system optimization was achieved through variation of the following characteristics: transport magnetic field profile with electron beam decompression; magnetic induction; vacuum diode impedance; coupling resistance profile along the SWS (for the electron beam coupling to synchronous harmonic of the backward wave TM_{01}); and the reflector geometry and position.

The final results of numerical modeling presented in Fig. 2 indicate that it is possible to obtain a peak output power of 2.5 GW (Fig. 2d) at a beam power conversion factor of $K \approx 0.7$ and a magnetic induction of $B_Z \approx 0.55$ T in the SWS. According to the system configuration depicted in Fig. 2b, the cathode is arranged in the region where $B_Z = 0.75$ T. As is known, enhanced magnetic field favors the more homogeneous distribution of the explosive emission centers at the cathode edge [15]. On the passage through a ~10-cm-long decompression region at the SWS input, the beam diameter expands from 30 to 34 mm and, passing along the SWS, gradually increases to 36 mm. This decreases the probability of electron escape to the SWS wall in the region of the resonance reflector, where the fields of the generated wave are most intense. It should be noted that numerical modeling of the system operation with a strong magnetic field (~3 T) gave a conversion factor of $K \geq 1$. Apparently, a power conversion threshold of $K \sim 1$ in weak magnetic fields limited by transverse electron oscillations in the backwards wave field can be achieved by further increasing the transverse dimensions of the SWS.
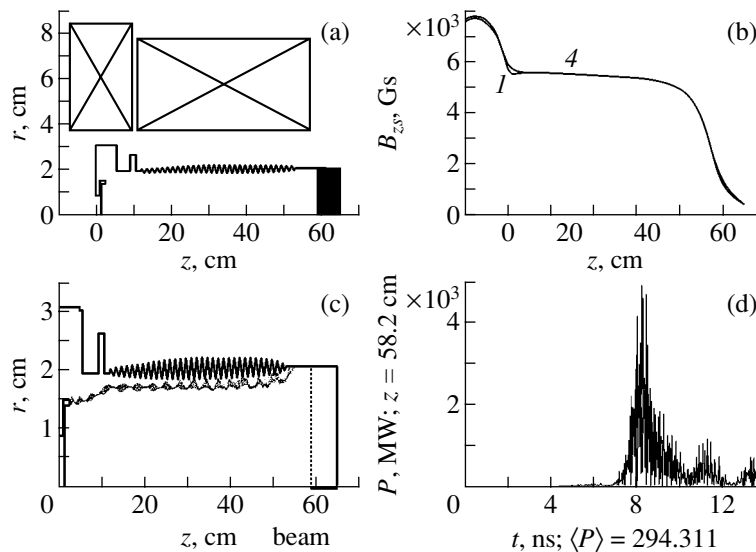
Fig. 2. The results of numerical modeling of a subnanosecond relativistic BWO: (a) electron injector, focusing solenoid, and SWS geometry; (b) magnetic field profile along the SWS axis; (c) tubular electron beam trajectory; (d) nonaveraged power flux of microwave pulses.

The aforementioned electron injector, solenoid, and SWS geometry was reproduced in an experimental setup based on the hybrid modulator described above. The magnetically insulated vacuum diode of the electron accelerator was equipped with a tubular graphite explosive-emission cathode with a diameter of 30 mm and an emitter edge thickness of 300 μm. The experiments were performed with an oil-cooled two-section dc solenoid. The windings were supplied with a stabilized current of 120 A from a small-size storage battery of molecular capacitors with an IGBT switch. The charging device power and the capacitor bank energy were sufficient to produce two to three 1-s pulse trains per minute.

In the course of experiments, the energy of the output microwave pulses was measured using a liquid calorimeter with a capillary meter characterized by a linear shift of the liquid level depending on the energy up to 170 J and by a responsivity of 2.9 J/mm. The results of measurements performed over several sequential cycles of the microwave oscillator showed that the output energy per pulse was 3.5 J with a scatter of no more than 3%. Thus, for 1-s trains at a repetition rate of 730 Hz, we obtained an average output microwave power of 2.5 kW.

In order to determine the peak output power, the calorimetric measurements were supplemented by monitoring of the microwave pulse envelope using a noncooled hot-carrier germanium detector linked to a broadband oscillograph. The hot-carrier detector design was analogous to that used previously [4, 6]. The results of calibration measurements showed that no significant heating of the crystal (having a resistance of 120 Ω) and no drift of the current–voltage characteristic took place for the bias voltage pulses (40 V, 3×10^{-5} s)

at a repetition rate of up to 1 kHz. The high-voltage cable (RG402) and other components of the circuit connecting the hot-carrier detector to the oscillograph were calibrated using rectangular test pulses with a 90-ps front width. The calibration procedure was performed using a 6-GHz Tektronix digital stroboscopic oscillograph forming one oscillogram by accumulating 512 sequential readings.

The output microwave signals were experimentally measured on a periphery of the radial distribution of the TM_{01} wave power at a distance of 5 m from the antenna. This distribution was monitored using a videocamera
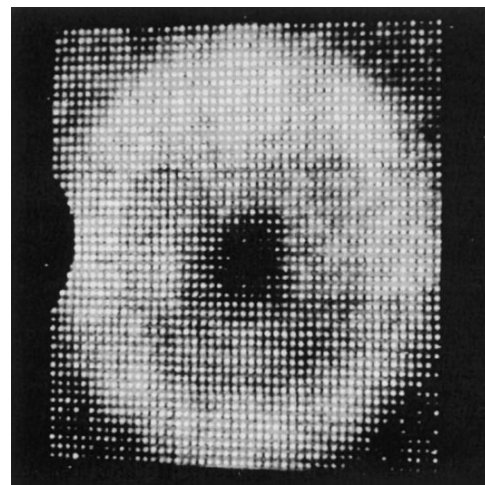

Fig. 3. The typical pattern formed by subnanosecond 10-GHz microwave (TM_{01} mode) pulses at a repetition rate of 50 Hz on a 150×150-cm panel of neon gas-discharge lamps monitored by a videocamera.
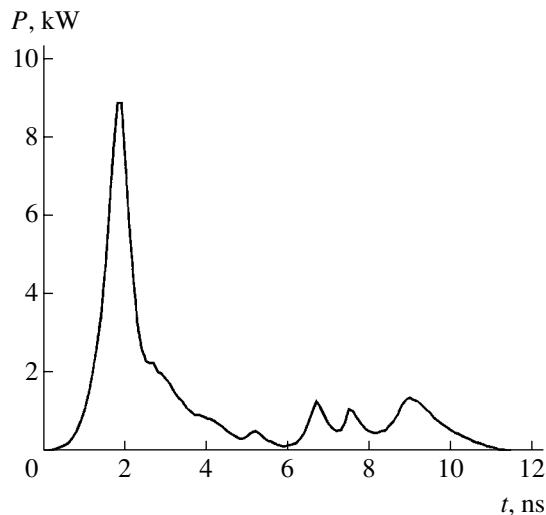
P, kW

Fig. 4. The shape of a BWO output microwave pulse in the time versus power coordinates reconstructed from the data obtained using a hot-carrier germanium detector and the volt–watt calibration dependence measured at a frequency of 10 GHz.

and a panel with neon gas-discharge lamps (Fig. 3). Positioning of the detector at the edge of the directional pattern ensured detection in the dynamical range of calibration and minimized the probability of signal distortions caused by nonlinearity of the detector and the off-band radiation component (wide-band emission from the beam front and harmonics of the fundamental frequency [16, 17]). However, more significant difficulties were related to nonideal cutoff of the microwave carrier frequency in the coaxial part of the detector and to a broad spectrum of the microwave signal envelope (video pulse). Even small admixture of the carrier frequency produced a significant effect of "deterioration" of the amplitude stability as a result of the random phase variation from pulse to pulse. The problem of this frequency filtration was solved by averaging over ten oscillograms. As a result, each microwave pulse envelope in the time versus power coordinates (Fig. 4) was obtained using more than 5000 pulses. The results of processing of such averaged oscillograms, depicted in Fig. 4, show that the pulse has FWHM ~ 800 ps and a peak power of 2.2 GW (with allowance for a total microwave pulse energy of 3.5 J). Alternative calculations of the peak power using a hot-carrier detector calibrated for 9.8 and 10.1 GHz gave results deviating from this value by no more than ±1.5%. Thus, with allowance for the typical absolute error of calibration measurements (~20%), the measured peak power agrees well with the results of numerical experiments and the beam power conversion factor has proved to be no less than 0.6.

The obtained results are consistent with the commonly accepted notions that the electric strength of insulation increases when the pulse width decreases (see, e.g., [18]). At a maximum microwave electric field strength of ~100 kV/cm at the aperture of the radiating horn and a repetition rate of 50 Hz, there was no evidence of breakdown in air or on the vacuum window surface. At a maximum repetition rate of 730 Hz, an insignificant ozone formation could be perceived, but still no visible evidence of breakdown. It should be noted that high electric strength is characteristic of the microwave oscillator under consideration not only from the standpoint of microwave radiation extraction into atmosphere, but in a more general aspect as well. Indeed, the results of our experiments showed that the system studied was not critically sensitive with respect to a number of phenomena (such as secondary emission resonance discharges, explosive-emission processes, plasma formation in the SWS, etc.) frequently posing limitations on the radiation pulse duration in high-power microwave electronics. For example, estimates based on the assessment of the degree of SWS heating showed that there was a considerable leak current of "used" electrons to the SWS wall, and the corrugated SWS surface played the role of a distributed beam current collector. In a long-pulse relativistic BWO, this phenomenon makes possible a quasiperiodic or complete breakage of the generation regime [19, 20]. In our experiments, no such effects caused by plasma-emissive processes were observed.

Thus, we have developed and realized a pulsed periodic regime of generation of high-power electromagnetic pulses with a carrier microwave frequency of 10 GHz based on the induced Cherenkov radiation in a spatially confined wave–beam system with a high signal gain per wave passage. Operating at a repetition frequency of 700 Hz and a 1-s pulse train width, the proposed BWO provides for a peak power above 2 GW and an average power of 2.5 kW. The laboratory BWO prototype can be of interest for both basic research and radio engineering applications.

REFERENCES

1. M. I. Yalandin, V. G. Shpak, S. A. Shunailov, *et al.*, IEEE Trans. Plasma Sci. **28**, 1615 (2000).

2. S. D. Korovin, G. A. Mesyats, V. V. Rostov, *et al.*, Pis'ma Zh. Tekh. Fiz. **28** (2), 81 (2002) [Tech. Phys. Lett. **28**, 76 (2002)].

3. D. M. Grishin, V. P. Gubanov, S. D. Korovin, *et al.*, Pis'ma Zh. Tekh. Fiz. **28** (19), 24 (2002) [Tech. Phys. Lett. **28**, 806 (2002)].

4. A. A. Elchaninov, S. D. Korovin, I. V. Pegel, *et al.*, in *Proceedings of the 14th International Conference on High-Power Particle Beams (BEAMS-2002), Albuquerque, 2002*, pp. 279–282.

5. S. D. Korovin, G. A. Mesyats, V. V. Rostov, *et al.*, Pis'ma Zh. Tekh. Fiz. **30** (3), 68 (2004) [Tech. Phys. Lett. **30**, 117 (2004)].

6. A. A. Elchaninov, S. D. Korovin, V. V. Rostov, *et al.*, Pis'ma Zh. Éksp. Teor. Fiz. **77** (6), 314 (2003) [JETP Lett. **77**, 266 (2003)].

7. N. S. Ginzburg, Yu. V. Novozhilova, and A. S. Sergeev, Pis'ma Zh. Tekh. Fiz. **22** (9), 39 (1996) [Tech. Phys. Lett. **22**, 359 (1996)].

8. A. A. Eltchaninov, S. D. Korovin, V. V. Rostov, *et al.*, Laser Part. Beams **21**, 187 (2003).

9. A. A. Elchaninov, S. D. Korovin, I. V. Pegel', *et al.*, Izv. Vyssh. Uchebn. Zaved. Radiofiz. **46**, 874 (2003).

10. S. K. Lyubutin, G. A. Mesyats, S. N. Rukin, *et al.*, Prib. Tekh. Éksp., No. 5, 80 (2001).

11. I. K. Kurkan, V. V. Rostov, and E. M. Tot'meninov, Pis'ma Zh. Tekh. Fiz. **24** (10), 43 (1998) [Tech. Phys. Lett. **24**, 388 (1998)].

12. S. N. Rukin, Prib. Tekh. Éksp., No. 4, 5 (1999).

13. A. I. Bushlyakov, A. V. Ponomarev, S. N. Rukin, *et al.*, Prib. Tekh. Éksp., No. 2, 74 (2002).

14. V. P. Tarakanov, *User's Manual for Code "Karat"* (Berkley, Springfield, 1992).

15. S. Ya. Belomyttsev, S. D. Korovin, and G. A. Mesyats, Pis'ma Zh. Tekh. Fiz. **6**, 1089 (1980) [Sov. Tech. Phys. Lett. **6**, 466 (1980)].

16. N. S. Ginzburg, A. S. Sergeev, I. V. Zotova, *et al.*, Nucl. Instrum. Methods Phys. Res. A **393**, 352 (1997).

17. V. P. Gubanov, S. D. Korovin, V. V. Rostov, and A. V. Smorgonsky, Pis'ma Zh. Tekh. Fiz. **11** (2), 93 (1985) [Sov. Tech. Phys. Lett. **11**, 37 (1985)].

18. N. S. Ginzburg, N. Yu. Novozhilova, I. V. Zotova, *et al.*, Phys. Rev. E **60**, 3297 (1999).

19. M. I. Yalandin, V. G. Shpak, and V. P. Tarakanov, in *Proceedings of the Pulsed Power Plasma Science Conference, Las Vegas, 2001*, pp. 544–547.

20. A. S. Elchaninov, F. Ya. Zagulov, S. D. Korovin, *et al.*, Pis'ma Zh. Tekh. Fiz. **7**, 1168 (1981) [Sov. Tech. Phys. Lett. **7**, 499 (1981)].

Translated by P. Pozdeev

Ionization Kinetics
in a Supersonic Xenon Plasma Flow Entering Electric Field

T. A. Lapushkina*, R. V. Vasil'eva, A. V. Erofeev,
S. A. Ponyaev, and S. V. Bobashev

Ioffe Physicotechnical Institute, Russian Academy of Sciences, St. Petersburg, 194021 Russia
* e-mail: tanyusha@mail.ioffe.ru
Received March 19, 2004

Abstract—We have studied xenon plasma moving in a supersonic diffuser in external electric and magnetic fields. The main physical parameters of the plasma (electron temperature and density) were determined using specially developed methods based on the theory of continuous optical emission from inert gas atoms. These experimental data are compared to the results of theoretical calculations. Based on an analysis of the results of spectroscopic measurements, a mechanism of plasma ionization is established which is capable of maintaining a high degree of ionization in the supersonic xenon plasma flow. © *2004 MAIK "Nauka/Interperiodica".*

Introduction. This study was inspired by attempts to use magnetohydrodynamic (MHD) methods for controlling shock waves arising in a supersonic diffuser [1, 2]. When air is used as a working gas, it has to be preliminarily ionized by means of external sources to an extent making conductivity of the medium sufficiently high to provide for a significant MHD interaction. In contrast to air, inert gases (in particular, xenon) are characterized by relatively low recombination coefficients. For this reason, the ionized state created in the region of MHD interaction is retained for a time sufficiently long to change the shock wave configuration in this region.

This study was aimed at the development of spectral methods for determining the electron temperature and density in plasma flows, comparison of the results of measurements with theoretically calculated values [3], and analysis of the ionization mechanisms.

The experiments were performed in a diffuser, where a supersonic flow was exposed to the action of external electric and magnetic fields. During passage of an electric current, the supersonic flow is retarded as a result of the action of ponderomotive forces and Joule heating, which changes the positions of attached shock waves. Selective heating of electrons leads to an additional ionization of the working gas, thus increasing the conductivity of plasma and the MHD interaction parameter.

Experimental setup. The experimental setup (Fig. 1) and methods were described in detail elsewhere [2]. The setup consists of a shock tube (*1*) with a diameter of 50 mm, separated by a thin Dacron diaphragm from a vacuum chamber comprising a flat supersonic nozzle (*2*) and a diffuser (*3*). When a shock-compressed gas is stopped at the tube end, the gas temperature increases and a preliminary thermal ionization takes place. The

calculated stagnant gas parameters are as follows: heavy-component temperature equal to the electron temperature, $T_h = T_e = 9600$ K; heavy-particle concentration, $n_h = 1.25 \times 10^{25}$ m^{-3}; degree of ionization, $\alpha = 0.05$; conductivity, $\sigma = 3700$ S/m. The ionized gas passes through a narrow inlet slit at the shock tube end and enters the expanding 84-mm-long supersonic nozzle with an expansion factor of 5.7. The calculated flow parameters at the nozzle outlet are as follows: Mach number, M = 4.3; flow velocity, $u = 1550$ m/s; $T_h = 1600$ K; $T_e = 3950$ K; $n_h = 6.6 \times 10^{23}$ m^{-3}; $\alpha = 0.0016$; $\sigma = 640$ S/m; efflux time, $\tau \sim 500$ μs.

Leaving the nozzle, the ionized gas moves in a transverse magnetic field *B* and enters the supersonic diffuser, forming attached shock waves (*8*). The diffuser is equipped with brass electrodes (*5*), to which an external voltage is applied. Thus, the resulting current measured
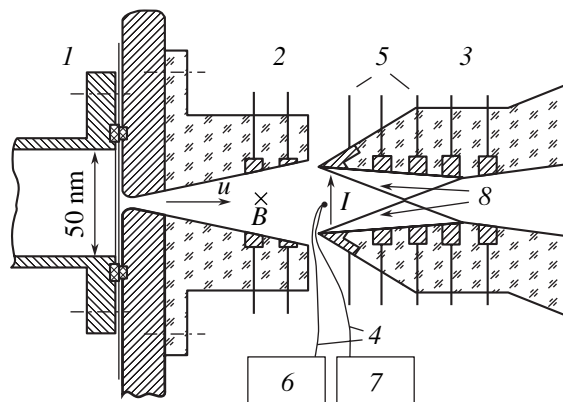

Fig. 1. Schematic diagram of the experimental setup (see the text for explanations).

upon closing the circuit includes components induced by both magnetic and electric fields.

The electron temperature and density in the plasma were measured based on the Unzold–Kramers theory of continuous optical emission and the Bierman–Norman theory [4]. According to this, the electron temperature in the plasma of inert gases can be determined by measuring the edge of continuum in the near UV region, while the electron density can be evaluated by measuring the absolute intensity of the continuous spectrum. The reference was the emission from a slug of the shock-compressed gas in the shock tube, whose parameters are well known [5].

The intensity of emission in various spectral regions was measured using two schemes. In the first variant, employing a photomultiplier (6), the desired spectral region was separated using interference filters or a grating monochromator [6]. In the second variant, the measurements were performed with an Ocean Optics spectrograph (7), which was also used for the spectral analysis of plasma emission and for determining the signal/background ratio of various spectral lines.

Results and discussion. Figure 2 shows plots of (a) the electron temperature T_e and density n_e and (b) the ratio of separate line intensities J_λ to the intensity of continuum J_c versus the plasma current I. These data were obtained in the absence of magnetic field, when the current was varied by changing the voltage applied to the electrodes.

Figure 2a shows experimental data in comparison to the results of theoretical calculations [3] performed within the framework of the theory of ionization kinetics for inert gases [7]. This theory involves the concept of a "bottleneck," whose position in the space of energy levels determines the ionization rate. As can be seen, the experiment and theory reveal the same trends in T_e and n_e in response to current variations. Depending on the current, it is possible to separate two regimes: recombination and ionization. For $I = 0$, the recombination regime dominates. A comparison of the measured electron density n_e to the values calculated using the Saha formula for a reduced electron temperature T_e shows that $n_e \gg n_{e(eq)}$, where $n_{e(eq)}$ is the equilibrium value. As can be seen from Fig. 2a, an increase in the current leads to selective heating of electrons accompanied by the development of nonequilibrium ionization, whereby estimates show that $n_e \ll n_{e(eq)}$.

Figure 2b shows the relative intensities of spectral lines corresponding to the transitions from the groups of excited levels with various positions relative to the ground state. In particular, the blue lines with $\lambda = 462.4$ and 467.1 nm belong to the group of levels with an average energy of 11 eV (denoted as $N3$). The red lines with $\lambda = 823.2$ and 828.0 nm belong to the group of levels with an average energy of 9.8 eV (denoted as $N2$). The bottom levels with an average energy of 8.4 eV constitute group $N1$.
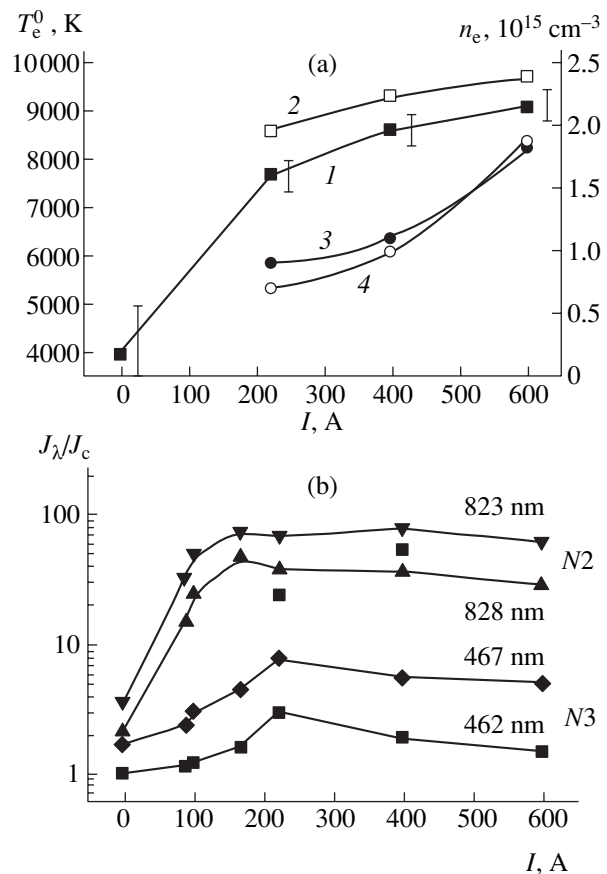

Fig. 2. Plots of (a) the electron temperature T_e (1, 2) and the electron density n_e (3, 4) [(1, 3) experiment; (2, 4) theory] and (b) the ratio of separate line intensities J_λ to the intensity of continuum J_c versus the plasma current I.

An analysis of the data in Fig. 2 shows that the state of plasma under our experimental conditions is nonequilibrium. This state can be characterized using several parameters. The first is the ionization temperature T_i, which formally (by the Saha formula) corresponds to the electron density. It is this value that mostly determines the intensity of continuous emission, representing recombination continuum in the visible range: $J_c \sim n_e^2 T_e^{-1/2}$. The second is the population temperature T_p, formally (by the Boltzmann formula) determining the population of levels and, hence, the intensity of lines J_λ. In particular, the population temperatures of the blue and red lines are denoted as T_{pb} and T_{pr}. Finally, T_e characterizes the thermal energy of free electrons. The character of dependences presented in Fig. 2 shows that, in the recombination regime (when the spectral lines are virtually indistinguishable on the continuous background), $T_i > T_{pb} > T_{pr} > T_e$. In the ionization regime at an electron temperature below 8000 K, the intensities of lines grow on the background of continuum, which is evidence that $T_i < T_{pb} < T_{pr} < T_e$. As the electron tem-

perature grows further, the populations of levels in the blue and red groups tend to equilibrium with the ionization process: $T_i = T_{pb} = T_{pr}$. Our experimental data suggest that the ionization rate under the conditions studied (Fig. 2) at $T_e < 8000$ K is determined primarily by the rate of population of levels in the $N2$ group, while at higher temperatures, the bottleneck shifts to the $N1$ group.

Conclusions. The results of our experiments showed that heating of the inert gas plasma under non-equilibrium conditions is accompanied by the shift of the bottleneck (determining the ionization rate) toward lower energy levels. This maintains the process of ionization in the expanding flow and provides the degree of ionization at the diffuser input on a level sufficient for MHD experiments.

REFERENCES

1. E. P. Gurijanov and P. T. Harsha, AIAA Pap. No. 96-4609 (1996).
2. T. A. Lapushkina, S. V. Bobashev, R. V. Vasil'eva, *et al.*, Zh. Tekh. Fiz. **72** (4), 23 (2002) [Tech. Phys. **47**, 397 (2002)].
3. Yu. P. Golovachev, Yu. Kurakin, A. A. Schmidt, and D. Van Wie, AIAA Pap. No. 2001-2883 (2001).
4. L. M. Biberman and G. E. Norman, Usp. Fiz. Nauk **91**, 193 (1967) [Sov. Phys. Usp. **10**, 52 (1967)].
5. G. K. Tumakaev and V. R. Lazovskaya, *Aerophysical Investigations of Supersonic Flows* (Nauka, Moscow, 1967) [in Russian].
6. T. A. Lapushkina, E. A. D'yakonova, and R. V. Vasil'eva, Pis'ma Zh. Tekh. Fiz. **24** (2), 58 (1998) [Tech. Phys. Lett. **24**, 66 (1998)].
7. L. M. Biberman, V. S. Vorob'ev, and I. T. Yakubov, *Kinetics of Nonequilibrium Low-Temperature Plasmas* (Nauka, Moscow, 1982; Consultants Bureau, New York, 1987).

Translated by P. Pozdeev

Gas Adsorption on Semiconducting Oxides: A Change in the Work Function

S. Yu. Davydov, V. A. Moshnikov, and A. A. Fedotov

Ioffe Physicotechnical Institute, Russian Academy of Sciences, St. Petersburg, 194021 Russia
St. Petersburg State Electrotechnical University, St. Petersburg, 197376 Russia
Received March 19, 2004

Abstract—Using a simple model, we have calculated the change in the work function of $ZnO(10\bar{1}0)$ and $TiO_2(110)$ surfaces as a result of adsorption of hydrogen atoms and oxygen molecules, the change in the charge of adsorbed species, and the adsorption-induced variation of the surface conductivity of semiconducting substrates. © 2004 MAIK "Nauka/Interperiodica".

Introduction. In contrast to the situation with $A^{IV}B^{IV}$ and $A^{III}B^V$ semiconductor compounds, the surface properties of metal oxides (such as wide-bandgap semiconductors ZnO, NiO, SnO_2, and TiO_2) have been less extensively studied, although these materials are also of considerable interest for various technological applications [1, 2]. The characterization of oxides encounters difficulties primarily because of the highly defective structure of these substances, which complicates the preparation of samples with reproducible composition and properties. The surfaces of samples having the same bulk composition but synthesized using slightly different methods may exhibit sharply different properties [1]. Another factor complicating the experimental investigation of oxides is the high adsorption activity of their surface. The theoretical situation is not much more advantageous: no commonly accepted approach to the description of semiconducting oxides has been developed so far, in particular, the mechanisms of adsorption on the oxide surface are still not clear.

This study is devoted to the adsorption of gaseous species (H and O_2) on the $ZnO(10\bar{1}0)$ and $TiO_2(110)$ surfaces, which were selected because variation of the work function $\Delta\phi$ depending on the time t of exposure to these gases has been measured [1, 3]. Once the $\Delta\phi(t)$ dependence (which can be transformed into $\Delta\phi(\Theta)$, where Θ is the surface coverage by adsorbed species) is known, it is possible to use a model approach to the description of the system studied. Note that the description of adsorption in this system is also of interest for applications, since zinc and titanium oxides are promising materials for gas sensors.

Theoretical model. The adsorption-induced change in the work function can be calculated using a simplified variant of the model developed previously for the adsorption of alkali metals on semiconductors [4] and applied, in particular, to $TiO_2(110)$ [5, 6]. The model takes into account both the interaction of adsorbed species with the substrate, leading to charge transfer from these particles to substrate and vice versa, and the dipole–dipole repulsion of particles in the adlayer.

Taking into account that hydrogen atom adsorbed on $ZnO(10\bar{1}0)$ and $TiO_2(110)$ surfaces behaves as a donor (hydrogen 1s-orbital electron passes to the substrate), the expression for the charge $Z = 1 - n$ (n is the 1s-orbital occupation number) of such an adatom can be written as

$$Z(\Theta) = \frac{1}{2} + \frac{1}{\pi}\arctan\frac{\Omega - \xi\Theta^{3/2}Z(\Theta)}{\Gamma}, \quad (1)$$

$$\xi = 2e^2\lambda^2 N_{ML}^{3/2}A,$$

where Ω is the energy of a quasi-level of the adatom relative to the Fermi level in the substrate; ξ is the constant of dipole–dipole repulsion between adatoms; 2λ is the surface dipole length; $A \sim 10$ is a dimensionless coefficient weakly dependent on the geometry of the surface lattice of adatoms; Γ is the half-width of the quasi-level of an isolated adatom; $\Theta = N/N_{ML}$; and N and N_{ML} are the concentrations of adatoms in the adlayer and in one monolayer, respectively.

In the case of adsorption of molecular oxygen, electrons are transferred from the substrate to the antibonding (loosening) π_{2p}^* orbital. The charge of the admole-

Model parameters for various gas/oxide systems

System	Φ, eV	ξ, eV	Γ, eV	N_{ML}, Å^{-2}	Ω/Γ
H/ZnO	5.33	1.03	0.005	0.059	–3.08
O_2/ZnO	16.00	10.64	0.025	0.044	6.31
O_2/TiO$_2$	2.00	1.33	0.0075	0.011	2.04

|Δφ|, meV

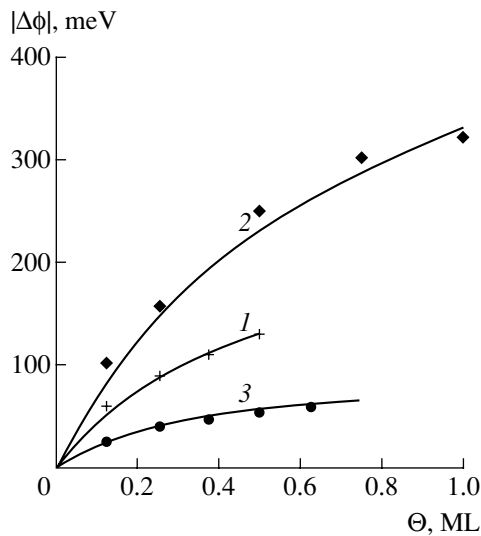**Fig. 1.** Plots of the work function |Δφ| versus adsorption coverage Θ expressed in monolayers (ML) for various gas/oxide systems: (*1*) H/ZnO(10$\bar{1}$0); (*2*) O$_2$/ZnO(10$\bar{1}$0); (*3*) O$_2$/TiO$_2$(110).
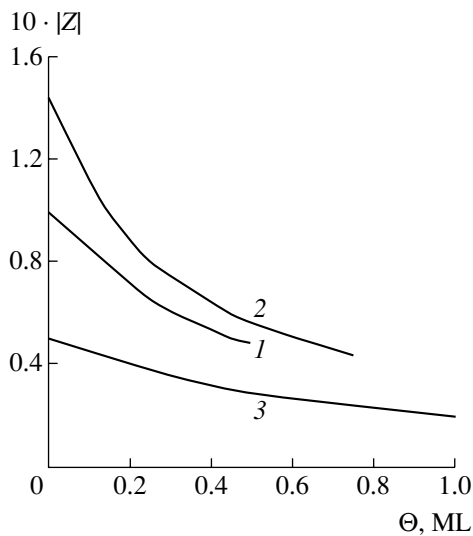
10 · |Z|

Fig. 2. Plots of the charge |Z| of an adsorbed particle versus adsorption coverage Θ for various gas/oxide systems (notation as in Fig. 1).

cule, $Z = -n$, where n is the number of transferred electrons, can be calculated using the formula

$$n(\Theta) = \frac{1}{2} - \frac{1}{\pi}\arctan\frac{\Omega + \xi\Theta^{3/2}n}{\Gamma}. \qquad (2)$$

The change in the work function Δφ(Θ) as a result of adsorption is

$$\Delta\phi(Q) = -\Phi\Theta Z,$$
$$\Phi = 4\pi e^2 N_{ML}\lambda. \qquad (3)$$

In contrast to a accurate descriptions [4–6], we consider a simplified model and ignore the smearing of quasi-levels of the adsorbed species into a band due to the direct and indirect exchange. In addition, we will not calculate the quasi-level energy Ω proceeding from the ionization potential of hydrogen and the electron affinity of oxygen molecule; the Ω value is considered as a parameter of the problem.

Adsorption of hydrogen atoms on ZnO(10$\bar{1}$0). According to the published data [1, 3], H$_2$ molecules are virtually not adsorbed at low pressures.[1] At elevated pressures, hydrogen molecules exhibit dissociation and atomic hydrogen is supplied to the surface of zinc oxide, where it behaves as a donor acquiring positive charge and reducing the work function (Δφ(Θ) < 0). For obtaining the Δφ(*t*) dependence presented in [1, 3], where *t* is the time of exposure in a hydrogen-containing atmosphere, it is necessary to find a relation between the exposure *t* and the surface coverage Θ. Taking into account the reported behavior of Δφ(*t*), which does not reach saturation at the maximum exposure of *t** = 1200 s, we assign this time to a coverage of Θ = 0.5. Assuming that one adatom corresponds to a surface unit cell with dimensions α$_0$ = 3.25 Å and c_0 = 5.207 Å, we can evaluate the monolayer density as N_{ML} = 0.059 Å^{-2}. Now, we can estimate the experimental value of $(d\Delta\phi/\Delta\Theta)_{\Theta\to 0} = -\Phi Z_0$, where $Z_0 \equiv Z(0)$ is the charge of an isolated adatom. Selecting "reasonable" values of Φ and Z_0 and assuming that λ = 1 Å, we determine all parameters of the problem (see table).[2]

Figure 1 (curve *1*) shows the results of such model calculations for |Δφ(Θ)| in comparison to the experimental data. As can be seen, the agreement is quite good. Variation of the charge of a hydrogen adatom is shown in Fig. 2 (curve *1*). In agreement with the general results of the theory [7–9], the charge of hydrogen adatom decreases with increasing surface concentration (coverage) due to the dipole–dipole depolarization.

Adsorption of oxygen molecules on ZnO(10$\bar{1}$0) and TiO$_2$(110). According to the modern notions of oxygen adsorption, O$_2$ molecule at room and elevated temperatures behaves as an acceptor, acquiring negative charge and increasing the work function (Δφ(Θ) > 0). The corresponding parameters, determined assuming that λ = 2 Å, are presented in the table. It should also be

---

[1] In all our papers, by adsorption we imply chemisorption, whereby specific chemical bonds are formed between adatoms (admolecules) and a substrate, rather than physical adsorption determined by the van der Waals interactions.

[2] Selection of the problem parameters is rather arbitrary and a criterion of the correct choice is the agreement of the calculated and experimental values of the adsorption-induced changes in the work function.

noted that, in the case of oxygen adsorption, we have to select a lower value for the monolayer density N_{ML}, which is probably indicative of a significant role of oxygen vacancies acting as adsorption centers [1–3]. Thus, in the case of oxides, the value of N_{ML} in the adopted model is interpreted as the number of adsorption centers on the substrate surface.

The results of calculations of $\Delta\phi(\Theta)$ for the system $O_2/ZnO(10\bar{1}0)$ are presented in Fig. 1 (curve *2*). Behavior of the work function during the adsorption O_2 on the surface of $TiO_2(110)$ is illustrated in the same figure by curve *3*. In the latter case, the model almost exactly describes the experimental data; the agreement between calculation and experiment for zinc oxide is also quite satisfactory. The corresponding variation of the charge of an oxygen admolecule is shown in Fig. 2.

Discussion. The results of calculations showed that the charge transfer between adsorbed species and the substrate is quite small, which is analogous to the behavior known in metals [9]. For this reason, the half-width of the quasi-level of an isolated adsorbed particle is much smaller than that observed for the adsorption of alkali metals on semiconductors [4–6]. However, it is unclear why the experimental values of $\Delta\phi(\Theta)$ for the adsorption of oxygen on zinc oxide and titanium oxide differ by almost one order of magnitude. For this reason, we have to select greater values of Φ and ξ (on the order of analogous parameters for the adsorption of alkali metals on semiconductors) for the $O_2/ZnO(10\bar{1}0)$ system. Apparently, this system is characterized by a significant influence of defects, which lead to the situation described in the introduction.

In accordance with the fact that hydrogen atoms donate electrons to the substrate, while oxygen molecules accept electrons from the substrate, the surface conductivity of these oxides σ in the former case increases, and in the latter case, decreases with increasing coverage. This response is used in semiconductor gas sensors of the resistive type. Figure 3 shows plots of the product $|Z(\Theta)|\Theta$, which is proportional to the change $\Delta\sigma$ in the surface conductivity. The results of calculations qualitatively agree with the experimental situation (see [1, 3]).

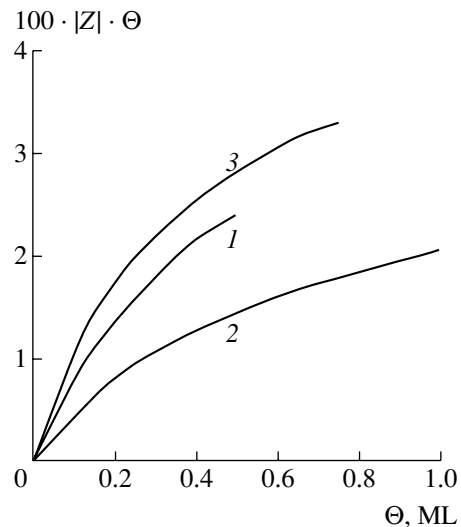In conclusion, it should be noted that, to the best of our knowledge, changes in the work function of the

Fig. 3. Plots of the product $|Z(\Theta)|\Theta$ (proportional to the change $\Delta\sigma$ in the surface conductivity) versus adsorption coverage Θ for various gas/oxide systems (notation as in Fig. 1).

gas/oxide system in the course of adsorption are calculated for the first time.

REFERENCES

1. V. E. Henrich and P. A. Cox, *The Surface Science of Metal Oxides* (Cambridge Univ. Press, Cambridge, 1994).
2. H.-J. Freund, H. Kuhlenbeck, and V. Staemmler, Rep. Prog. Phys. **59**, 283 (1996).
3. W. Göpel, Prog. Surf. Sci. **20**, 9 (1985).
4. S. Yu. Davydov and A. V. Pavlyk, Fiz. Tekh. Poluprovodn. (St. Petersburg) **35**, 831 (2001) [Semiconductors **35**, 796 (2001)].
5. S. Yu. Davydov and I. V. Noskov, Pis'ma Zh. Tekh. Fiz. **27** (20), 1 (2001) [Tech. Phys. Lett. **27**, 844 (2001)].
6. S. Yu. Davydov and I. V. Noskov, Zh. Tekh. Fiz. **72** (11), 137 (2002) [Tech. Phys. **47**, 1481 (2002)].
7. S. Yu. Davydov, Poverkhnost, No. 8, 17 (1991).
8. O. M. Braun and V. K. Medvedev, Usp. Fiz. Nauk **157**, 631 (1989) [Sov. Phys. Usp. **32**, 328 (1989)].
9. L. A. Bol'shov, A. P. Napartovich, A. G. Naumovets, and A. G. Fedorus, Usp. Fiz. Nauk **122**, 125 (1977) [Sov. Phys. Usp. **20**, 432 (1977)].

Translated by P. Pozdeev

The Effect of Neutron Irradiation on the Microhardness of Gallium Arsenide

Z. V. Jibuti, N. D. Dolidze, N. Sikhuashvili, and G. L. Eristavi

Tbilisi State University, Tbilisi, Georgia
e-mail: nugo@geo.net.ge
Received March 16, 2004

Abstract—We have studied the effect of neutron irradiation on the microhardness of n-GaAs crystals. It is shown that the growth and saturation of microhardness with increasing radiation dose Φ, as previously reported in the literature, take place only in the dose range $\Phi \sim 10^{15}$–5×10^{16} cm^{-2}. As the neutron dose is increased further, the microhardness continues to grow due to the increasing role of the radiation-induced disordered regions in n-GaAs. © 2004 MAIK "Nauka/Interperiodica".

As is known, radiation not only significantly influences the electrical and optical properties of semiconductors but also affects all other structure-sensitive characteristics, such as, in particular, mechanical properties of crystals [1–3]. Previous investigations of the effect of neutron radiation on the microhardness H of GaAs at relatively low doses ($<2 \times 10^{15}$ cm^{-2}) [3] showed that H increases with the dose and exhibits saturation after irradiation to $\sim 10^{15}$ cm^{-2}. An analogous behavior of the microhardness of GaAs was observed in the case of γ irradiation [2].

We have studied the effect of neutron irradiation on the microhardness of GaAs at 70°C in a broad range of doses Φ from 10^{15} up to 1.25×10^{18} cm^{-2}. The experiments were performed with undoped n-type GaAs crystals with a carrier density of 10^{15} cm^{-3} and a dislocation density of 10^4 cm^{-2}. The microhardness was measured on a (111) plane with a Durimet setup using the standard Knoop indentation technique with a pyramid loaded in the range from 15 to 300 g.

Figures 1 and 2 show plots of the microhardness H and its relative variation ($\Delta H/H$) versus neutron dose Φ for GaAs. The results of our measurements show (Fig. 1) that, when the dose reaches $\Phi \sim 10^{15}$ cm^{-2}, the microhardness exhibits saturation, in agreement with the behavior reported in [3]. However, subsequent increase in the dose to 5×10^{16} cm^{-2} leads to a new increase in H, with a sharp growth in the range of $\Phi > 10^{17}$ cm^{-2}. Thus, the microhardness exhibits saturation only in the interval of doses within $\Phi \sim 10^{15}$–5×10^{16} cm^{-2}. It should also be noted that the growth of microhardness in GaAs irradiated to doses above $\Phi \sim 10^{16}$ cm^{-2} is observed in the entire range of indenter loads (Fig. 2).

The observed increase in the microhardness of irradiated GaAs may be caused both by a decrease in the

mobility of dislocations and by their pinning at the point radiation defects (predominantly, vacancies) [3]. In the case of neutron irradiation at relatively low doses ($<5 \times 10^{16}$ cm^{-2}), point defects generated in the crystal outside the disordered regions apparently play a greater role in this process. As the radiation dose increases, the disordered regions begin to overlap and the volume occupied by these regions becomes significant. The concentration of point defects (of the V_{Ga} or V_{As} vacancy type) in these regions becomes much greater than in the main volume [4–6]. As a result, the effect of these defects on the mobility of dislocations increases, which is manifested by a significant increase in the microhardness of irradiated crystals. In addition, the radiation defects produced by neutrons create internal strain fields analogous to external compression, which also lead to an increase in the microhardness [7, 8].

It should be noted that an increase in the microhardness of irradiated crystals could also be related to an
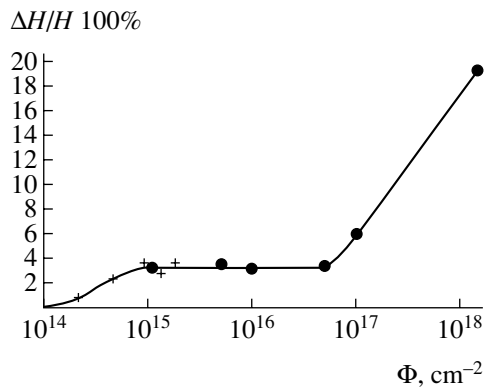

Fig. 1. Plot of the relative change of microhardness versus radiation dose for GaAs irradiated by fast neutrons. Black circles show the experimental points obtained in this study; crosses show the data taken from [3].
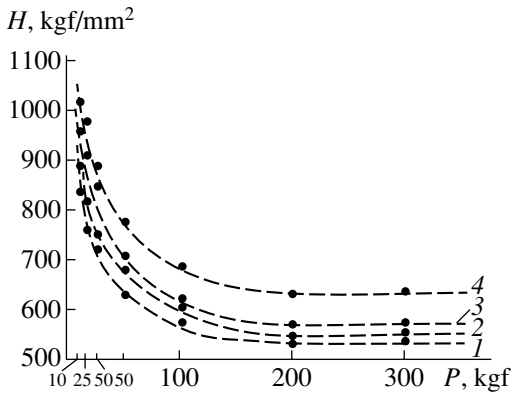
Fig. 2. Plot of the microhardness versus indenter load for GaAs irradiated by fast neutrons at various doses $\Phi = 0$ (*1*), 5×10^{16} (*2*), 10^{17} (*3*), and 1.25×10^{18} cm^{-2} (*4*).

increase in the density of dislocations under the action of radiation [1]. However, it was demonstrated [5] that the neutron irradiation of GaAs does not change the density of dislocations in this material.

REFERENCES

1. M. A. Krivov, G. I. Potakhova, and L. P. Rybkina, Izv. Vyssh. Uchebn. Zaved. Fiz. **1**, 190 (1966).
2. I. A. Domoryad, *The Effect of Radiation on Substance* (FAN, Tashkent, 1970), pp. 27–29 [in Russian].
3. N. N. Sirota, N. F. Kurilovich, and G. M. Berezina, Dokl. Akad. Nauk BSSR **19**, 880 (1975).
4. R. Coates and E. W. J. Mitchell, Adv. Phys. **24**, 593 (1975).
5. V. P. Klad'ko and S. V. Plyatsko, Fiz. Tekh. Poluprovodn. (St. Petersburg) **32**, 261 (1998) [Semiconductors **32**, 235 (1998)].
6. K. D. Glinchuk and A. V. Prokhorovich, Fiz. Tekh. Poluprovodn. (St. Petersburg) **31**, 533 (1997) [Semiconductors **31**, 449 (1997)].
7. Z. V. Jibuti, N. D. Dolidze, B. E. Tsekvava, and G. L. Eristavi, Pis'ma Zh. Tekh. Fiz. **29** (13), 26 (2003) [Tech. Phys. Lett. **29**, 540 (2003)].
8. M. S. Ablova, *Microhardness Testing Methods and Devices* (Nauka, Moscow, 1965), pp. 237–244 [in Russian].

Translated by P. Pozdeev

Electron Chemoemission from Metal to Semiconductor

V. F. Kharlamov*, S. N. Romashin, and A. V. Sedov

Orel State Technical University, Orel, Russia
* e-mail: kharl@ostu.ru
Received January 14, 2004; in final form, March 29, 2004

Abstract—A method of monitoring hot electron generation in a metal, accompanying a chemical reaction on the metal surface, is proposed. The phenomenon of electron chemoemission from metal to semiconductor has been observed. The effect of conversion of the energy liberated on the surface of a metal catalyst into the electric energy is found. © *2004 MAIK "Nauka/Interperiodica".*

According to theoretical notions of heterogeneous chemical reactions at the metal–gas interface, molecules formed in the course of these reactions are stabilized predominantly at the expense of production of electron–hole pairs rather than phonons [1–3]. In view of the small electron energy relaxation time in metals ($\tau \sim 10^{-12}$ s at $T = 300$ K [4]), hot electrons account for a negligibly small fraction (10^{-11} under the conditions of experiments described below) of their total number. For this reason, methods capable of monitoring the formation of hot electrons in the course of chemical conversions on the surface of solids have practically not been developed.

We have solved this problem by extracting hot electrons from a metal (catalyzing a given reaction) into a semiconductor via a potential barrier at the interface. For this purpose, the semiconductor surface was covered by a thin metal film with a thickness satisfying the condition $d \ll \tau\vartheta$, where ϑ is the velocity of electrons in the metal. The generation of hot electrons was studied using the heterogeneous reaction $H + H \longrightarrow H_2$.

The experiments were performed on p-type germanium with a resistivity of $1\ \Omega$ cm, n-type silicon with a resistivity of $100\ \Omega$ cm, and planar p–n junctions prepared by diffusion techniques in silicon. The thickness of all semiconductor crystals was 0.4 mm, while the area of the large face (face b) varied within $S = 2$–100 mm^2. Using thermal deposition in vacuum, face b was covered by nickel. The metal film thickness d was varied within 10^{-7}–10^{-8} m. The surface of some semiconductor crystals was coated by a natural oxide film formed as a result of interaction with air [5], while other samples were deprived of this oxide by means of etching with $HNO_3 + HF$ acid mixture. Control experiments were performed with semiconductors not covered by nickel (which corresponds to $d = 0$). The crystal surface opposite to face b was provided with an ohmic contact. The deposited metal layer contacted with 0.8-mm-thick copper clamp electrode. All faces except b were protected by a layer of epoxy resin. In what follows, R_n

denotes the resistance of the metal–semiconductor–metal (MSM) structure connected to a measuring circuit so that minus of the bias voltage source ($V = 1.5$ V) is on the nickel film; R_p is the resistance of the sample structure measured with plus of the source connected to the nickel film. In all samples, the R_n and R_p values differed at least by a factor of 10. The samples were also characterized by the photo emf and thermo emf values.

The experimental setup was analogous to that described in [6]. The MSM structures were connected into a measuring circuit (UPIP-60M dc bridge or F 116 microvoltmeter) and placed into a flow reactor purged by spectral-purity hydrogen at a pressure of 50 Pa. The reactor walls could be heated up to 500 K. Hydrogen molecules were dissociated ($H_2 \longrightarrow 2H$) in a high-frequency gas discharge. The optical emission from discharge was absorbed by the Wood horn. The absence of illumination of the sample by light emitted from the discharge region was checked with the aid of a photomultiplier. While diffusing from the discharge to reactor, each vibrationally and/or electronically excited molecule was involved in no less that 10^3 collisions with gas molecules and lost the excess energy [7]. The results of special experiments showed that electrons and ions from discharge plasma exhibited recombination and did not enter the reactor. Indeed, at a voltage of 100 V applied between Ni film and an additional electrode placed above this film, the current in the gas phase was below the sensitivity of measuring equipment (1×10^{-14} A). The concentration of hydrogen atoms in the reactor measured by thermoprobe was 3×10^{13} cm^{-3}. Prior to measurements, the samples were exposed for 2 h to an atmosphere containing atomic hydrogen in order to clean Ni films from adsorbed molecules (oxygen, water, etc.) through the formation of volatile hydrides and sputtering of the adlayer in the course of this reaction [8]. Bringing the samples in contact with a thermocouple or a thermoresistor showed that the increase in the sample temperature due to the reaction proceeding on the surface of nickel was about 0.2 K. In

the course of experiments, we measured (i) the time variation of R_n and R_p of the MSM structure after switching the source of atomic hydrogen on and off, (ii) the behavior of R_n and R_p in response to illumination of the nickel film by the light of an incandescent lamp, (iii) the potential difference (chemo emf) arising between contacts of the MSM structure in the course of the reaction, and (iv) the short-circuit current related to chemo emf.

Switching of the source of atomic hydrogen produced no (or very insignificant) effect on the R_p values of any MSM structures and on the R_n value of germanium-based structures. Under the same conditions, R_n of the samples based on n-type silicon or p–n-Si junctions exhibited significant changes (ΔR_n). When the reactor temperature was increased, R_n rapidly (and reversibly) decreased; for $T \geq 390$ K, switching of the source of H atoms only slightly influenced the resistance of these MSM structures. The most pronounced changes in R_n under the action of H atoms were observed for MSM structures with a nickel film thickness of $d = 3 \times 10^{-8}$ m. The shape of the $R_n(t)$ curves is well reproduced in the course of repeated measurements (Fig. 1). The phenomenon of hydrogen-induced changes in R_n is not observed if the natural oxide film is not removed from the substrate surface prior to nickel deposition. In the case of both "thin" ($d = 1 \times 10^{-8}$ m) and "thick" ($d = 1 \times 10^{-7}$ m) metal films, as well as in the absence of nickel film ($d = 0$), the action of H atoms on the MSM structure is not accompanied by changes in the R_n and R_p values. After switching on the source of H atoms, the change in the electric current passing through the MSM structure is $\Delta I \approx V R_n^{-2} \Delta R_n = 10^{-8}$–$10^{-4}$ A. This is six to ten orders of magnitude greater than the upper limit of a current related to the penetration of charged particles from plasma to reactor.

In the course of the atomic hydrogen recombination reaction $H + H \longrightarrow H_2$ proceeding on the surface of a nickel film deposited onto a germanium substrate, the film acquires a positive charge, germanium is charged negatively, and a chemo emf is developed. The magnitude of this chemo emf decreases with increasing temperature (cf. curves 1 and 2 in Fig. 2). At the same time, the short-circuit current related to the development of chemo emf increases with the temperature (cf. curves $1*$ and $2*$ in Fig. 2). For all silicon-based MSM structures, neither chemo emf nor short-circuit current are observed ($U < 10^{-8}$ V, $I_U < 10^{-9}$ A). It was established that, in germanium-based MSM structure, the potential barrier for electrons at the interface is small or absent due to the band bending downward. This accounts for the development of chemo emf as a result of the escape of hot electrons (appearing in the course of the catalytic reaction) from metal to semiconductor. In the case of silicon-based MSM structures, a potential barrier exists at the nickel–silicon interface that
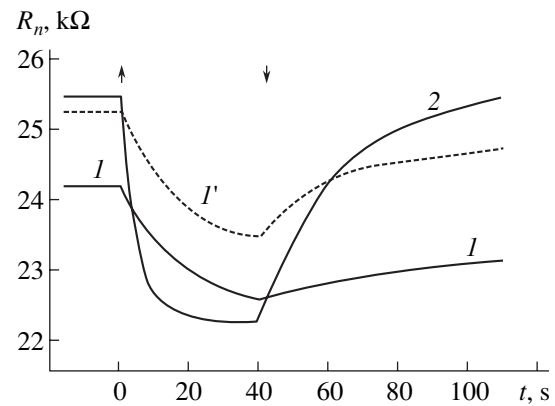

Fig. 1. Time variation of the resistance R_n ($T = 295$ K) of the Ni film–p-Si–n-Si (MSM) structure with a film thickness of $d = 3 \times 10^{-8}$ m (with minus of the bias voltage on Ni) observed when the source of H atoms is switched on ($\uparrow$) and off ($\downarrow$): (1) first run; (2) second run after 2-h exposure of the MSM structure to H atoms; ($1'$) R_n variation in response to illumination switched on for the same period of time.
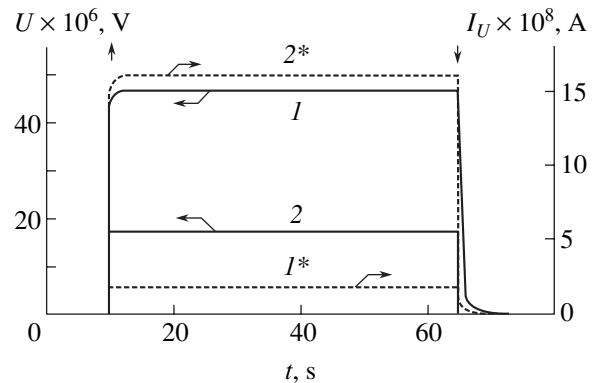

Fig. 2. Time variation of (1, 2) the potential difference U between contacts of the Ni film–p-Ge structure with a film thickness of $d = 3 \times 10^{-8}$ m and ($1*$, $2*$) the short-circuit current in this structure measured by a galvanometer when the source of H atoms is switched on ($\uparrow$) and off ($\downarrow$): (1, $1*$) $T = 295$ K; (2, $2*$) $T = 350$ K.

accounts for the absence of chemo emf in these structures.

The aforementioned thin films exhibit no metal-like surface conductivity and, hence, probably possess a mosaic structure. Therefore, the phenomenon of variation of the R_n value under the action of hydrogen atoms is observed only in the presence of a continuous nickel film in electric contact with silicon. Penetration of hydrogen atoms to the surface of silicon does not lead to this effect. The changes in R_n of the MSM structures observed in the presence of hydrogen cannot be induced by an increase in the temperature of silicon as a result of the exothermal process $H + H \longrightarrow H_2$ on the nickel film. This statement is confirmed by the absence of the influence of H atoms on the resistance of MSM structures containing oxide films and the structures

with thin and thick Ni films (these films also exhibit heating when exposed to H atoms). It should also be noted that the resistance of the p–n junction was several orders of magnitude greater than the Ni–Si contact resistance. Therefore, the diffusion of H atoms through the nickel film and their possible adsorption at the Ni–Si interface (influencing the contact potential difference and, hence, the contact resistance [5]) cannot affect the resistance of MSM structures containing the p–n junction.

Under the experimental conditions studied, switching of the source of atomic hydrogen on and off was accompanied by jumplike changes in the rate J of their heterogeneous recombination on the nickel surface. As a result, the kinetic curve $J(t)$ has the shape of rectangular pulses [9] coinciding with the $U(t)$ and $I_U(t)$ kinetics (Fig. 2). Therefore, Ni film exhibits virtually nondelayed charging in the course of the reaction. The shape of the $R_n(t)$ curves is determined by the kinetics of the electron processes on the surface and in the bulk of the semiconductor, which are related to the formation of hot electrons on the metal surface in the course of the heterogeneous reaction $H + H \longrightarrow H_2$ and their penetration under the action of the electric field into the semiconductor through a potential barrier at the metal–semiconductor interface. This is confirmed by correlated variation of the curves of photo- and chemoconductivity (Fig. 1). The time-delayed relaxation of photo- and chemoconductivity is explained by the presence of electron traps. In the case of Ni films on the surface of p–n-Si junctions, the decrease in R_n during the surface reaction is related to the penetration of hot electrons to the most high-ohmic region (p–n junction) of this structure. At $T \geq 390$ K (and in structures with thick nickel films), the effect of H atoms on the R_n value is absent because hot electrons exhibit relaxation in the film (where the condition $d \ll \tau\vartheta$ is no longer valid).

The results of measurements were described using the relations

$$\Delta I = e\eta\eta_1 JS, \quad J = 0.25cu\gamma, \quad \Delta I \approx VR_n^{-2}\Delta R_n,$$

where ΔI is the change in the current caused by the penetration of hot electrons from metal to semiconductor; e is the electron charge; η is the probability of hot electron generation as a result of chemical conversion on the surface; η_1 is the probability of hot electron penetration through the MSM structure during the electric current passage; J is the rate of the surface heterogeneous reaction; S is the area of the metal film; c is the concentration of H atoms in the gas phase; u is the average velocity of the thermal motion of H atoms in the gas phase; γ is the coefficient of heterogeneous recombination of H atoms on the metal surface; V is the voltage applied to the MSM structure, $V = 1.5$ V; and ΔR_n is the change in the MSM structure resistance under the action of H atoms. Taking the value $\gamma = 0.1$ [10], and the results of measurements $S = 2$ mm^2, $R_n = 25$ kΩ, $\Delta R_n = 3$ kΩ (see curve 2 in Fig. 1), we obtain an estimate for a Ni film deposited onto a p–n-Si junction: $\eta\eta_1 = 1 \times 10^{-2}$.

REFERENCES

1. W. Brenig, Z. Phys. B **23**, 361 (1976).

2. M. A. Kozhushner, V. G. Kustarev, and B. R. Shub, Dokl. Akad. Nauk SSSR **237**, 871 (1977).

3. E. M. Lifshitz and L. P. Pitaevskiĭ, *Physical Kinetics* (Nauka, Moscow, 1979; Pergamon Press, Oxford, 1981).

4. V. L. Bonch-Bruevich and S. G. Kalashnikov, *Physics of Semiconductors* (Nauka, Moscow, 1990) [in Russian].

5. V. F. Kharlamov, I. A. Makushev, A. V. Barmin, *et al.*, Pis'ma Zh. Tekh. Fiz. **29** (7), 87 (2003) [Tech. Phys. Lett. **29**, 305 (2003)].

6. P. Borrell, *Molecular Relaxation Processes* (Chem. Soc., London, 1966), p. 263.

7. V. F. Kharlamov, L. Yu. Frolenkova, and T. S. Rogozhina, Zh. Tekh. Fiz. **71** (10), 90 (2001) [Tech. Phys. **46**, 1294 (2001)].

8. V. F. Kharlamov, E. P. Krutovskiĭ, Yu. V. Mosin, *et al.*, Pis'ma Zh. Tekh. Fiz. **24** (5), 23 (1998) [Tech. Phys. Lett. **24**, 176 (1998)].

9. M. U. Kislyuk, Khim. Fiz. **8**, 59 (1989).

Translated by P. Pozdeev

Synergetic Description of Temperature Evolution in Strongly Inhomogeneous Media

S. O. Gladkov

Moscow State Regional University, Moscow, Russia
Received February 10, 2004

Abstract—A nonlinear differential heat conduction equation is phenomenologically derived proceeding from the general principles of construction of the action S invariant with respect to the operation of inversion $I(\mathbf{x} \longrightarrow -\mathbf{x})$. Based on this equation, the dynamics of temperature evolution in a nonstationary case is analyzed. This approach reveals some general laws of the physical behavior of such systems, which can be used for the description of irreversible phenomena involved in self-organization processes. This situation can be realized, for example, in strongly inhomogeneous structures featuring stochastic internal heat fluxes. © *2004 MAIK "Nauka/Interperiodica".*

In investigations of the evolution of various physical processes, it is important to assess the degree of determinacy of the system under consideration. All mechanical and quantum-mechanical systems obey time-reversible (i.e., invariant with respect to the operation of time inversion: $t \longrightarrow -t$) equations of motion. In the former case, this is Newton's second law, and in the latter case, the Schrödinger equation. For this reason, these equations can provide a description only of the time-reversible dynamics. As for irreversible processes, such as heat conduction or diffusion, they are characterized (according to Prigogine [1]) by the absence of the "time arrow," which mathematically implies the interval $t \in (-\infty, +\infty)$. This is the basic difference in mathematical descriptions of reversible and irreversible phenomena, whereby the dynamical system under consideration either possesses a past (reversibility) or not (irreversibility).

A characteristic feature inherent in all reversible processes is the dynamical stability of the equilibrium state, which implies that the system, when subjected to various perturbations, "slides down" to a certain potential well representing stable equilibrium. For a stable equilibrium state of a system (mechanical or quantum-mechanical) containing a large number of objects (e.g., a system of N particles), the number of trajectories is insignificant (there can be a single trajectory) and the basic point is the very fact that a given object comes to a final (equilibrium) point (p_0, q_0) in the phase space. For a system containing only one particle, this is a real point, while for N particles, this is a scaled point (p_0, q_0) determined both by the probabilistic character of motion and by a certain "volume" representing a local region of phase space $\Delta\Gamma_0$ to which, according to the ergodic hypothesis, all trajectories come after a rather long but finite time interval Δt (despite the fact that the motion of the whole system is highly sensitive to the initial conditions).

The situation is different when we turn to irreversible processes. A system, leaving an equilibrium state and performing (in the general case) an infinite motion, may get anywhere except the region close to the initial phase volume $\Delta\Gamma_0$ from which the dissipation has started.

Despite apparently well-established laws of the behavior of reversible and irreversible processes, there are some exceptions from the general rules. Indeed, in the description of purely dissipative phenomena over large positive times, a point of principal importance is the fluctuational behavior of parameters (e.g., temperature and density) even when all relaxation processes have ceased and the equilibrium is reached. The system continues to perform chaotic walk over the entire phase region (this walk lasts an infinite time), not obeying the laws of deterministic chaos [2, 3], being sensitive to the initial conditions, and exhibiting only periodic variation of parameters. An example of such a system was recently [4] described for a homogeneous medium. For a system with the parameters inhomogeneously distributed in space, the situation substantially changes: the fluctuations are "suppressed" by this inhomogeneity and the system slides down to a certain equilibrium state [5].

This paper presents an example of the nonlinear self-organization of an irreversible process and reveals some laws in the variation of temperature considered within the framework of a nonstationary and nonlinear equation of heat conduction describing the system in the semi-infinite time interval $t \in [0, +\infty)$. This equation can be strictly derived from the variational principle using a phenomenological approach used, for example, in [6, 7].

In order to obtain the nonlinear differential heat conduction equation in the general form (capable of describing strongly inhomogeneous systems), let us use the aforementioned phenomenological approach and write the equation of "motion" for the temperature in the form $dT/dt = \delta Q/\delta T$, where the functional Q is determined by the invariant relation

$$Q\{T\} = \int_{t_0}^{t_1} \left\{ \frac{\chi}{2}(\nabla T)^2 + \frac{\lambda_1}{3}(\nabla T)^3 \right.$$
$$\left. + \frac{\lambda_2}{12}(\nabla T)^4 + \dots + \frac{\beta_1}{2}\dot{T}^2(\nabla T)^2 + \frac{\beta_2}{2}\dot{T}^2 + \frac{\beta_3}{2}\ddot{T}^2 \right\} d^3 x. \quad (1)$$

Here, λ and β are constants and χ is the thermal diffusivity.

To obtain the desired equation, let us use the definition of a variational derivative in the form $\delta J/\delta y = F_y$, where $F_y = \delta F/\delta y$ and the functional is defined by the relation $J\{y\} = \int_{x_0}^{x_1} F\,dx$ (by analogy with the procedure described in monograph [8]). By varying Q with respect to the temperature, we obtain the following nonlinear equation describing evolution of the temperature in space and time:

$$\dot{T} = \chi\Delta T + \lambda_1\nabla T\Delta T + \lambda_2(\nabla T)^2\Delta T + \dots - \beta\ddot{T}(\nabla T)^2$$
$$- \beta_1\dot{T}^2\Delta T - 4\beta_1\dot{T}\nabla T\nabla\dot{T} - \beta_2\ddot{T} + \beta_3\ddot{T} + \dots. \quad (2)$$

There may arise a suspicion that Eq. (2) does not describe reality, but this fear is certainly unjustified. The matter of fact is that nonlinear heat fluxes always exist in strongly inhomogeneous systems (such as, e.g., composites or porous media) in the case when chaotic motion of heat flows takes place inside a body. Outgoing from various local internal regions, these flows exhibit mixing that can give rise to a kind of resonance (so-called synchronization) leading (as will be shown below) to a spontaneous increase and oscillation in the temperature even despite the fact that the body is placed into a thermostat (!). However, after a sufficiently long period of time, the temperature of the sample as a whole will be established equal to the temperature of the thermostat.

The question is how to model this situation mathematically. An answer is provided by the following considerations.

Let us somewhat simplify Eq. (2) using a simple formal approach, whereby the sum of terms involving various powers of the temperature gradient is assumed to be equal to a sum of terms of a geometric progression,

$$\chi + \lambda_1\nabla T + (\lambda_2\nabla T)^2 + \dots = \frac{\chi}{1 + \lambda\nabla T},$$

where λ is a new constant vector parameter of the corresponding dimension. Now, let us make another model assumption and pass to a finite difference equation by eliminating spatial derivatives using a simple rule: $\lambda\nabla E = -\lambda(T - T_0)/\delta$ and $\Delta T = -(T - T_0)/\delta^2$, where δ is the thickness of a region of the contact between the body and the thermostat occurring at the temperature T_0. Since we have passed to the equation of heat exchange, it will be convenient to use (instead of the thermal diffusivity) the heat transfer coefficient defined as $\alpha = \kappa/\delta^2 c_p$, where κ is the thermal conductivity and c_p is the isobaric heat capacity per unit volume. Eventually, we arrive at a much simpler, but still nonlinear, second-order differential equation describing the dynamics of temperature variation in strongly inhomogeneous media:

$$\dot{T} = -\frac{\alpha(T - T_0)}{1 + \frac{\lambda}{\delta}(T - T_0)} - \beta_1\ddot{T}\left(\frac{T - T_0}{\delta}\right)^2$$
$$- 3\beta_1\dot{T}^2\frac{(T - T_0)}{\delta^2} - \beta_2\ddot{T} + \beta_3\dddot{T}.$$

This equation can be conveniently written in dimensionless from by introducing the new function $y = (T - T_0)/T_0$ and dimensionless variables $\lambda_0 = \lambda T_0/\delta$, $K_1 = \alpha\beta_1 T_0^3/\delta^2$, $K_2 = \beta_3 T_0$, and $K_3 = \beta_2 T_0^2$ dimensionless time $\tau = \alpha t$. As a result, we obtain the equation

$$\dot{y} + (K_1 y^2 + K_3)\ddot{y} + 3K_1 y\dot{y}^2 - K_2\dddot{y} + \frac{y}{1 + \lambda_0 y} = 0, \quad (3)$$

where upper dots indicate differentiation with respect to the dimensionless time τ. The initial conditions are selected as follows: $y(0) = 1$ and $\dot{y}(0) = 0$. Note that the first condition corresponds to the initial temperature $T(0) = 2T_0$.

It should be emphasized that, for small λ_0 and $K_{1,2}$, Eq. (3) is equivalent to the usual Newton heat exchange equation, whereby the rate of temperature variation is proportional to the temperature: $\dot{y} + y = 0$. A solution to this equation is $y(\tau) = y(0)e^{-\tau}$, where $y(0)$ is the initial condition at $\tau = 0$.

As for Eq. (3), it is difficult to solve this equation for arbitrary $K_{1,2}$ and λ_0, and the analytical solution is still unavailable. However, the dependence $y(\tau)$ in a broad range of parameter s $K_{1,2,3}$ and λ_0 can be determined by numerical methods. Indeed, introducing the step h, passing from derivatives to finite differences by the formulas $\dot{y} = (y_{n+1} - y_n)/h$ and $\ddot{y} = (y_{n+2} - 2y_{n+1} + y_n)/h^2$, and

ignoring the fourth derivative with respect to time, we eventually obtain the following relation:

$$y_{n+2} = 2y_{n+1} - y_n - \frac{h^2}{Ky_n(1+\lambda_0)}$$
$$- \frac{3(y_{n+1} - y_n)^2}{y_n} - \frac{h(y_{n+1} - y_n)}{Ky_n^2}. \tag{4}$$

Numerical integration of iterative relation (4) is still a rather complicated task because of the presence of "poor" denominators. Let us consider the behavior of $T(t)$ qualitatively. In the case of small y, Eq. (3) yields the relation $\dot{y} + K_2\dddot{y} + K_3\ddot{y} + y = 0$ and the characteristic equation $K_2k^4 + K_3k^2 + k + 1 = 0K_2$. A solution of this algebraic equation for $K_2 = 27/256$ and $K_3 = 0$ is $k_1 = -4/3$, while the other three roots are imaginary and can be found from the equation $k_3 - \frac{4k^2}{3} + \frac{16k}{9} + \frac{64}{9} = 0$. Thus, we have obtained one partial solution, $y_1 = \exp(-4r/3)$, and three oscillating solutions, y_2, y_3, and y_4.

REFERENCES

1. G. Nicolis and I. Prigogine, *Self-Organization in Non-Equilibrium Systems* (Wiley, New York, 1977; Mir, Moscow, 1979).

2. H. G. Schuster, *Deterministic Chaos* (Physik-Verlag, Weinheim, 1984; Mir, Moscow, 1988).

3. M. R. Schroeder, *Number Theory in Science and Communication, with Applications in Cryptography, Physics, Digital Information, Computing and Self-Similarity*, 2nd ed. (Springer, Berlin, 1990).

4. S. O. Gladkov and I. V. Gladyshev, Zh. Tekh. Fiz. **71** (3), 1 (2001) [Tech. Phys. **46**, 273 (2001)].

5. S. O. Gladkov and I. V. Gladyshev, Zh. Tekh. Fiz. **71** (4), 1 (2001) [Tech. Phys. **46**, 363 (2001)].

6. S. O. Gladkov and A. M. Tokarev, Fiz. Goreniya Vzryva **1**, 30 (1990).

7. S. O. Gladkov, *Dielectric Properties of Porous Media* (Springer, Berlin, 2003).

8. B. A. Strukov and A. P. Levanyuk, *Ferroelectric Phenomena in Crystals: Physical Foundations* (Nauka, Moscow, 1995; Springer, Berlin, 1998).

Translated by P. Pozdeev

Photoelectron Spectroscopy of Thin-Film Yb–Si(100) Structures Formed by Solid Phase Epitaxy at 800 K

D. V. Vyalikh[a], M. V. Kuzmin[a], M. A. Mittsev[a,*], and S. L. Molodtsov[b]

[a] *Ioffe Physicotechnical Institute, Russian Academy of Sciences, St. Petersburg, 194021 Russia*
[b] *Institut für Festkoerperphysik und Fachrichtung Physik, Technische Universität Dresden,*
D-01062 Dresden, Germany
* e-mail: m.mittsev@mail.ioffe.ru
Received March 15, 2004

Abstract—Thin-film Yb–Si(100) structures formed by solid phase epitaxy at 800 K were studied by photoelectron spectroscopy using a synchrotron radiation source. Analysis of the photoelectron spectra showed that, in the range of submonolayer ytterbium coverages θ, the formation of two-dimensional ordered structures is accompanied by the destruction of surface dimers existing on a clean (2 × 1)-reconstructed Si(100) surface and (starting with the minimum coverage θ = 0.15) by the nucleation of silicides. In the layered structure of silicides, there is charge transfer from ytterbium to silicon layers. It is concluded that this charge transfer eventually accounts for the characteristic trident shape of the spectrum of Si 2*p* core level in silicides. © *2004 MAIK "Nauka/Interperiodica"*.

In recent years, much attention has been devoted to the investigation of thin-film structures formed by deposition of rare earth metals onto silicon surface. In most cases, such structures were obtained on a Si(111)7 × 7 surface, while a (2 × 1)-reconstructed Si(100) surface was studied to a much lower extent.

This paper presents the results of investigation of the growth mechanism and electron properties of thin-film structures formed upon deposition of ytterbium onto a Si(100)2 × 1 surface. In particular, we aimed at elucidating whether the valence of Yb atoms in the course of formation of these structures changes from 2+ to a certain fractional value $2 + x$, where $x < 1$. The investigation was performed using a variant of photoelectron spectroscopy (PES), whereby photoelectrons are excited by synchrotron radiation. To our knowledge, such investigations have not been reported to date.

Thin-film structures were created by deposition of ytterbium onto a Si(100)2 × 1 surface at room temperature under ultrahigh vacuum conditions, followed by heating of the samples for 3 min at 800 K. The experiments were performed using a photoelectron spectrometer and a synchrotron radiation channel of the Russian–German Laboratory at the BESSY II storage ring (Berlin, Germany). The overall energy resolution of the electron energy analyzer and monochromator was 150 meV. We measured the photoelectron spectra of the Si 2*p* core level, the valence band of silicon, and the Yb 4*f* level. In the first case, photoelectrons were excited by synchrotron radiation with a photon energy of $h\nu = 130$ eV, while the valence band and 4*f* level electrons were excited using the photons with $h\nu = 108$ eV. The state of the sample surface and the structure of surface films formed in the course of ytterbium deposition were monitored by low-electron energy diffraction (LEED).

The samples were prepared using *n*-type single crystal silicon plates with a resistivity of 1 Ω cm. Prior to experiments, the plates were heated in a vacuum chamber of the photoelectron spectrometer, first for 2 h at 900 K and then for a short time at 1450 K. This treatment ensured that an atomically clean Si(100)2 × 1 reconstructed surface was obtained. Ytterbium atoms were deposited onto the substrate surface by evaporation from tantalum Knudsen cells. The residual pressure in the spectrometer chamber during evaporator operation did not exceed 8×10^{-10} mbar. The rate of deposition was 0.01–0.08 monolayer per second (one monolayer coverage of Yb atoms corresponds to their surface density of 6.78×10^{14} cm^{-2}, which equals the density of silicon atoms on the Si(100) face). The PES measurements were performed at room temperature in a vacuum of 1×10^{-10} mbar.

Figure 1 shows the photoelectron spectra of Yb 4*f* and Si 2*p* levels observed for various surface coverages in the Yb–Si(100) system studied. Each spectrum is normalized to the maximum peak height. The spectra exhibit a number of peculiarities. In particular, our Yb 4*f* spectra, in contrast to those reported for the Yb–Si(111) system in [1], reveal the formation of three (rather than two) peaks already at minimum coverages (see the spectrum for θ = 0.15). The two most intense components are predominantly due to divalent Yb atoms involved in two-dimensional reconstructions [2]. The nature of third component with $E = 0.8$ eV will be considered below. Another peculiarity of the spectra of Yb 4*f* levels is their significant variation observed for
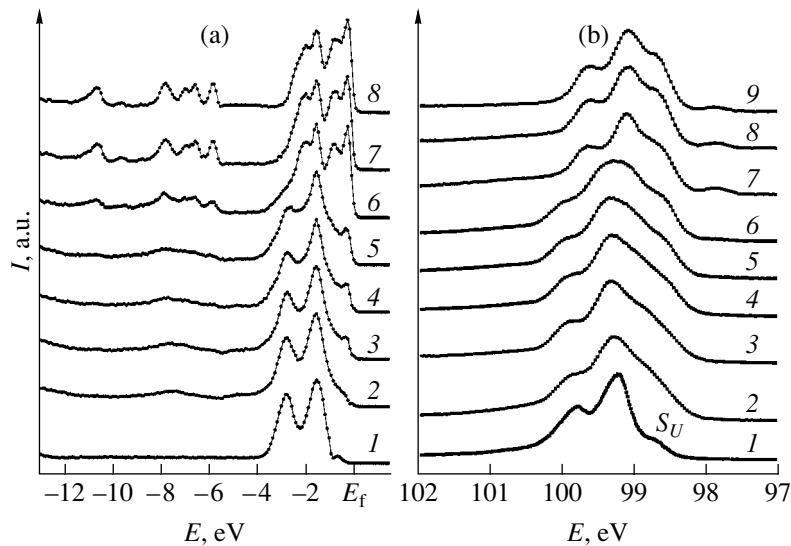
Fig. 1. Normalized photoelectron spectra of the Yb–Si(100) structures with various ytterbium coverages θ grown by solid phase epitaxy at 800 K: (a) Yb 4f level for θ = 0.15 (1), 0.3 (2), 0.5 (3), 0.7 (4), 1 (5), 3 (6), 8 (7), and 20 (8); (b) Si 2p core level for θ = 0 (1), 0.15 (2), 0.3 (3), 0.5 (4), 0.7 (5), 1 (6), 3 (7), 8 (8), 20 (9). The spectra were obtained using photon energies hν = 108 (a) and 130 eV (b); I is the photoelectron intensity, E is the binding energy, and E_f is the Fermi level energy.

the passage from small (θ < 1) to large (θ > 1) coverages leading to the formation of a surface silicide film [2]. However, these changes did not involve the peak with a binding energy of E = 0.8 eV. Moreover, the most pronounced growth of this peak with increasing amount of deposited ytterbium is observed in the range of coverages (θ > 1) corresponding to the aforementioned changes. The third peculiarity of the Yb 4f spectrum is the presence of peaks in the region of binding energies E = 6–12 eV. These peaks have small amplitudes at θ < 1 but significantly increase when θ > 1. These signals are due to trivalent Yb atoms [3, 4].

Analysis of the observed evolution of spectra leads to several conclusions concerning the properties of the Yb–Si(100) system heated to a high temperature in various stages of formation of two-dimensional surface structures. First, the presence of peaks in the region of binding energies E = 6–12 eV indicates that Yb atoms in silicide films formed on the Si(100) surface exhibit fractional valence ν. The ratio of areas under the peaks of divalent and trivalent atoms shows that 2 < ν < 2.5. In addition, simultaneous correlated growth of these areas shows that the fractional valence is homogeneous and, hence, Yb atoms occupy equivalent positions in the silicide film.

Another important conclusion following from an analysis of the spectra presented in Fig. 1a is that silicide nucleates on the Si(100) face already for the minimum coverages studied. This is evidenced by the peak at E = 0.8 eV, which is present in the spectra of samples with all ytterbium coverages. The same is evidenced by the peaks of trivalent ytterbium, which appear in the spectra already for θ = 0.3. These results imply that the Y–Si(100) system is qualitatively different from the

Yb–Si(111) system, where the growth of silicide begins only at θ > 0.5, that is, after the formation of the most dense reconstruction (2 × 1) matched with the substrate surface structure [5, 6].

As can also be seen from the data in Fig. 1a, the photoelectron spectra vary rather insignificantly for θ > 3. This result indicates that the silicide film corresponding to a coverage of θ = 3 is practically continuous and, hence, the substrate no longer contributes to the spectra. The same conclusion follows from an analysis of the Si 2p spectra presented in Fig. 1b. Indeed, the spectra observed for θ = 3 and 20 are virtually identical. At small coverages, the evolution proceeds as follows. For minimum doses of the deposited metal, the shoulder denoted as S_U (which is inherent in the spectrum of clean Si(100) surface and is due to the surface dimers [7, 8]) transforms into an extended tail with weakly pronounced structure. This behavior indicates that even small metal coverages destruct dimers. Considerable extension of the tail is related to the fact that Si atoms forming these dimers (and, probably, Si atoms of subsurface layers) are incorporated into various structures formed on the substrate surface in the course of deposition of Yb atoms. These structures include two-dimensional reconstructions of several types [2] and three-dimensional nuclei of silicides. Evidently, the binding energies of Si 2p electrons in such structures are different. As the coverage increases, a step appears on the tail. The formation of this step is accompanied by broadening of the central peak, which is most clearly manifested at θ = 1. For θ > 1, the central peak exhibits narrowing and the whole spectrum shifts toward lower binding energies. This transformation reflects the gradual transition from pure silicon to silicide. As was noted

above, the spectra of silicide acquire their final shape at $\theta = 3$.

The shape of the spectra of Si $2p$ levels in silicides indicates that the signal consists of at least two doublets. We believe that the most probable explanation of this is as follows. As is known, the structure of ytterbium silicides comprises alternating layers of metal and silicon atoms [7]. Since Si atoms are much more electronegative than Yb atoms, charge transfer from metal to silicon atoms takes place. This charge transfer must be accompanied by a decrease in the binding energies of electrons on the Si $2p$ level and, hence, by a shift of the spectrum toward lower binding energies (relative to the spectrum of clean silicon surface). If the surface of the silicide film exposes the layer of Yb atoms (which is confirmed by our data on the work function [2]) and the character of relaxation in this layer is such that atoms are pulled into the film (this case is most frequently encountered [8]), then the spacing between atoms of the uppermost layer of the film and the adjacent layer of Si atoms will be smaller than the corresponding distance in the bulk of this film. As a result, the charge transfer from metal to silicon in the Si layer closest to the surface will increase and the binding energy of electrons on the Si $2p$ levels will accordingly decrease compared to the bulk value. If this difference is sufficiently large, the signal from subsurface Si atoms in the photoelectron spectra will appear as a separate peak shifted toward lower energies relative to the peaks due to bulk silicon layers. We believe that this very shift accounts for the observed trident shape of the spectrum of silicides.

Based on the above considerations, we can also formulate more general conclusions concerning the shape of the Si $2p$ spectra in silicides. In the case of a silicide possessing a layered structure, the shape of the spectrum will depend on the difference $\Delta\chi$ of electronegativities of silicon and metal. If this difference is large, the spectrum will acquire a trident shape; otherwise, the spectrum will consist of two peaks. The first case is realized in the Yb–Si(100) system ($\Delta\chi = 0.8$) considered in this study, as well as in Yb–Si(111) [9] and Sm–Si(111) systems ($\Delta\chi = 0.7$) [10]. The second case was observed in the Co–Si(100) system ($\Delta\chi = 0$) [11, 12].

Thus, the experimental results obtained in this study show that the formation of two-dimensional ordered structures is accompanied by the destruction of surface dimers existing on a clean (2×1)-reconstructed Si(100)

surface and (starting with the minimum coverage $\theta = 0.15$) by the nucleation of silicides. Photoelectron spectra of the Si $2p$ core level in silicides are shifted toward lower binding energies relative to the spectra of pure silicon. This is evidence of a charge transfer from ytterbium to silicon layers in the layered structure of silicides. It is concluded that this charge transfer accounts for the characteristic trident shape of the spectrum of Si $2p$ core level in silicides.

REFERENCES

1. C. Wigren, J. N. Andersen, R. Nyholm, *et al.*, Phys. Rev. B **48**, 11014 (1993).

2. M. Kuzmin, R. E. Perälä, P. Laukkanen, *et al.*, Appl. Surf. Sci. **214**, 196 (2003).

3. C. Wigren, J. N. Andersen, R. Nyholm, *et al.*, J. Vac. Sci. Technol. A **9**, 1942 (1991).

4. R. Hofmann, W. A. Henle, F. P. Netzer, *et al.*, Phys. Rev. B **46**, 3857 (1992).

5. M. V. Kuzmin, M. V. Loginov, and M. A. Mittsev, Pis'ma Zh. Tekh. Fiz. **21** (19), 73 (1995) [Tech. Phys. Lett. **21**, 803 (1995)].

6. T. V. Krachino, M. V. Kuzmin, M. V. Loginov, and M. A. Mittsev, Fiz. Tverd. Tela (St. Petersburg) **39**, 256 (1997) [Phys. Solid State **39**, 224 (1997)].

7. G. Rossi, Surf. Sci. Rep. **7**, 1 (1987).

8. A. Bechshtedt and R. Enderlein, *Semiconductor Surfaces and Interfaces. Their Atomic and Electronic Structures* (Academie-Verlag, Berlin, 1988; Mir, Moscow, 1990).

9. L. Braicovich, I. Abbati, C. Carbone, *et al.*, Surf. Sci. **168**, 193 (1986).

10. C. Wigren, J. N. Andersen, R. Nyholm, *et al.*, Surf. Sci. **293**, 254 (1993).

11. M. V. Gomoyunova, I. I. Pronin, N. R. Gall, *et al.*, Pis'ma Zh. Tekh. Fiz. **29** (12), 25 (2003) [Tech. Phys. Lett. **29**, 496 (2003)].

12. M. V. Gomoyunova, I. I. Pronin, N. R. Gall, *et al.*, Fiz. Tverd. Tela (St. Petersburg) **45**, 1519 (2003) [Phys. Solid State **45**, 1596 (2003)].

Translated by P. Pozdeev

Reconstructing an Object Image Using the Laser Speckle Pattern of the Diffraction Field

B. B. Gorbatenko, V. P. Ryabukho, and L. A. Maksimova

Saratov State Technical University, Saratov, Russia
Saratov State University, Saratov, Russia
Institute for High-Precision Mechanics and Control Problems,
Russian Academy of Sciences, Saratov, Russia
Received March 1, 2004

Abstract—A method of reconstruction of the object image from a recorded speckle pattern of the scattered coherent radiation field has been developed and experimentally verified. In order to restore information about the phase of the diffraction field, which is lost during the recording of the speckle pattern, it is suggested to take the phase difference between adjacent speckles equal to π. The proposed method is applicable to objects for which the average intensity distribution is described by an even function of the coordinates. © *2004 MAIK "Nauka/Interperiodica".*

As is known, complete information about the light field scattered by an object can be recorded and read with the aid of a holographic technique using a coherent reference wave. In the absence of such a wave, we measure a speckle pattern of the scattered intensity distribution [1]. The development of methods for the reconstruction of object images from such patterns is of interest for diffraction optics, various optical measurements, optical diagnostics, optical data processing, etc. For this reason, the possibilities of solving this problem, which is incorrectly posed from mathematical standpoint [2], have been rather extensively studied (see, e.g., [2–4]).

Formally speaking, the problem consists in that, when a speckle pattern is recorded, the information about the phase of the object field in the registration plane is lost. It is this point that places the problem of image reconstruction under such conditions in the class of ill-posed problems [5]. In optics, this situation is referred to as the phase problem [6–10]. Once a method of restoring spatial field phase distributions in the plane of the speckle pattern, together with the field amplitude, becomes available, the object image could be reconstructed from the recorded diffraction field.

This paper describes a method of restoring the spatial distribution of the phase of a speckle field formed during the scattering of a laser field from an object, for which the average intensity distribution is described by an even function of the coordinates. In this case, the object field in the far diffraction zone is described (as was demonstrated, for the most part theoretically, in [11, 12]) by a real function of the coordinates. In other words, the cross section of a coherent field scattered by such an object represents a combination of speckles such that the phase is constant or continuously varies in a certain way inside each speckle and changes by π on the passage to the adjacent speckle. This circumstance allows the phase information about the phase wave to be restored without using a reference beam in the stage of recording of the object field intensity distribution. This study was aimed at the experimental verification of the possibility of using these theoretical concepts for reconstruction of an object image from the speckle pattern of a scattered coherent field.

There are several possible approaches to solving the problem formulated above. One possibility is offered by an experimental procedure performed using the scheme depicted in Fig. 1. According to this, laser beam *1* illuminates a scattering object *2* and a binary transparency *3*, this combination representing the object whose image is recorded. Radiation scattered from this object is recorded by a photosensitive medium *5* in the far diffraction zone. In our experiments, transparency *3* had the form of a nontransparent screen with a square ring hole *4*. Figure 1 also shows an increased fragment of the speckle pattern formed on the registration plane in the far diffraction zone *6*.
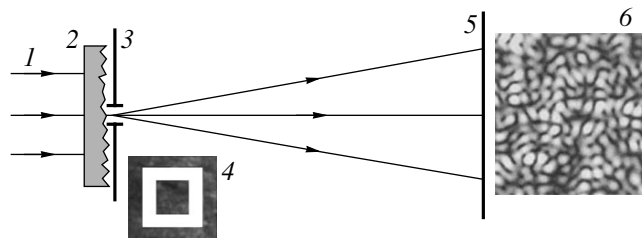

Fig. 1. Schematic diagram of the speckle pattern recording: (*1*) laser beam; (*2*) scattering object; (*3, 4*) transparency; (*5*) photosensitive medium; (*6*) magnified fragment of a spackle pattern formed in the far diffraction zone.
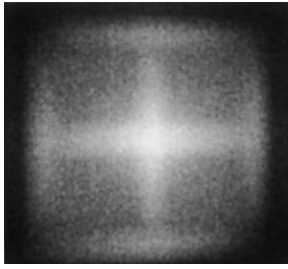
Fig. 2. Laser beam diffraction on a speckle pattern, observed in the far diffraction zone.

Illuminated by a monochromatic wave, the speckle pattern (formed, e.g., on a high-resolution photographic plate) forms an average intensity distribution pattern in the far diffraction field. This distribution is determined by self-convolution of the distribution of average illumination over the object [13]. Figure 2 shows the experimental intensity distribution corresponding to speckle pattern obtained according to the scheme in Fig. 1. As expected, this pattern bears only a faint resemblance to the initial intensity distribution.

Let us return to the speckle pattern observed in the registration plane (Fig. 1). In accordance with the approach outlined above, it is necessary to assign a certain phase to each speckle in this pattern, thus obtaining the amplitude and phase distribution of the object field in the registration plane. In holography, this procedure is performed using a coherent reference beam and a system of interference carrier bands inside the speckles. Indeed, if a plane reference wave is incident at a certain angle θ onto plane *4* (Fig. 1) in the recording stage, then a system of equidistant quasi-parallel interference bands with a period of $\Lambda = \lambda/\sin\theta$ is formed within each speckle. Since we assume that the phases of adjacent speckles are shifted by π [11, 12], the interference bands in the speckles will shift by a half-period on the passage between neighboring speckles. Figure 3a

shows a fragment of such a speckle-modulated interference pattern essentially representing a hologram.

An analogous pattern can be obtained artificially by using a record of only one speckle pattern without a reference beam. For this purpose, a given speckle pattern has to be covered (e.g., using computer graphics) by a system of bands simulating the interference bands on a real hologram. A fragment of a pattern obtained in this way is shown in Fig. 3b. This pattern simulates a hologram, and a period of quasi-regular interference carrier bands determines the slope of a plane virtual reference wave relative to the registration plane of the speckle pattern. Reconstruction of the object field and, hence, the object image consists in transfer of the obtained pattern to a photographic plate (in a scale convenient for use as a diffraction element) and illumination of this element by a plane monochromatic wave. A half-period shift of bands in the diffraction element leads to a shift by π between neighboring speckles. On the whole, the complete diffracted light field represents a coherent superposition of elementary light fields formed as a result of diffraction on the periodic system of bands within separate speckles of the diffraction element (in the same manner as in the usual hologram). Thus, the object light wave is reconstructed and the object image is formed in the far diffraction zone.

In our experiments, the speckle pattern formed according to the scheme of Fig. 1 was recorded using a Nikon D'100 digital camera without an objective lens equipped with a CCD matrix (23.7 × 15.6 mm; 3008 × 2000 = 6.1 × 10⁶ pixels). An image of the speckle pattern was stored in a graphical file and processed using the CorelDRAW program package so as to form a system of parallel bands shifted by a half-period in the neighboring speckles (Fig. 3b). The obtained pattern was transferred to a photographic plate, which represented a holographically similar diffraction element.

Figure 4a shows a pattern of the far diffraction zone formed upon illumination of the obtained diffraction element by a laser beam ($D \approx 6$ mm). The central part
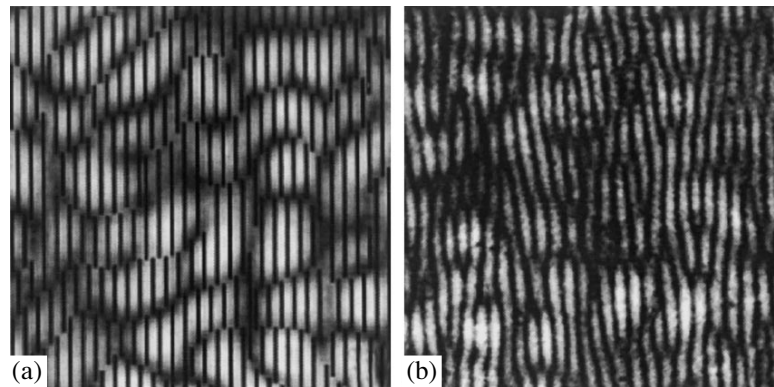

Fig. 3. Fragments of (a) a real hologram of the scatterer and (b) a speckle pattern of the same object with an artificial system of carrier bands.
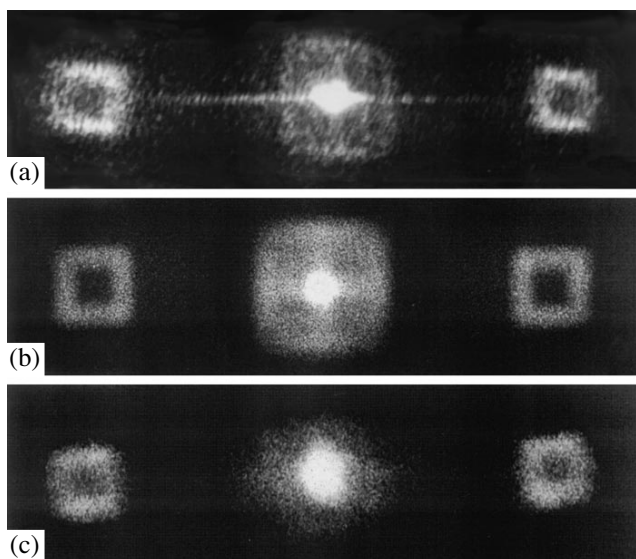
Fig. 4. Patterns formed in the far diffraction zone when a laser beam illuminates (a) a diffraction element, (b) a real hologram, and (c) an optical diffraction element containing only a system of carrier bands.

of this pattern shows, in the zero order of diffraction, a distribution of intensity analogous to that presented in Fig. 2 (the wave propagating in this direction is diffracted only on the speckle pattern of the optical diffraction element). In the ±1 orders of diffraction, the system of carrier bands forms optically conjugated images of the object in the form of a square ring (Fig. 1). For comparison, Fig. 4b shows the pattern of a diffraction field of a real hologram of the same object recorded using the scheme of Fig. 1 with a reference wave (a laser beam of the same diameter as that used for the reconstruction of the image from the diffraction element).

We have also obtained an optical diffraction element containing only the system of carrier bands without the original speckle pattern. In other words, the original pattern was removed after the creation of a system of bands on the recorded speckle pattern and the remaining system was transferred to a photographic plate. The resulting diffraction element contains a manifold of elementary diffraction gratings with the dimensions and spatial arrangement determined by those of the speckles in the original pattern. Using this diffraction element, it is also possible to reconstruct the object image (Fig. 4c). However, in this case, the zero order of diffraction exhibits no diffraction halo determined by the autocorrelated intensity distribution over the object.

The relatively low quality of the object image reconstructed using the simulated hologram is explained by the fact that the holographic processing of a speckle pattern without using a special program is a rather labo-

rious procedure. The number of processed speckles did not exceed several thousand, which is insufficient in such cases. Nevertheless, quite clear images of square rings are obtained in the ±1 orders of diffraction.

In conclusion, we showed the principal possibility of reconstructing the image of an object using a speckle pattern of its diffraction field and demonstrated a possible procedure based on the creation of an optical diffraction element with a system of carrier bands. An analogous procedure, starting with the moment of speckle pattern recording, can be performed using only computational methods without forming real diffraction elements, whereby the image is obtained on a computer display.

REFERENCES

1. M. Francon, *Laser Speckle and Applications in Optics* (Academic, New York, 1979).
2. I. M. Bel'dyugin, I. G. Zubarev, and S. I. Mikhaĭlov, Kvantovaya Élektron. (Moscow) **31**, 539 (2001).
3. J. R. Fienap, Appl. Opt. **21**, 2758 (1982).
4. R. H. T. Bates and D. G. H. Tan, J. Opt. Soc. Am. A **2**, 2013 (1985).
5. *Inverse Source Problems in Optics*, Ed. by H. P. Baltes (Springer-Verlag, Berlin, 1978).
6. M. V. Vakhrusheva and N. G. Vlasov, Prikl. Mekh. Tekh. Fiz. **2** (4), 3 (2003).
7. N. G. Vlasov, A. V. Sazhin, and S. G. Kalenkov, Laser Phys. **6**, 401 (1996).
8. A. V. Goncharskiĭ, V. V. Popov, and V. V. Stepanov, *Introduction to Computer Optics* (Izd. Mosk. Gos. Univ., Moscow, 1991) [in Russian].
9. *The Computer in Optical Research*, Ed. by B. R. Frieden (Springer-Verlag, Berlin, 1980; Mir, Moscow, 1983).
10. V. P. Aksenov, V. A. Banakh, and O. V. Tikhomirova, Opt. Atmos. Okeana **9**, 1450 (1996).
11. B. B. Gorbatenko, I. S. Klimenko, L. A. Maksimova, and V. P. Ryabukho, Opt. Spektrosk. **78**, 316 (1995) [Opt. Spectrosc. **78**, 283 (1995)].
12. B. B. Gorbatenko, I. S. Klimenko, L. A. Maksimova, and V. P. Ryabukho, Pis'ma Zh. Tekh. Fiz. **18** (2), 26 (1992) [Sov. Tech. Phys. Lett. **18**, 35 (1992)].
13. R. J. Collier, C. B. Burckhardt, and L. H. Lin, *Optical Holography* (Academic Press, New York, 1971; Mir, Moscow, 1973).

Translated by P. Pozdeev

Phase Inhomogeneity of Pyroboroncarbon Structure

V. N. Kukin[a,*], N. I. Borgardt[a], A. V. Agafonov[b], and V. O. Kuznetsov[b]

[a] Moscow State Institute of Electronic Technology (Technical University), Moscow, Russia
[b] TRI Carbon Ltd., Moscow, Russia
* e-mail: kukin@lemi.miee.ru
Received March 16, 2004

Abstract—Peculiarities of the structure and phase composition of pyroboroncarbon were studied by a combination of electron-microscopic techniques including electron diffraction, high-energy electron loss spectroscopy, bright- and dark-field imaging with diffraction contrast, and high-resolution measurements up to the atomic resolution level. © *2004 MAIK "Nauka/Interperiodica".*

Pyroboroncarbon (PBC) is an isotropic pyrolytic material synthesized by thermal decomposition of a mixture of carbon-containing gases (methane and propane) with boron chloride [1]. With respect to the structure, mechanical properties, and method of synthesis, this material is very close to pyrocarbon. Successful practical applications of PBC include medicinal prosthetic devices, in particular, heart valves [2, 3]. In contrast to pyrocarbon, whose properties were extensively studied and reported in a large number of publications (see, e.g., review [4] and references therein), the structure and the mechanism of PBC formation are studied to a lower extent. To our knowledge, no data on the PBC structure on the atomic level have been reported so far.

In order to fill this gap, we have studied PBC by a combination of electron-microscopic techniques and obtained detailed data on the structure of this material with a resolution of up to the atomic level.

We have studied samples of PBC grade intended for manufacturing prosthetic heart valves. The synthesis was conducted for 5–12 h in an axisymmetric reactor at a pressure of 800–1300 Pa and a temperature of 1450–1490°C. Thermodestruction of a mixture of carbon-containing gases and boron chloride under these conditions was accompanied by the formation of 4- to 5-mm-thick PBC layers on a carbon substrate. The gas phase also contained an additive of nitrogen. Electron-microscopic investigation of the PBC samples were performed on a Philips CM-30 electron microscope operating at an accelerating voltage of up to 300 kV.

The electron diffraction measurements showed that PBC comprises a mixture of phases of two types. The first type, accounting for most of the material, is characterized by a turbostratic structure typical of pyrocarbon [4]. This structure is manifested on the electron diffraction patterns by high-intensity bright arcs and two less intense diffraction rings (Fig. 1, right insets). The bright arcs corresponded to the reflections from basal graphite planes (formed by carbon hexagons), representing 002, 004, etc., lattice fringes, while the diffraction rings corresponded to the reflections from the (100) and (110) planes. The high-energy electron loss spectra obtained from regions of the first phase displayed a single clearly pronounced peak of carbon (K edge, 284 eV). The values of interplanar spacing, $C_{(002)} = 0.343$ nm, $C_{(100)} = 0.213$ nm, and $C_{(110)} = 0.123$ nm, coincided with the values known for pyrocarbon [2, 5, 6].

By studying the electron-microscopic images on the first phase, we established the laws of variation of the orientation of crystals forming this turbostratic structure. Using dark-field micrographs obtained in the reflections corresponding to bright arcs (lattice fringes), it was found that, within domains with dimensions about 1–2 μm, the basal planes of crystallites were predominantly aligned in a certain direction, so
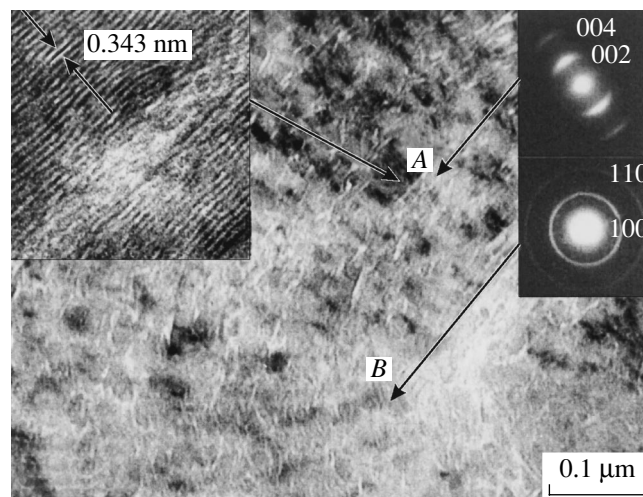

Fig. 1. Defocused bright-field electron-microscopic image of a PBC sample region corresponding to the first phase. The right inset shows the electron diffraction patterns obtained from regions *A* and *B*. The left inset shows a high-resolution micrograph of region *A*.

that these domains were textured. In the neighboring domains, the basal planes had different predominant orientations such that the whole PBC structure was isotropic.

Inside the textured domains, there were local regions in which the orientation of basal planes deviated from the predominant orientation. In order to reveal such regions, we used defocused images with diffraction contrast and high-resolution micrographs measured for the sample oriented so that predominant orientation of the basal planes would coincide with the primary electron beam direction. An important role in the formation of defocused images is played by differences in both amplitudes and phases of the electron waves. These images provide visualization of the contrast features absent in the case of exact focusing of the object lens. These features appeared as parallel segments (narrow bands) representing contours of the Fresnel lines, arising due to the sample regions (Fig. 1, region *A*) in which the orientation of basal planes deviated from the predominant direction. These deviations led to local changes in the scattering ability and variations in the distribution of phases of the output electron waves, eventually manifested by the contrast of defocused images. This conclusion concerning local variations in the orientations of crystallites was confirmed by the analysis of high-resolution micrographs obtained for the sample regions in which the Fresnel lines were observed. As can be seen from the left inset in Fig. 1, the images of basal planes oriented along the electron beam appear as virtually parallel rows in the top left and bottom right parts of this micrograph. The central part of this high-resolution micrograph appears as a wide bright band where the direct resolution contrast of basal planes is absent, which is evidence of a change in their orientation. The direction of the bright band coincides with that of the corresponding Fresnel line on the defocused bright-field micrographs, while the width of this band is correlated with the Fresnel line size.

The data of electron diffraction, in combination with the bright- and dark-field images, obtained for the sample regions corresponding to the second phase (Fig. 2) showed evidence of the presence of single-crystalline inclusions. The particles of this phase could be divided into two groups with respect to their dimensions. The larger (Fig. 2, particle *a*) inclusions representing 0.1–0.25 μm crystallites gave selected-area electron diffraction patterns with point reflections (Fig. 2, right inset). No such patterns could be obtained from particles of the second group, which have small sizes within 5–20 nm. The corresponding reflections were present on the ring diffraction patterns obtained from relatively large regions of the sample, which contained integral information about all phases of the sample (Fig. 2, top left inset). These small particles (Fig. 2, particles *b* in the bottom left inset) were visualized in the dark-field images. The high-energy electron loss spectra obtained from the regions with large particles of the second
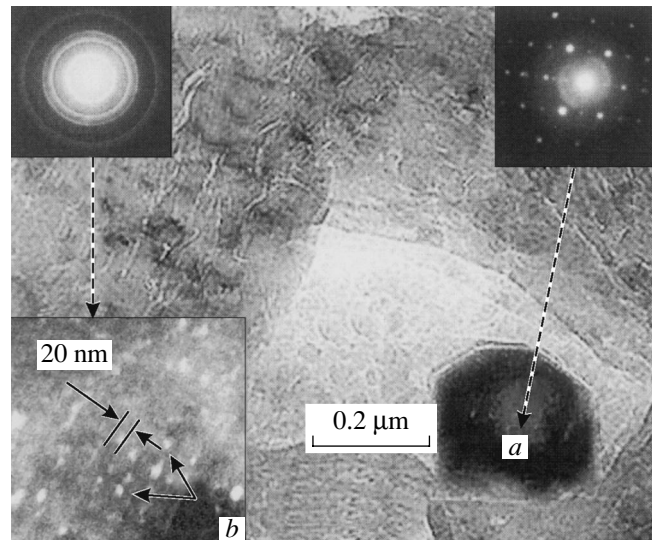

Fig. 2. Defocused bright-field electron-microscopic image of a PBC sample showing large (*a*) and small (*b*) inclusions of the second phase. The left bottom inset shows a dark-field image obtained in one of the reflections of the electron diffraction pattern shown in the top left inset. The top right inset shows an electron diffraction pattern corresponding to particle (*a*). Regions *A* and *B* correspond to domains of the first phase with different predominant orientations of the crystallites possessing a turbostratic structure.

phase displayed a peak of boron (*K* edge, 188 eV), while the peak of carbon was absent. High-resolution micrographs obtained from both large and small particles of the second phase were indicative of their high crystal perfection. These crystallites exhibited a macroscopically uniform distribution over the PBC sample volume. Large particles occurred at the boundaries of textured domains of the first phase, while more numerous small particles occurred inside these domains.

The interplanar distances for the PBC phases, determined from the electron diffraction data are presented in the table. For the small single-crystalline inclusions, the values corresponded to the structures of various modifications of boron carbide [7, 8]. In the case of large inclusions, we took into account both the interplanar spacings and the angles between crystallographic directions (determined from a series of electron diffraction patterns measured for various projection planes). These data corresponded to a cubic structure with a lattice parameter of about 0.362 nm. Although this value corresponds to the cubic modification of boron nitride [9–11], the final assignment of large inclusions to this phase requires additional investigations.

Thus, the results of our electron-microscopic investigation showed that PBC is a composite material comprising the layers of pyrocarbon and large and small single-crystalline inclusions distributed in and between these layers. Small inclusions represent a modification of boron carbide, while large inclusions probably correspond to a cubic phase of boron nitride.

Interplanar distances in pyroboroncarbon determined in these experiments in comparison to published data for some carbon materials

Experimental values, nm	Turbostratic graphite, nm [2, 5, 6]	h-B$_4$C, nm [7]	h-B$_{13}$C$_2$, nm [8]		c-BN, nm [9–11]
0.451 ± 0.002			0.450		
0.401 ± 0.002		0.400	0.403		
0.378 ± 0.002		0.379	0.377		
0.362 ± 0.002					0.362
0.343 ± 0.002	0.344	0.339			
0.255 ± 0.002		0.257	0.2569	0.280	0.256
0.238 ± 0.002		0.238	0.2385		
0.232 ± 0.002			0.2305		
0.213 ± 0.002	0.213				
0.205 ± 0.002		0.203			0.209
0.181 ± 0.002		0.181	0.1816		0.181
0.172 ± 0.002			0.1712		
0.166 ± 0.002		0.169	0.1628		
0.131 ± 0.002			0.1326	0.1340	
0.126 ± 0.002			0.1264	0.1317	0.128
0.121 ± 0.002	0.123				0.121
0.113 ± 0.002					0.114
0.107 ± 0.002					0.109
0.083 ± 0.002					0.083

The laws of formation of the electron-microscopic images and electron diffraction patterns described above can be used in subsequent investigations aimed at determining the effect of technological parameters on the PBC structure and establishing relationships between the structure and properties of this material.

REFERENCES

1. G. M. Volkov, V. I. Kalugin, and K. I. Syskov, Dokl. Akad. Nauk SSSR **183**, 396 (1968).

2. V. F. Tatarinov and P. I. Zolkin, Ogneupory Tekh. Keram., No. 3, 37 (1999).

3. V. F. Tatarinov, V. S. Virgil'ev, and S. E. Evdokimov, Perspekt. Mater., No. 4, 41 (1999).

4. A. Oberlin, Carbon **40**, 7 (2002).

5. M. Monthioux, B. W. Smith, B. Burteaux, *et al.*, Carbon **39**, 1251 (2001).

6. V. V. Kovalevski, P. R. Buseck, and J. M. Cowley, Carbon **39**, 243 (2001).

7. L. I. Mirkin, *X-ray Structural Analysis. Indexing of Electron Diffraction Patterns* (Nauka, Moscow, 1981) [in Russian].

8. *Powder Diffraction File. Inorganic: Publication SMF-27* (JCPDS-International Center for Diffraction Data, Pennsylvania, 1977).

9. P. B. Mirkarimi, K. F. McCarty, and D. L. Medlin, Mater. Sci. Eng. R **21**, 47 (1997).

10. W. S. Verwoerd, Thin Solid Films **300**, 78 (1997).

11. H. Feldermann, C. Ronning, H. Hofsass, *et al.*, J. Appl. Phys. **90**, 3248 (2001).

Translated by P. Pozdeev

Orientation of Methyl Red Dye Molecules in a Polymer Matrix

A. V. Tomov and A. V. Khomchenko

Institute of Applied Optics, National Academy of Sciences of Belarus, Mogilev, Belarus
e-mail: ipo@physics.belpak.mogilev.by
Received March 23, 2004

Abstract—We have studied the optical anisotropy of waveguide layers formed upon introduction of Methyl Red azo dye molecules into a polycarbonate matrix. The observed anisotropy of absorption in the dyed layers is related to ordering of the azo dye molecules in the course of waveguide layer formation. The order parameter is estimated and the possible mechanism of orientation is proposed. © *2004 MAIK "Nauka/Interperiodica".*

The interest in organic nonlinear optical materials with functional groups having a special direction of orientation is related to the broad spectrum of possible applications of such materials in data transmission and processing systems. There are two main methods used for the orientation of optically active molecules in polymer matrices: poling in a corona discharge (corona poling) [1] and all-optical poling based on the effect of orientation hole burning [2]. Both methods require special equipment and thoroughly selected technological parameters of the poling process. For this reason, the search for new effective methods of obtaining organic optical materials with a selected direction of orientation of the optically active molecules and the study of mechanisms involved in the formation of such media are of considerable importance.

This paper reports on the results of investigation of the phenomena of alignment accompanying the formation of thin (5–30 μm) waveguide layers by means of solvent-assisted diffusion of Methyl Red azo dye from solution into polycarbonate substrates based on 1,1-di(4-oxyphenyl)propane. The refractive index profile in these layers was reconstructed using the measured mode spectrum. For the TE wave of probing radiation (with the electric vector parallel to the waveguide layer), this procedure was based on the inverse WKB technique [3], while for the TM wave (with the electric vector virtually perpendicular to the waveguide layer), we used the method proposed in [4]. The complex propagation constants of the modes excited in the waveguide structures were determined by measuring the angular distribution of the laser beam reflection coefficient ($\lambda = 0.633$ μm) with the aid of a prism coupling device [5].

A characteristic feature of the structures under consideration is considerable anisotropy of the refractive index. With respect to the TE wave, these layers exhibit the properties of usual waveguides (see curve *1* in the figure), whereby the index at any point of the cross section is greater than in the substrate ($n_{TE} = 1.5804$). For the TM-polarized probing radiation, the sample structures guide only leaky modes. An analysis of the index profiles in the samples obtained under various conditions showed that the maximum value of n in this case is close to that in the substrate ($n_{TM} = 1.5780$), but there is a region of reduced index between a subsurface layer and the substrate (curve *2* in the figure).

The results of X-ray diffraction and IR spectroscopy measurements suggested that the observed anisotropy is caused to a considerable extent by the predominant orientation of polymer molecules in the plane of the film [6]. In order to estimate the contribution of the
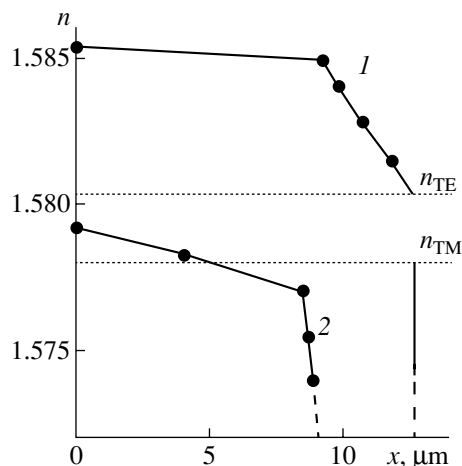
Characteristic profiles of the refractive index n for the (*1*) TE and (*2*) TM waves of the probing radiation in waveguide layers obtained by solvent-assisted diffusion of Methyl Red into polycarbonate.

Calculated parameters of the waveguide layers formed in a polymer treated in a dye solution (series 1) and in pure solvent (series 2)

Sample	Probing wave	Model parameters	Diffusion time		
			1 min	2 min	4 min
Series 1	TE	n	1.5866	1.5864	1.5863
		d, μm	4.81	6.37	9.40
	TM	n	1.5788	1.5786	1.5787
		d, μm	4.51	5.99	9.74
Series 2		n	1.5739	1.5746	1.5744
		d, μm	4.26	5.88	10.16

polymer orientation to the ordering of waveguide layers in the course of their formation, we studied the samples prepared using the azo dye solution (series 1) and the pure solvent (series 2) under otherwise equal conditions. A comparison of the spectra of the TE and TM modes showed that waveguide structures formed in both cases are of the same type, but the change in the refractive index in the latter case is smaller than in the former. In order to characterize the samples, their structures were modeled by thin homogeneous films with refractive index n and thickness d. These parameters were calculated from experimental data using the methods described in [3, 7]. The results of calculations are presented in the table.

An analysis of the results of model calculations shows that the formation of waveguide layers under consideration involves at least two different processes: (i) an increase in the refractive index caused by the introduction of azo dye molecules into the polymer matrix and (ii) a change in the matrix index under the action of solvent, which is positive for the TE probing wave and negative for the TM wave. The second process can be explained by an increase in the mobility of macromolecules in the solid polymer in the presence of solvent. As a result, a certain fraction of these molecules is reoriented to become parallel to the sample surface, which increases the degree of ordering in a subsurface layer of the polymer matrix [6]. This change in the spatial arrangement of macromolecules results in that the refractive index increases for the TE wave and decreases for the TM wave. Taking into account the positive contribution to the index due to the azo dye, we obtain the index profile $n_{TM}(x)$ for the TM wave as depicted in the figure (curve 2).

As was mentioned above, such a waveguide features leaky modes. The values of the imaginary part h'' of the propagation constants calculated for these modes using a stepwise model profile $n_{TM}(x)$ proved to be much smaller than the experimental values. For example, the values of $h'' k_0^{-1}$ (k_0 is the wave number in vacuum) measured for the first two modes of a waveguide layer formed in the azo dye solution with a concentration of $C = 0.02$ M at room temperature for 8 min were $h_0'' k_0^{-1} = 6.0 \times 10^{-4}$ and $h_1'' k_0^{-1} = 1.9 \times 10^{-3}$. These values are at least ten times greater than the results of calculation: $h_{c0}'' k_0^{-1} = 2.4 \times 10^{-5}$ and $h_{c1}'' k_0^{-1} = 9.9 \times 10^{-5}$. Taking into account small scattering losses, it is natural to suggest that this increase in the optical losses is due to the absorption in the waveguide. The absorption can be related only to the presence of the azo dye, since polycarbonate is transparent in the visible spectral range. At the same time, it is known [8] that Methyl Red may partly occur in a *cis* form absorbing light in the wavelength interval 0.55–0.65 μm. The method used for the measurement of the propagation constant allowed the real and imaginary parts of h to be determined for both guided and leaky modes, so that the absorption coefficient k of the waveguide material could also be determined in both cases. For the example under consideration, we obtained $k_{TE} = 2.0 \times 10^{-4}$ and $k_{TM} = 4.2 \times 10^{-4}$. Therefore, the obtained layers exhibit anisotropic absorption, which is apparently related to a certain orientation of the azo dye molecules rather than to the waveguide properties of dyed layers. The degree of this orientation can be evaluated in terms of the order parameter defined as $F = (k_{TM} - k_{TE})/(k_{TM} + 2k_{TE})$ [1]. For the given sample, this parameter was $F = 0.26$, which is comparable with the degree of orientation achieved using conventional methods [1, 2].

The data presented above indicate that inhomogeneous layers obtained upon diffusion of Methyl Red into a polycarbonate substrate are characterized by the orientation of molecules of both the polymer matrix and the azo dye. This alignment is probably explained by a chemical interaction of the azo dye with the polymer via hydrogen bonds formed between the OH groups of Methyl Red and C=O groups of the polymer matrix, which was previously observed in solution [9]. Some evidence is provided by a comparison of the IR spectra of the pure polycarbonate and that doped with Methyl Red, which showed a shift by $\Delta v \approx 2$ cm^{-1} of the maximum of the absorption band belonging to C=O groups of the polymer. This shift can be interpreted as being indicative of the chemical interaction between these groups and the azo dye.

Naturally, all assumptions concerning the mechanisms responsible for the anisotropic absorption observed in the waveguide layers studied have to be verified by additional investigations.

REFERENCES

1. R. H. Page, M. C. Jurich, R. Reck, *et al.*, J. Opt. Soc. Am. B **7**, 1239 (1990).

2. J.-M. Nunzi, C. Fiorini, A.-C. Etile, *et al.*, Pure Appl. Opt. **7**, 141 (1998).

3. *Integrated Optics*, Ed. by T. Tamir (Springer-Verlag, Berlin, 1975; Mir, Moscow, 1978).

4. I. U. Primak and A. V. Tomov, Vestsi Nats. Akad. Navuk Belarusi, Ser. Fiz.-Mat. Navuk, No. 2, 97 (2001).

5. A. V. Khomchenko, A. B. Sotskiĭ, A. A. Romanenko, *et al.*, Pis'ma Zh. Tekh. Fiz. **28** (11), 51 (2002) [Tech. Phys. Lett. **28**, 467 (2002)].

6. A. V. Tomov, in *Proceedings of the International Scientific–Engineering Conference "Polymer Composites," Gomel, 2000*, pp. 166–168.

7. T.-N. Ding and E. Garmire, Appl. Opt. **22**, 3177 (1983).

8. A. V. Tomov, A. I. Voĭtenkov, and A. V. Khomchenko, Zh. Tekh. Fiz. **68** (2), 124 (1998) [Tech. Phys. **43**, 249 (1998)].

9. J. A. Lee and T. P. Lodge, J. Phys. Chem. **91**, 5546 (1987).

Translated by P. Pozdeev

Optical Rectification Effect in Nanocarbon Films

G. M. Mikheev*, R. G. Zonov, A. N. Obraztsov, and Yu. P. Svirko

Institute of Applied Mechanics, Ural Division, Russian Academy of Sciences, Izhevsk, Udmurtia, Russia
Department of Physics, Moscow State University, Moscow, Russia
Faculty of Physics, Joensuu University, Joensuu, Finland
* e-mail: gmmikheev@udmnet.ru
Received March 23, 2004

Abstract—When a nanocarbon film obtained by plasmachemical deposition is fixed between two parallel electrodes and exposed to the pulsed radiation of a Q-switched neodymium laser, a pulsed electric voltage appears between the electrodes, with the pulse shape repeating the laser pulse envelope. It is shown that the amplitude and polarity of the pulsed voltage strongly depend on the angle of incidence and polarization of laser beam and on the spatial orientation of a carbon film with electrodes relative to the laser beam. The observed phenomenon exhibits all features characteristic of the optical rectification effect. For the optimum spatial orientation of a film, the factor of conversion of the laser pulse power into electric voltage amounted to 500 mV/MW, which is many times greater than the values observed in the case of optical rectification in well-known dielectric nonlinear optical crystals. © 2004 MAIK "Nauka/Interperiodica".

The phenomenon of optical rectification consists in that a sufficiently powerful laser pulse passing through a nonlinear optical crystal induces a dielectric polarization signal in this medium, whose shape repeats the laser pulse envelope [1, 2]. If such a nonlinear optical crystal is placed between electrodes, the laser-induced polarization will lead to the appearance of a voltage between these electrodes. In transparent media, the optical rectification effect is related to the second term in the expansion of the polarization vector into series with respect to the electric field strength (that is, to the second-order nonlinear permittivity). For this reason, observation of the optical rectification effect in the dipole approximation is possible only in nonlinear optical crystals possessing no center of inversion. Recently, Margulis *et al.* [3] theoretically studied the optical rectification effect in carbon nanotubes, which is possible because of the central symmetry breakage in a constant electric field. As is known, optical rectification was observed in a rather large number of noncentrosymmetric crystals (see, e.g., review [2]). To the best of our knowledge, no data have been reported on the investigation and observation of the optical rectification effect in thin-film graphite structures. It should be noted that the study of optical rectification is of interest from the standpoint of application of this effect to the measurement of the power, polarization, and shape of laser pulses in a broad range of electromagnetic radiation wavelengths and the generation of ultrashort electromagnetic pulses in the frequency range 0.1–50 THz [4].

This paper reports on the experimental observation of the optical rectification effect in nanocarbon films.

The experiments were performed with carbon films obtained by plasmachemical deposition from a methane–hydrogen mixture according to our standard method described elsewhere [5, 6]. The films were deposited onto 25 × 25-mm silicon substrates. The main structural elements in these carbon films are crystallites of an irregular shape comprising several (typically, five to fifty) parallel, well-ordered graphite layers. The thickness of these crystallites ranges from 2 to 20 nm, while the lateral dimensions vary within 1−3 µm. In all crystallites, the atomic layers exhibit predominant orientation in the direction normal to the substrate surface, with a maximum deviation not exceeding ±20°. The distance between crystallites is about 0.5–1 µm. Thus, the carbon films studied exhibit a clearly pronounced porous nanocrystalline structure. The average thickness of nanocarbon films was 3–4 µm.

Figure 1 shows a schematic diagram of the experimental arrangement. A nanocarbon film 6 on a silicon substrate 8 was pressed with two flat conducting elec-
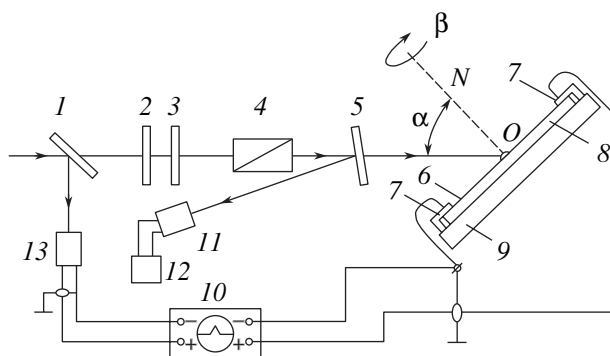

Fig. 1. Schematic diagram of the experimental arrangement (see the text for explanations).

trodes *7* to a dielectric sample holder *9*. The amplitude of the voltage *U* appearing between the electrodes during laser irradiation of the graphite film was measured using a storage oscillograph *10* with an input impedance of 1 MΩ, while the shape of electric pulses was observed using an oscillograph with a pass band of 650 MHz. The radiation source was a single-mode single-frequency YAG:Nd^{3+} laser [7] generating pulses of Gauss shape with a full width at half maximum (FWHM) of about 22 ns. The laser beam diameter was 2 mm. The laser beam was attenuated by neutral filters and passed through λ/4 plates (*2*, *3*) and a polarizer *4*. The quarter-wave plates changed the orientation of the polarization planes in the beam entering the polarizer, which allowed the power of linearly polarized radiation at the polarizer output to be smoothly controlled. The polarizer could be rotated up to 90° around its axis, which allowed *p*- and *s*-polarized beams to be obtained. Using divider plate *5* together with photodiode *11* and an automated multichannel registration system *12* [8], it was possible to measure the energy of pulsed radiation incident onto the sample film. Plate *1*, together with an avalanche photodiode *13* enabled the observation of laser radiation pulses on an oscillograph screen. Measurements according to this scheme were also performed using second harmonic radiation of the same laser. All the results presented below were obtained for laser pulse energies below a threshold for the visible laser damage of the graphite films studied [9].

The results of our experiments showed that irradiation of a nanocarbon film by laser pulses at λ = 1064 nm is accompanied by the appearance of pulsed voltage between the electrodes. The shape of this signal was virtually identical to the laser pulse shape observed with the aid of the avalanche photodiode. Analogous results were obtained for the samples irradiated by second-harmonic radiation (λ = 532 nm) with a pulse width of 16 ns.

Further investigation showed that the amplitude *U* and polarity of the pulsed voltage strongly depend on the polarization of laser beam and on the spatial orientation of a carbon film with electrodes relative to the laser beam. When the laser beam was perpendicular to the film plane, the response signal amplitude was zero irrespective of the beam polarization and the arrangement of electrodes.

Figure 2a shows the dependence of the response voltage pulse amplitude *U* on the angle α of laser beam incidence relative to the film plane (Fig. 1) for the *p*- and *s*-polarized radiation. Note that, according to Fig. 1, α = 0 when the film surface is perpendicular to the laser beam; α is positive (negative) when the film is rotated clockwise (counterclockwise) from the initial position. The axis of rotation passing through the point *O*, the plane of the film, and the electrodes are perpendicular to the plane of the figure, which coincides with the plane of laser beam incidence. It should also be noted that data corresponding to the incidence
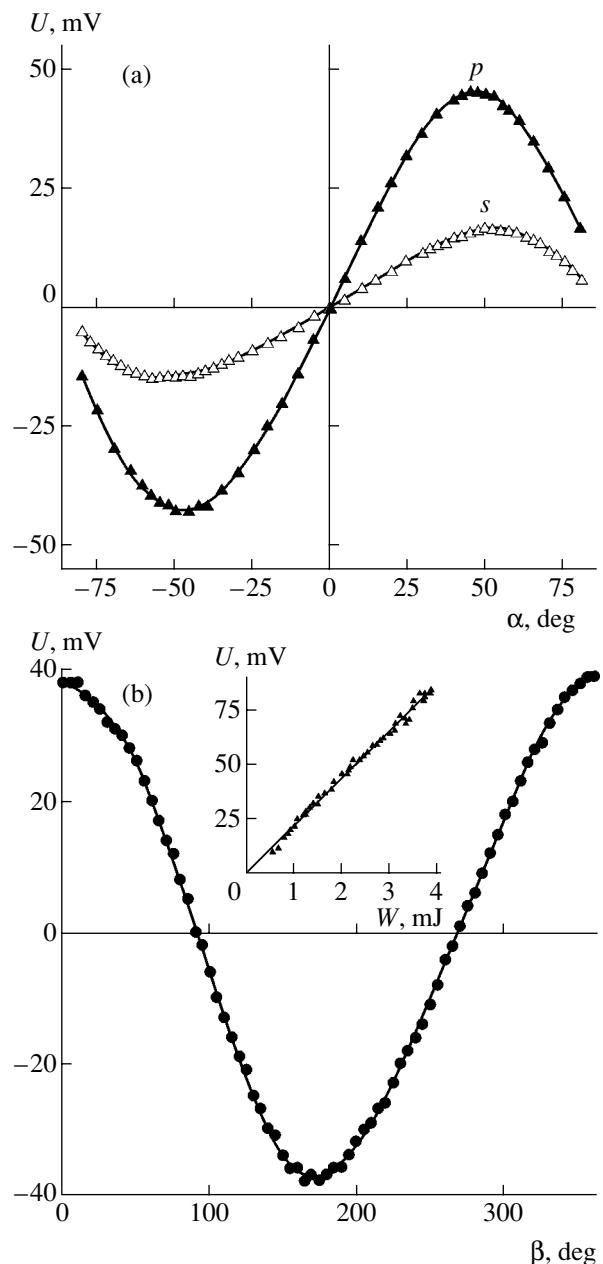

Fig. 2. Plots of the amplitude of a pulsed response voltage between electrodes fixed on the nanocarbon film versus (a) the angle α of incidence of *p*- and *s*-polarized laser radiation (τ = 22 ns, λ = 1064 nm, *W* = 2 mJ) and (b) the angle β of rotation of the film with electrodes for *p*-polarized radiation (α = 50°, *W* = 1.7 mJ). The inset shows the plot of *U* versus laser pulse energy *W* for α = 50° and β = 0°.

angles close to ±90° are not presented in Fig. 2a because laser radiation incident at grazing angles on the sample surface partly illuminated the electrodes, which resulted in that the response voltage pulse duration became significantly longer than the laser pulse width. As can be seen from Fig. 2a, the experimental curves behave as uneven functions. In addition, it is seen that the absolute value *U* is maximum at α = ±(45–55)° and that the *U*(α) curves for the *p*- and *s*-polarized laser

radiation are significantly different. At fixed laser beam energy, the response voltage pulse amplitude for the *p* polarization exceeds that for the *s* polarization in the entire range of α.

Figure 2b shows the plot of *U* versus β, the angle of rotation of a sample film *6* with electrodes *7* relative to the *ON* axis (Fig. 1) coinciding with the normal to the surface, measured for the *p*-polarized laser beam and a fixed incidence angle α = +50°. It should be noted that the values β = 0° and 180° correspond to the positions of electrodes *7* perpendicular to the plane of laser beam incidence (plane of Fig. 1). As can be seen from Fig. 2b, rotation of the sample holder plate with electrodes around the *ON* axis leads to variation of the response voltage pulse amplitude according to the cosine law. When electrodes *7* are in the planes parallel to the plane of laser beam incidence (β = 90° and 270°) the response voltage pulse amplitude is zero. For β = 180°, when the electrodes change their mutual arrangement (upper electrode becomes lower and vice versa, see Fig. 1), the response signal becomes negative, while its amplitude approximately corresponds to that observed for β = 0°.

The results of our measurements performed for various fixed values of α and β showed that, to a good approximation, the plots of *U* versus the laser pulse energy *W* are linear (see the inset in Fig. 2b). For α = 50° and β = 0°, the factor of conversion $\eta_{\lambda = 1064 \, nm}$ of the pulsed laser power into response voltage was about 500 mV/MW, while the value of $\eta_{\lambda = 532 \, nm}$ obtained for the second-harmonic radiation was about 650 mV/MW. It should be emphasized that, at a fixed laser pulse power, variation of the laser beam diameter did not lead to a change in the response voltage pulse amplitude measured between the electrodes.

The whole body of experimental results described above covers all features characteristic of the optical rectification effect [2]. However, in contrast to the previously reported investigations, our experiments demonstrated optical rectification on the surface of absorbing electrically conducting nanocarbon films. As is known, the projection of the vector of static polarization, quadratic with respect to the field, onto the *j*th Cartesian axis can be expanded in the general case as follows:

$$P_j(0) \,=\, P_j^D(0) + P_j^{DS}(0) + P_j^Q + P_j^M(0),$$

where the first two terms correspond to polarization in the dipole approximation and describe the volume and surface contributions, while the third and fourth terms reflect the volume quadrupole and magnetic-dipole contributions. For a centrosymmetric medium, the volume dipole term is absent, while the surface dipole and the volume quadrupole contributions to the quadratic polarization can be comparable [10]. It should be noted that, in the case of absorbing centrosymmetric crystals, the contributions to the quadratic polarization due to the volume quadrupole and magnetic-dipole terms can be significant. Indeed, the results of our preliminary theoretical analysis showed that the response voltage pulse amplitude for a quadrupole nonlinearity is proportional to $F(\alpha)\sin 2\alpha \cos \beta$, where $F(\alpha)$ is a slowly varying function. This conclusion is confirmed by the results presented above.

REFERENCES

1. J. F. Ward, Phys. Rev. **143**, 569 (1966).
2. B. N. Morozov and Yu. M. Aĭvazyan, Kvantovaya Élektron. (Moscow) **7**, 5 (1980) [Sov. J. Quantum Electron. **10**, 1 (1980)].
3. V. L. Margulis, E. A. Gaiduk, and E. N. Zhidkin, Opt. Commun. **183**, 317 (2000).
4. M. C. Nuss and J. Orenstein, in *Millimeter and Submillimeter Wave Spectroscopy of Solids* (Springer, Berlin, 1998), pp. 7–50.
5. A. N. Obraztsov, A. P. Volkov, A. I. Boronin, and S. V. Koshcheev, Zh. Éksp. Teor. Fiz. **120**, 970 (2001) [JETP **93**, 846 (2001)].
6. A. N. Obraztsov, A. A. Zolotukhin, A. O. Ustinov, *et al.*, Carbon **41**, 836 (2003).
7. G. M. Mikheev, D. I. Maleev, and T. N. Mogileva, Kvantovaya Élektron. (Moscow) **19**, 45 (1992) [Sov. J. Quantum Electron. **22**, 37 (1992)].
8. G. M. Mikheev, T. N. Mogileva, A. Yu. Popov, and D. G. Kalyuzhnyĭ, Prib. Tekh. Éksp., No. 2, 101 (2003) [Instrum. Exp. Tech. **46**, 233 (2003)].
9. G. M. Mikheev, R. G. Zonov, A. N. Obraztsov, and A. P. Volkov, Zh. Éksp. Teor. Fiz. **125**, 548 (2004) [JETP **98**, 483 (2004)].
10. S. A. Akhmanov, V. I. Emel'yanov, N. I. Koroteev, and V. N. Seminogov, Usp. Fiz. Nauk **147**, 675 (1985) [Sov. Phys. Usp. **28**, 1084 (1985)].

Translated by P. Pozdeev

Electron Emission from Solid Surfaces Stimulated by Electric Field and Heterogeneous Chemical Reaction

V. F. Kharlamov*, A. V. Sedov, and S. N. Romashin

Orel State Technical University, Orel, Russia
* e-mail: kharl@ostu.ru
Received March 24, 2004

Abstract—A method for monitoring the process of electron accommodation during chemical reactions at the gas–solid (metal, semiconductor) interface is proposed. It is established that the tunneling electron current from a solid surface (Ni, Cu, Si steel) increases by a factor of 10^3–10^5 when a heterogeneous chemical reaction (H + H $\longrightarrow$ H$_2$) proceeds on the surface. Autooscillations of the reaction-stimulated tunneling current have been observed. A method of investigation of the structure of surface catalytic centers on a nanometer resolution level is proposed. © 2004 MAIK "Nauka/Interperiodica".

When heterogeneous chemical reactions proceed at the solid–gas interface, molecules of the intermediate and target products formed in the course of these reactions are stabilized due to the energy exchange between reacting species and the surface. This energy exchange involves both the crystal lattice (phonons) and the electron subsystem of the solid. The electron excitation of semiconductors in the course of heterogeneous chemical reactions on their surfaces is accompanied by luminescence [1], nonequilibrium conductivity [2], and electron emission [3]. In the case of metal substrates, methods for monitoring the generation of excited electrons during surface chemical reactions have not been developed. In particular, electron chemoemission from metal surfaces is observed quite rarely under certain special conditions (small work function of the surface, etc.) [3–6].

This paper demonstrates that the process of electron accommodation during chemical reactions on solid surfaces can be monitored using the phenomenon of electron tunneling, whereby excited electrons penetrate from a solid (acting as a reaction catalyst) to the gas phase through a potential barrier at the gas–solid interface. The parameters of this barrier depend on the strength of electric field between the catalyst (cathode) and a point probe (anode).

The experiments were performed using a setup described in detail elsewhere [7, 8]. A solid sample and a stainless-steel point (with a tip curvature radius of 2 μm) perpendicular to its surface were placed into a flow reactor. The reactor walls could be heated up to 500 K. The gap between the solid surface and the point tip could be controlled within $d = 2$–20 μm using a bellow manipulator with a micrometric drive mechanism [7]. The solid samples were of three types: a copper plate, phosphorus-doped single crystal silicon with a resistivity of 1 Ω cm, and a 30-nm-thick nickel film deposited onto a silicon crystal substrate. The electron excitation of solids

was provided by the heterogeneous reaction of recombination of atomic hydrogen, H + H $\longrightarrow$ H$_2$, on the sample surface. For this purpose, the flow reactor was purged by spectral-purity (99.995%) hydrogen at a pressure of 50 Pa. Hydrogen molecules were dissociated in a high-frequency gas discharge. During the measurement of the tunneling current, the error caused by the discharge did not exceed 1×10^{-14} A. The optical emission from discharge was absorbed by the Wood horn. While diffusing from the discharge to reactor, vibrationally and electronically excited molecules exhibited on the average no less that 10^3 collisions with gas molecules and lost the excess energy [9]. The mixture of atomic and molecular hydrogen supplied from the discharge tube to the reactor consisted of particles in the ground and vibrationally excited states. The concentration of hydrogen atoms in the reactor measured by thermoprobe was $n = 3 \times 10^{13}$ cm^{-3}. Using a thermocouple and a thermoresistor, it was established that the increase in the sample temperature due to the reaction proceeding on the surface did not exceed 0.2 K.

The electric field strength between the solid surface and the point probe could be varied by applying a controlled bias voltage within $U = \pm(0$–500) V. After switching on the source of H atoms, we observed a jumplike increase (by a factor of 10^3–10^5) in the current of electron emission from the surface of all solid samples as well as from the probe surface. As the sample is kept for ~1 h at a constant electric field strength in an atmosphere containing H atoms, the tunneling current increases several tens of times due to the hydrogen-induced surface cleaning from oxides and the resulting decrease in the work function. For the same reason, the tunneling current exhibits additional sharp increase after heating the samples at $T = 400$ K in an atmosphere containing H atoms. The value of the current depends on the sample material and the applied field strength.
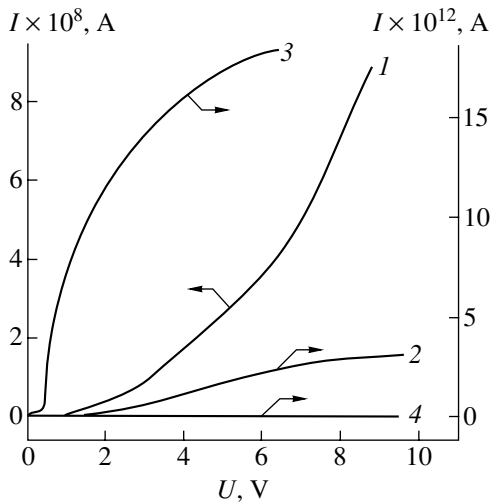
Fig. 1. Current–voltage characteristics for the tunneling emission of electrons from the surface of (*1, 2*) single crystal silicon and (*3, 4*) nickel film measured in a medium of (*1, 3*) atomic hydrogen and (*2, 4*) H_2 molecules; $d = 2$ μm; $T = 295$ K.

The current–voltage characteristics $I(U)$ of the sample–probe system are nonlinear (Fig. 1). Variation of the surface–probe distance d at a fixed bias voltage showed that the tunneling current rapidly decreases with increasing d (Fig. 2). The kinetic curves $I(t)$ showing variation of the current after switching on the source of H atoms (for samples with the surface cleaned by atomic hydrogen) exhibit a complicated behavior, with the shape depending on the sample nature. After switching the source of atomic hydrogen off, the tunneling current rapidly vanishes (Fig. 3).

The observed strong influence of the sample material and the state of its surface on the shape of the $I(t)$, $I(U)$, and $I(d)$ curves indicates that the current is carried by electrons emitted from the sample surface rather
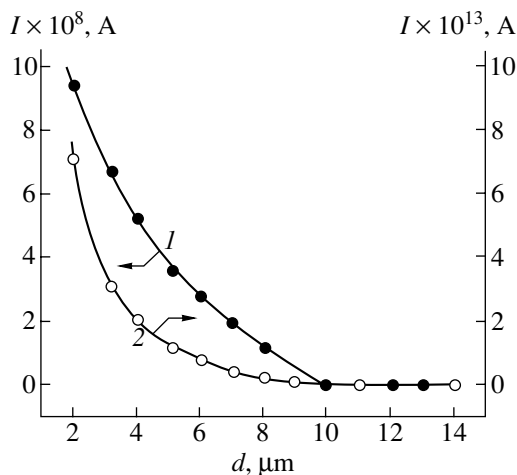
than being transferred from the discharge plasma. Under the experimental conditions studied, switching of the source of atomic hydrogen on and off was accompanied by jumplike changes in the rate J of their heterogeneous recombination on the surface of nickel, copper, and other solids. As a result, the kinetic curve $J(t)$ has the shape of rectangular pulses. The characteristic time of the solid surface filling by adsorbed H atoms is on the order of $\sim 10^2$ s [7, 8, 10], which coincides with the time constant of the tunneling current variation after switching on the source of atomic hydrogen (Fig. 3). Therefore, the shape of the $I(t)$ curves is determined by the process of generation of excited electrons in the course of the heterogeneous reaction $H + H \longrightarrow H_2$ and by the process of variation of the work function as a result of this reaction and the establishment of adsorption equilibrium. The observed current kinetics $I(t)$ corresponds to electron excitation in the recombination events, rather than in the adsorption events.

The yield of reaction-stimulated electron emission per H_2 molecule formed on the surface can be estimated as $\eta = \eta_1\eta_2 = I(\pi eJr^2)^{-1}$, where η_1 is the probability of excited electron generation in the solid during the $H + H \longrightarrow H_2$ conversion, η_2 is the probability of electron tunneling, I is the measured tunneling current, e is the electron charge, $J = 0.25nv\gamma$, v is the average velocity of thermal motion of H atoms in the gas phase, γ is the coefficient of heterogeneous recombination of H atoms on the solid surface ($\gamma \approx 0.1$ for Ni and $\approx 10^{-2}$ for Si), and r is the radius of an emission spot on the cathode surface emitting electrons toward the point anode. For silicon (Fig. 2, curve *1*), the current becomes significant for $d < 10$ μm. Assuming the emission spot radius to be 10 μm and using the values $\gamma = 10^{-2}$ and $I = 9 \times 10^{-8}$ A, we obtain $\eta = 9$. For nickel under analogous conditions ($U = 10$ V), we use the values $\gamma = 0.1$, $I = 3 \times 10^{-11}$ A, and $r = 15$ μm, from which it follows that $\eta = 10^{-4}$. These results

Fig. 2. Plots of the tunneling current of electrons from the surface of single crystal silicon versus the probe–crystal distance d in a medium of (*1*) atomic hydrogen and (*2*) H_2 molecules; $U = 10$ V; $T = 295$ K.
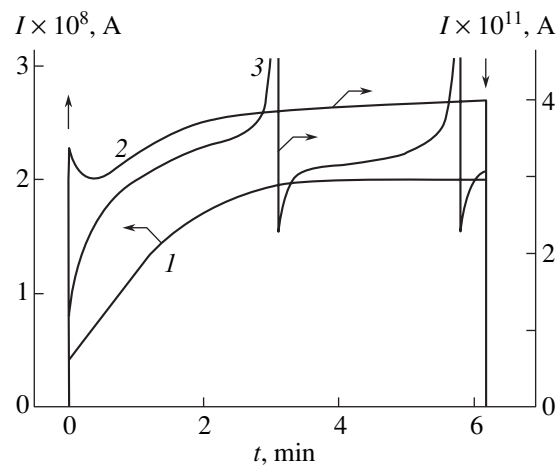

Fig. 3. Time variation of the tunneling current of electrons from the surface of (*1*) single crystal silicon and (*2, 3*) nickel film measured at $U = 4$ (*1*), 70 (*2*), and 100 V (*3*, ordinate divided by a factor of 1.5); $d = 2$ μm; $T = 295$ K.

can be explained as follows. In nickel, the tunneling current is due to electrons excited in the course of reaction. In silicon, atomic hydrogen stimulates the tunneling current by decreasing the work function as result of ionization of the surface electron states in the course of the H + H $\longrightarrow$ H$_2$ reaction, so that the contribution of excited electrons to the tunneling current is negligibly small.

The tunneling current from nickel film on a silicon substrate exhibited autooscillations in atomic hydrogen, whereby the current periodically (for a time of 2–8 s) increased by a factor of 10^3 to reach $I_{max} > 10^{-7}$ A (Fig. 3, curve 2). This phenomenon was reproduced in various samples upon prolonged (~3 h) keeping of a nickel film in atomic hydrogen. During these current autooscillations, the voltage between Ni film and the point probe remained constant. For the current autooscillations to arise, it is necessary that the voltage exceed a certain critical level ($U_{cr} = 80$–400 V) depending on the sample prehistory. An increase in the distance d between the point probe and the solid surface at U = const led to an increase in the period of current oscillations. Heating to a temperature of 400°C decreased the amplitude of current autooscillations by three orders of magnitude and reduced their period by a factor of 5. It was established that the effect of atomic hydrogen on the resistance of the nickel film on a silicon substrate was insignificant. In metals, hydrogen atoms accumulate the energy supplied to the solid, start intensive migration, and escape from the metal, thus stimulating rearrangement of the defect structure of the crystal lattice [12]. The observed behavior can be explained as follows. Featuring the adsorption and absorption of H atoms in the presence of electric field and the recombination reaction H + H $\longrightarrow$ H$_2$, the surface of nickel occurs in a nonequilibrium (stressed) state. Jumplike relaxation of the surface is accompanied by energy evolution, additional electron emission, and hydrogen desorption, after which the cycle is repeated.

Based on the obtained result, we propose a method for monitoring the process of electron accommodation during various chemical reactions at the interface between active gas and solids. According to this, by measuring the curves of $I(E)$, $I_1(E)$, and $A(J)$, where E is the electric field strength, I_1 is the tunneling current in an inert gaseous medium, and A is the work function of the cathode surface, it is possible to obtain information about the energy spectrum of excited electrons generated during the chemical conversion events on the solid surface.

The tunneling current stimulated by a heterogeneous chemical reaction can be measured using a point probe (anode) scanning over the sample (cathode) surface. In this mode, it is possible to obtain information about the structure and distribution of centers responsible for the electron chemoemission. These centers, being involved in the surface energy exchange and favoring stabilization of the intermediate compounds and target products, are active centers of heterogeneous

catalysis. In the first step, the sample is studied in the scanning tunneling microscopy regime at a fixed tunneling current I_1 in an inert gaseous medium in order to determine the surface microrelief. Then, a heterogeneous chemical reaction is initiated and the catalyst surface is scanned at the same tunneling current $I = I_1$. A comparative analysis of the two images provides information on the structure and surface arrangement of the active centers. Let us evaluate the necessary conditions of such an analysis for $\eta = 0.1$ and $I = 10^{-14}$ A. In order to study the structure of the centers of heterogeneous catalysis, it is necessary to provide for a spatial resolution on the order of ~10^{-9} m, which requires that $r \approx 10^{-9}$ m and $J = (\pi e \eta r^2)^{-1} \approx 2 \times 10^{23}$ m^{-2} s^{-1}. This value of the reaction rate can be achieved for a large number of heterogeneous reactions. For example, the reaction of atomic hydrogen recombination on the surface of silicon proceeds at this rate if the concentration of H atoms in the gas phase is $n = J(0.25 v\gamma)^{-1} = 3 \times 10^{22}$ m^{-3}.

The surface of a catalyst is always inhomogeneous. Using the proposed method, it is possible to assess the role of this inhomogeneity in the acceleration of heterogeneous reactions, to establish the existence of active centers, to determine the catalytic activity of separate parts of the surface microrelief, to monitor the dynamics of the catalytic activity, and to study the relationships between the activity of microinhomogeneities and their structure, rearrangement, degradation, and sputtering in the course of reaction.

REFERENCES

1. F. F. Vol'kenshteĭn, A. N. Gorban', and V. A. Sokolov, *Radical-Recombination Luminescence of Semiconductors* (Nauka, Moscow, 1976) [in Russian].
2. V. P. Grankin and V. V. Styrov, Pis'ma Zh. Éksp. Teor. Fiz. **31**, 403 (1980) [JETP Lett. **31**, 375 (1980)].
3. V. F. Kharlamov, Kinet. Katal. **20**, 946 (1979).
4. V. F. Kharlamov, Izv. Vyssh. Uchebn. Zaved. Fiz., No. 2, 125 (1977).
5. V. V. Barelko, Yu. E. Volodin, and E. S. Gen'kin, Teor. Osn. Khim. Tekhnol. **29** (1), 46 (1995); **29** (2), 192 (1995).
6. T. Greber, Chem. Phys. Lett. **222**, 292 (1994).
7. V. F. Kharlamov, E. P. Krutovskiĭ, Yu. V. Mosin, *et al.*, Pis'ma Zh. Tekh. Fiz. **24** (5), 23 (1998) [Tech. Phys. Lett. **24**, 176 (1998)].
8. V. F. Kharlamov and T. S. Rogozhina, Zh. Fiz. Khim. **77**, 632 (2003).
9. P. Borrell, *Molecular Relaxation Processes* (Chemical Society, London, 1966), pp. 263–267.
10. V. F. Kharlamov, T. S. Rogozhina, A. V. Barmin, *et al.*, Pis'ma Zh. Tekh. Fiz. **28** (13), 67 (2002); **29** (7), 87 (2003) [Tech. Phys. Lett. **28**, 564 (2002); **29**, 305 (2003)].
11. M. U. Kislyuk, Khim. Fiz., No. 1, 59 (1989).
12. Yu. I. Tyurin and I. P. Chernov, Dokl. Akad. Nauk **367**, 328 (1999) [Dokl. Phys. **44**, 427 (1999)].

Translated by P. Pozdeev

Europium Diffusion
in Single Crystal Samarium Sulfide

V. A. Didik*, E. A. Skoryatina, V. P. Usacheva,
A. V. Golubkov, and V. V. Kaminskiĭ

Ioffe Physicotechnical Institute, Russian Academy of Sciences, St. Petersburg, 194021 Russia
* e-mail: didik@mail.ioffe.ru
Received March 31, 2004

Abstract—The process of europium diffusion in samarium sulfide (SmS) has been studied for the first time. Experiments performed with ^{152}Eu radioactive isotope in a temperature interval from 950 to 1050°C showed that the diffusion coefficient varies within 10^{-12}–10^{-9} cm^2/s and depends on the temperature as $D = 6 \times 10^{19}\exp(-6.18/kT)$. It is concluded that Eu impurity atoms diffuse in the SmS lattice predominantly via the lattice sites. © *2004 MAIK "Nauka/Interperiodica".*

The need for studying the diffusion of europium in samarium sulfide arose in the course of investigations of the phenomenon of thermo emf in this semiconductor compound, since the carrier generation onset temperature and the thermo emf depend on the impurity concentration [1]. On the other hand, SmS and EuS are known to crystallize in the NaCl type structures with very close lattice parameters (5.967 and 5.968 Å, respectively). Semiconductors with lattice mismatch below 0.01 Å are considered most promising systems for the creation of heterostructures [2]. Taking into account the significant difference between the band structures of SmS and EuS (in particular, in the energies of 4f levels [3]), in combination with good compatibility of thermal, electrical, and crystallochemical properties, the investigation of heterostructures based on these compounds is of considerable interest. In this context, the study of mutual diffusion in such heterostructures is the task of primary importance.

The experiments were performed with $8 \times 5 \times 3$-mm plane-parallel SmS plates cut via the (100) cleavage plane from a single-crystalline ingot grown as described in [4]. The samples were plane-parallel to within ±2 μm, which was ensured by high-precision dry grinding on fine emery papers and controlled with the aid of an IKV-1 optical meter (1-μm scale).

The process of diffusion was studied using ^{152}Eu radioactive isotope, which was deposited from an ethanol solution onto one large face of an SmS plate. The substrate with a deposited isotope layer was placed into a tantalum container (preventing the interaction between SmS and quartz) and sealed into an evacuated quartz ampule. The diffusion annealing of samples in vacuum was performed in a temperature interval from 950 to 1050°C; the duration of annealing was varied from 1 to 21 h. The annealing was effected in furnaces of the

SDO-125/4-4 type equipped with a programmable temperature controller (REPID) capable of maintaining a preset temperature to within ±2 K. After annealing, the ampules were cooled in air and the samples were extracted. The sample edges were ground off to a depth of no less that 500 μm in order to eliminate the contribution of the radioactive impurity from edges on the tracer activity in measured layers. Then, the samples were characterized by radiography so as to evaluate the homogeneity of impurity distribution over the sample area.

The impurity concentration–depth profiles were studied using the method of sequential layer removal. According to this, the tracer activity is measured in the material of thin layers sequentially removed from a sample by grinding on an emery paper with the aid of a special sample holder. The thickness of a removed layer was determined using an IKV-1 optical meter. The measurements of radioactivity (γ emission from removed layers) were performed using a BDZA2-01 detector with a NaI(Tl) scintillation crystal and the corresponding counting electronics.

The absolute concentrations of the tracer were determined using a coefficient of proportionality between the measured activity and the impurity content. This coefficient was preliminarily determined by measuring the activity of standard samples with known concentrations of the given radioactive isotope. Using the absolute values of the tracer concentrations c and thicknesses of sequentially removed layers, we constructed the concentration–depth profiles $c = f(x)$, where x is the coordinate measured from the sample surface.

Using the method described above, we obtained the concentration–depth profiles of ^{152}Eu radioactive iso-
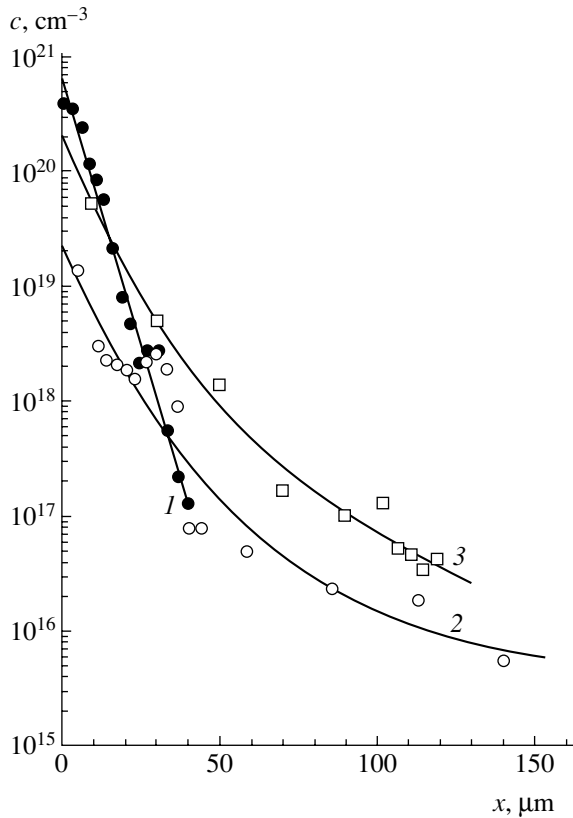
Fig. 1. Europium concentration–depth profiles in samarium sulfide at various temperatures: (*1*) $T = 950°C$ (annealing time, $t = 21$ h); (*2*) $T = 1000°C$ (10 h); (*3*) $T = 1050°C$ (1 h).

Fig. 2. The temperature dependence of the diffusion coefficient D of europium in samarium sulfide.

tope in SmS single crystals annealed for various times at different temperatures, which had the shape of monotonically decreasing curves. Figure 1 shows the concentration–depth profiles of [152]Eu in SmS samples annealed at 950, 1000, and 1050°C. As can be seen from these data, the depth of tracer diffusion under these conditions reaches 40–150 μm. It should be noted that, as expected, the maximum tracer penetration depth at a given annealing time increases with the temperature. The concentration of [152]Eu is 10^{19}–10^{21} cm^{-3} at the sample surface and decays to 10^{15}–10^{16} cm^{-3} in the bulk.

The process of europium impurity diffusion in SmS can be described by Fick's differential equation, which can be written in the one-dimensional case as [5]

$$\partial c/\partial t = D(\partial^2 c/\partial x^2), \qquad (1)$$

where D is the diffusion coefficient [5]. Since the thickness of our samples was much greater than the tracer penetration depth, the sample could be considered as a semi-infinite medium initially free of the diffuser, which corresponds to the case of diffusion from the so-called steady source.
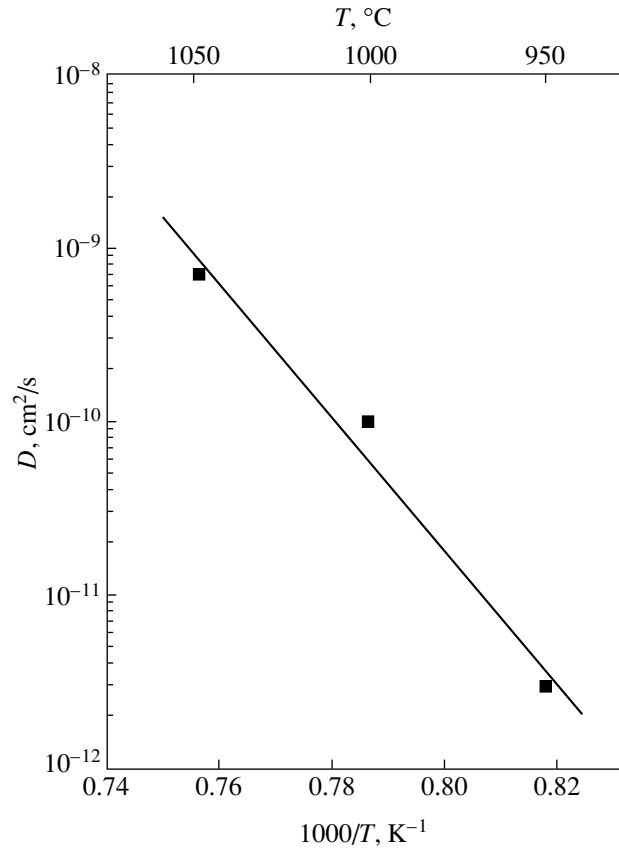
A solution to Fick's equation in the case under consideration is given by the formula

$$c(x, t) = c_0 \text{erfc}(x/2\sqrt{D}t). \qquad (2)$$

Using the method of calculation of the diffusion coefficient described in [6], we determined D with an accuracy of 25%. Taking into account that the temperature dependence of the diffusion coefficient observed in our experiments obeyed the Arrhenius relation,

$$D = D_0 \exp(-\varepsilon/kT), \qquad (3)$$

we determined the main diffusion parameters: the diffusion activation energy ε and the preexponential factor D_0.

According to the results of our experiments, europium diffusion into single crystal SmS in the temperature interval studied is characterized by the diffusion coefficients $D = 10^{-12}$–10^{-9} cm^2/s, an activation energy of 6.18 eV, and $D_0 = 6 \times 10^{19}$ cm^2/s (Fig. 2). The temperature dependence of the diffusion coefficient can be described by the expression $D = 6 \times 10^{19} \exp(-6.18/kT)$. Judging by the values of the activation energy and the diffusion rate, we suggest that Eu

impurity atoms diffuse in the SmS lattice predominantly via the lattice sites.

REFERENCES

1. V. V. Kaminskiĭ, A. V. Golubkov, and L. N. Vasil'ev, Fiz. Tverd. Tela (St. Petersburg) **44**, 1501 (2002) [Phys. Solid State **44**, 1574 (2002)].

2. G. Kremer, Usp. Fiz. Nauk **172**, 1087 (2002).

3. V. P. Zhuze, Zh. Vses. Khim. O–va im. D.I. Mendeleeva **26**, 695 (1981).

4. A. V. Golubkov, E. I. Goncharova, V. P. Zhuze, G. M. Loginov, V. M. Sergeeva, and I. A. Smirnov, *Physical Properties of Rare-Earth Chalcogenides* (Nauka, Leningrad, 1973) [in Russian].

5. B. I. Boltaks, *Diffusion in Semiconductors* (Fizmatgiz, Moscow, 1961; Academic Press, New York, 1963).

6. R. Sh. Malkovich, *Mathematics of Diffusion in Semiconductors* (Nauka, St. Petersburg, 1999) [in Russian].

Translated by P. Pozdeev

Textured Tin Dioxide Films
for Gas Recognition Microsystems

V. V. Sysoev, N. I. Kucherenko, and V. V. Kissin*

Saratov State Technical University, Saratov, Russia
* e-mail: kisin@sstu.ru
Received November 3, 2003; in final form, April 26, 2004

Abstract—We have studied the microstructure, electrical properties, and gas sensor characteristics of thin tin dioxide (SnO_2) films obtained by RF magnetron sputtering of an oxide target. The synthesized films are composed of crystalline rods with a diameter of 10–60 nm and a length of up to 1000 nm oriented perpendicularly to the substrate plane. This morphology facilitates the access of gas molecules to the side surfaces of crystallites. Use of such SnO_2 films in a multisensor microsystem expanded the spectrum of recognized gases. © *2004 MAIK "Nauka/Interperiodica".*

Thin SnO_2 films have been successfully used in the active layers of multisensor systems of gas analysis [1, 2]. Materials for such systems must provide for the effective modulation of the sensor conductivity in response to adsorbed particles. In polycrystalline semiconductor thin-film detectors, this condition is satisfied for a grain size not exceeding the Debye length [3–5]. In addition, it is necessary to provide for the access of molecules from the gas phase to the semiconductor surface. It is expected that both conditions can be met in gas recognition systems using ultradisperse films with developed internal surface [6–8]. In this context, development of the methods of synthesis of such films and investigation of their sensitivity to gases are of considerable importance.

Previously [2], we demonstrated that tin oxide (SnO_2) films deposited by RF magnetron sputtering of an oxide target and then recrystallized by high-temperature annealing in oxygen can be used for the formation of a multisensor system distinguishing acetone and ammonia vapors. However, some other pairs (for example, acetone and ethanol) were classified into the same group. However, the process of crystallization and, hence, the properties of deposited films can be controlled immediately in the course of deposition [9–11]. This paper reports on the results of investigation of SnO_2 films obtained by RF magnetron sputtering of an oxide target with additional supply of a volatile film component (oxygen) by directed flow to deposition zone.

The films were synthesized in a planar magnetron sputtering system. The target had the shape of a 2-mm-wide ring with a diameter of 50 mm. The distance from the target to the substrate was three times the target diameter. The flow of an argon–oxygen (3 : 1) working gas mixture was uniformly supplied to the target region and pumped from the substrate side. The gas mixture composition and flow rate were controlled using needle leak valves and electronic flow meters (DRG-1). The total gas pressure in the chamber during deposition was 3×10^{-3} Torr; the discharge power density at the target was 80 W/cm^2; and the substrate temperature was 250°C. The deposition was performed in the regime of stabilized self-sustained target bias potential. The substrate holder was electrically insulated; the anode, having the shape of a truncated cone, was situated between the target and the substrate and was grounded.

The SnO_2 films were deposited onto polycrystalline sapphire (Polycor) substrates of two types:

(A) Rectangular $1 \times 5 \times 10$-mm plates with metal (Fe/Cr) contacts with a 100-μm gap preliminarily formed on the surface. The samples deposited onto such substrates were used for the investigation of electrical properties and morphology of the films.

(B) Square $0.3 \times 10 \times 10$-mm plates with a system of coplanar platinum (Pt) electrodes preliminarily formed on the front surface and resistive Pt heaters formed on the rear surface. The distance between electrodes was 100 μm, which allowed 38 sensor segments to be obtained on each sample. The sensor topology is described in more detail elsewhere [12]. These samples were used for the investigation of gas sensor characteristics and the ability of the multisensor microsystem to recognize gases.

The film thickness was measured using a Tencor P-10 stylus profilometer (KLA-Tencor Co, USA). The film composition and morphology were studied using a STADi-P X-ray diffractometer (STOE Co, Germany) and an FESEM DSM 982 Gemini scanning electron microscope (LEO Co, Germany).

The gas sensor characteristics of the films were studied using a KAMINA electronic nose system (Forschungszentrum Karlsruhe GmBH, Germany) [11]. For
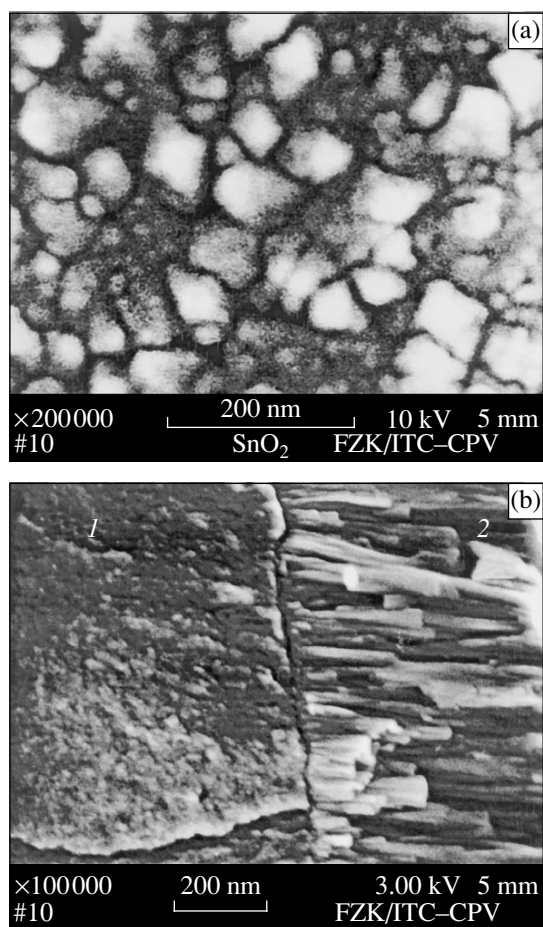
Fig. 1. SEM micrographs of (a) the surface and (b) transverse cross section (cleavage) of a tin oxide film (*1* and *2* are Pt electrode and SnO_2 layer, respectively).

this purpose, B type samples were incorporated in and connected to a 120-pin PGA-120 case (Kyocera Co, Japan). The resistance of each sensor element was measured using the corresponding pair of electrodes at a retrieval rate of 30 ms per segment. Homogeneity of the film surface heating was monitored using an IR camera of the Thermo Tracer TH3100MR type (NEC Sanei Instruments Ltd., Japan). The sample structure surface temperature was maintained on a level of 350°C.

The gas recognition ability was studied using a set of test gases (TGs) representing air mixtures with ethanol, propanol, acetone, and ammonia vapors. The TG humidity was determined using a TFA type device. For the gas recognition test, a sample was mounted in a chamber with a volume of about 50 cm³, to which TGs were admitted in a cyclic flow regime in the following order: air–TG1–air–TG2–air–TG2–air–TG3–air. The time of exposure to each TG was 1 min. The sensitivity with respect to a given TG was determined as the ratio of the sensor segment resistances measured in air and in this TG. The recognition ability of the microsystem with respect to a given TG was characterized by the

ratio of the number of cycles with correct recognition using the linear discriminant analysis (LDA) to the total number of exposures to this TG.

The film thicknesses varied from 100 to 1000 nm, depending on the deposition time. Examination of the film surface morphology showed that the size of crystallite edges emerging at the film surface varied within 10–60 nm and was virtually independent of the deposited layer thickness (Fig. 1a). Figure 1b shows a micrograph of the transverse cross section (cleavage surface) of a 600-nm-thick film, which shows that the film is composed of crystalline rods with a diameter of 10–60 nm and a length equal to the layer thickness. This orientation of rods favors the access of gas molecules to the side surface of crystallites.

The results of X-ray diffraction measurements did not reveal any phases other than tin dioxide. Using measurements with a crystal monochromator, the average grain edge size was evaluated by the Scherer formula as approximately 20 nm. This result agrees with the data of scanning electron microscopy (SEM) and indicates that a considerable fraction of the grain volume is crystalline.

The results of investigation of the electrical properties of SnO_2 films showed that the scatter of resistances of sensor segments in the structures of type B measured in vacuum coincides with the degree of nonuniformity of the layer thickness over the sample area (10–15%). In air, the scatter of the resistance was several tens of times greater than the degree of variation of the layer thickness, composition, or morphology (Fig. 2d). The admission of TGs to the test chamber modified the resistances of segments (Figs. 2a–2c) in a reproducible manner, whereby the particular segments exhibited up to a 100-fold change in the resistance. According to [13, 14], we used the LDA method to construct a computer model of the microsystem response to the action of TGs. After calibration, the recognition ability of the multisensor microsystem studied was no less than 86% and was virtually independent of the TG concentration and the humidity (in the *RH* = 30–60% range). The proposed system not only distributed TGs between the groups of pure air, ammonia vapor, and inflammable fluids (as in [2]), but it even recognized particular TGs in the latter group, distinguishing between acetone, ethanol, and propanol vapors (Fig. 3).

It should be noted that the SnO_2 films used in these experiments differed from those studied previously [2]: a decrease in the transverse size of crystallites improved the gas recognition ability of the new microsystems. Since the recognition of gases is based on the uncorrelated response of sensors to various gases, the difficulties in distinguishing gases (e.g., ethanol versus acetone vapors) producing a like physicochemical action upon the film sensors, which were encountered in [2], can be related to the fact that a change in the resistance of SnO_2 under the action of such substances are proportional in a broad range of concentrations
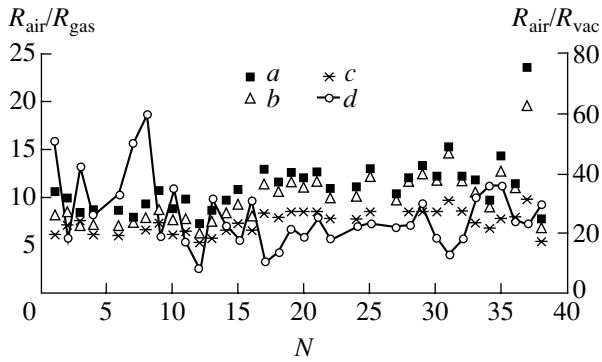
Fig. 2. The pattern of the gas sensitivity of sensor segments in a B type microstructure based on a 1000-nm-thick SnO_2 film, characterized by the ratio of the element resistances measured in air (R_{air}) and in a given TG (R_{gas}) or in vacuum (R_{vac}): (*a*) acetone; (*b*) ethanol; (*c*) propanol; (*d*) vacuum; *N* is the ordinal number of a sensor segment in a 38-segment microstructure.
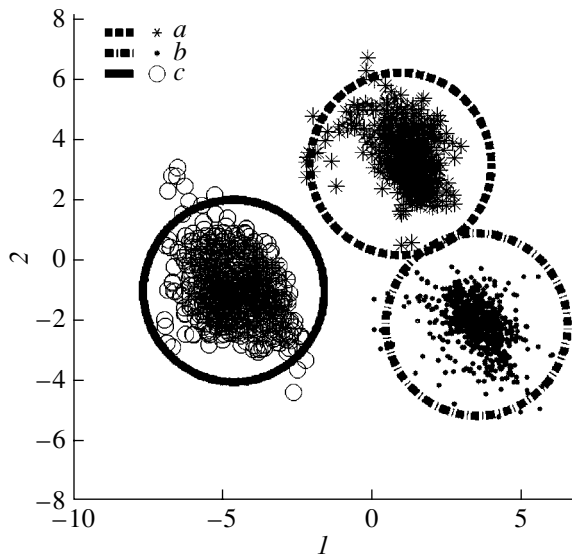

Fig. 3. The results of testing a B type microstructure based on a 1000-nm-thick SnO_2 film in a KAMINA electronic nose system, showing the plot of LDA components 1 versus 2 for various TGs: (*a*) acetone; (*b*) ethanol; (*c*) propanol. Each experimental point corresponds to a microsystem response to a single exposure; ellipses bound the region of TG recognition with a confidence probability of 0.99.

(see [15]). In the films synthesized in this study, the difference in the response of sensors to different TGs has increased. This is probably related to the fact that sensors operate at the edge of the dependence of their sensitivity on the crystallite size (the position of this edge varies with the gas type). Such a shift of the sensitivity edge was observed [16] upon modification of the surface microrelief. Elucidation of this mechanism in more detail requires further investigations.

Thus, the results of this study showed that the passage to films with the transverse size of crystallites

within 10–60 nm decreased the correlation between responses of the sensor segments to the action of TGs. This circumstance improved the gas recognition ability and expanded the spectrum of reliable recognized substances. In particular, the new microsystem not only identifies ammonia vapor but also distinguished rather close (in physical and chemical properties) vapors of acetone, ethanol, and propanol.

REFERENCES

1. J. Gardner and K. C. Persaud, in *Proceedings of the 7th International Symposium on Olfaction and Electronic Nose, Brighton, 2000* (IOP, Bristol, 2000).
2. V. V. Kisin, V. V. Sysoev, and S. A. Voroshilov, Pis'ma Zh. Tekh. Fiz. **25** (16), 54 (1999) [Tech. Phys. Lett. **25**, 657 (1999)].
3. M. J. Madou and S. R. Morrison, *Chemical Sensing with Solid State Devices* (Academic, London, 1991).
4. H. Ogawa, M. Nishikawa, and A. Abe, J. Appl. Phys. **53**, 4448 (1982).
5. V. V. Kissin, V. V. Sysoev, and S. A. Voroshilov, Appl. Phys. Lett. **76**, 2391 (2000).
6. B. Panchapakesan, D. L. De Voe, M. R. Wildmaeir, *et al.*, Nanotechnology **12**, 336 (2001).
7. Z. W. Pan, Z. R. Dai, and Z. L. Wang, Science **291**, 1947 (2001).
8. E. Comini, G. Faglia, G. Sberveglieri, *et al.*, Appl. Phys. Lett. **81**, 1869 (2002).
9. V. V. Kisin, S. A. Voroshilov, V. V. Sysoev, *et al.*, Zh. Tekh. Fiz. **69** (4), 112 (1999) [Tech. Phys. **44**, 452 (1999)].
10. R. Snyders, M. Wautelet, R. Gouttebaron, *et al.*, Surf. Coat. Technol. **142**–**144**, 187 (2001).
11. V. V. Kissin, S. A. Voroshilov, and V. V. Sysoev, Thin Solid Films **348**, 307 (1999).
12. P. Althainz, J. Goschnick, S. Ehrmann, *et al.*, Sens. Actuators B **33**, 72 (1996).
13. P. C. Jurs, G. A. Bakken, and H. E. McClelland, Chem. Rev. **100**, 2649 (2000).
14. R. Henrion and G. Henrion, *Multivariate Datenanaluse* (Springer-Verlag, Berlin, 1995) [in German].
15. S. I. Rembeza, T. V. Svistova, E. S. Rembeza, and O. I. Borsyakova, Fiz. Tekh. Poluprovodn. (St. Petersburg) **35**, 796 (2001) [Semiconductors **35**, 762 (2001)].
16. M. V. Bestaev, D. Ts. Dimitrov, A. Yu. Il'in, *et al.*, Fiz. Tekh. Poluprovodn. (St. Petersburg) **32**, 654 (1998) [Semiconductors **32**, 587 (1998)].

Translated by P. Pozdeev

Photosensitivity of Surface Barrier Structures Based on Cu(In,Ga)Se₂ Films Grown by Codeposition in Vacuum

V. Yu. Rud'[a],*, Yu. V. Rud'[b], V. F. Gremenok[c], and G. A. Il'chuk[d]

[a] *St. Petersburg State Technical University, St. Petersburg, Russia*
[b] *Ioffe Physicotechnical Institute, Russian Academy of Sciences, St. Petersburg, Russia*
[c] *Institute of Solid State and Semiconductor Physics, National*
Academy of Sciences of Belarus, Minsk, Belarus
[d] *"Lvivska Politekhnika" National University, Lvov, Ukraine*
* e-mail: rudvas@spbstu.ru
Received March 24, 2004

Abstract—Polycrystalline Cu(In,Ga)Se₂ (CIGS) films with various ratios of Cu, In, and Ga were grown by codeposition of all elements in vacuum. The X-ray diffraction study showed that the films are single-phase and possess a chalcopyrite structure with predominant [112] orientation. The films exhibited a mirror smooth surface and had a close-packed structure composed of crystallites with clear faceting and a transverse size of 0.1–0.3 μm. Related surface barrier structures of the (In,Ag)/Cu(In,Ga)Se₂ type were obtained and their spectra of the quantum efficiency of photoconversion were studied. The obtained structures can be used for optimization of the CIGS film technology. © 2004 MAIK "Nauka/Interperiodica".

Introduction. The broad class of ternary analogues of $A^{II}B^{VI}$ semiconductor compounds, obtained by substituting atoms of groups I and III for two atoms of group II contains more than 30 semiconductors. The transition to ternary or more complicated compounds significantly expands the possibilities of the technology of semiconductor materials. In this class of compounds, direct-band solid solutions of the $CuIn_xGa_{1-x}Se_2$ (CIGS) system, possessing a high optical absorption coefficient ($\alpha > 5 \times 10^4$ cm^{-1}), high thermal stability, and radiation resistance, are considered as most promising materials for low-cost solar cells [1, 2]. By means of simultaneous molecular beam epitaxy of all component elements (Cu, In, Ga, and Se), high-quality CIGS films were obtained and prototype solar cells with record efficiency ($\eta = 19.2\%$) were created [3]. However, the photosensitivity of CIGS films is still insufficiently studied.

This investigation was devoted to the creation of photosensitive CIGS-based thin-film structures. Below, we present the first results concerning the photoelectric properties of surface barrier structures of the (In,Ag)/Cu(In,Ga)Se₂ type.

Synthesis and structure of thin CIGS films. CIGS films with a thickness of 1.3–1.5 μm and various ratios of Cu, In, and Ga were synthesized by means of simultaneous evaporation and codeposition of all elements in vacuum. The temperature of selenium evaporator was 390°C. CIGS films were deposited onto substrates heated to 400–420°C. The substrates were made of usual soda glass with or without molybdenum coating (depending on the experiment). The pressure in the chamber during film deposition did not exceed $(5–10) \times 10^{-6}$ mBar.

The results of quantitative analysis of the obtained CIGS films showed homogeneous distribution of all elements over the sample surface. Table 1 presents data on the content of components in two typical samples. The X-ray diffraction investigation showed that the deposited layers are single-phase and possess a chalcopyrite structure with predominant [112] orientation. In addition to the typical series of lines (112, 220/204, 312/116, etc.), the diffraction patterns exhibited superlattice reflections (101, 103, and 211) and revealed tetragonal splitting of 116/312 doublets characteristic of the ordered structure of chalcopyrite.

The surface morphology of CIGS films was studied using Stereoscan 360 scanning electron microscope (SEM). All CIGS films obtained by codeposition in

Table 1. Elemental composition and electrical properties of two *p*-CIGS films at *T* = 300 K

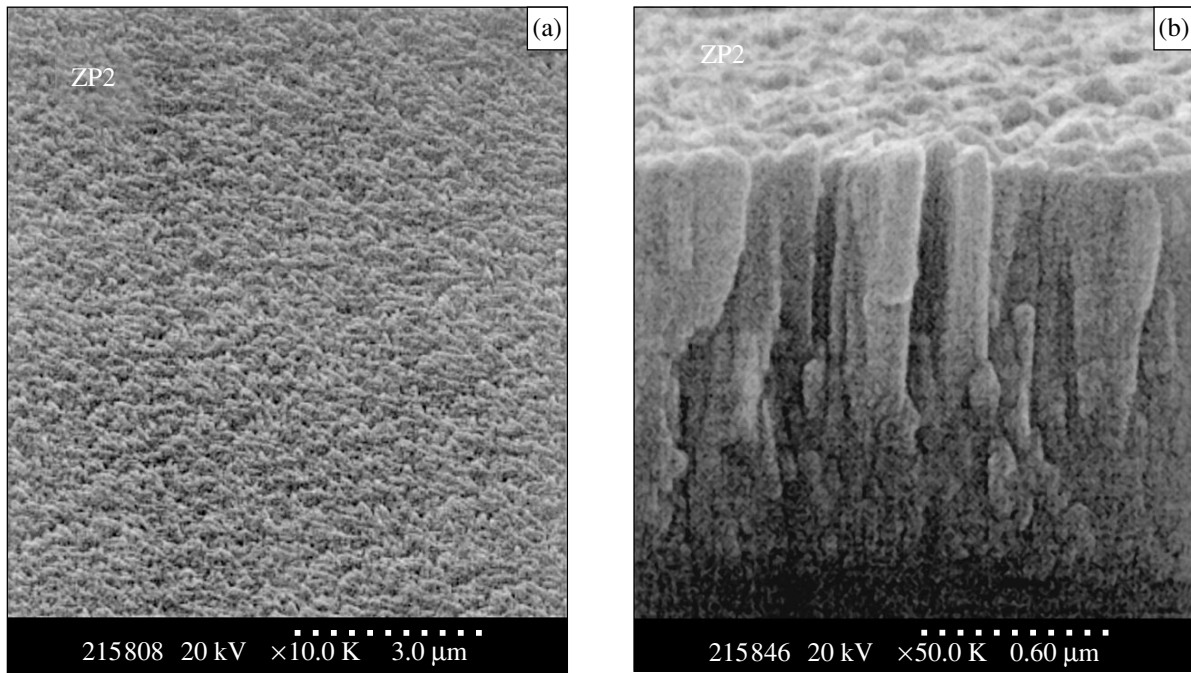| Sample	Conductivity type	ρ, Ω cm	Content, at. %			
			Cu	In	Ga	Se
ZP3-4	*p*	10^3–10^4	26.75	22.23	5.36	45.47
ZP2	*p*	10^8–10^{10}	17.02	26.60	7.89	48.51

Fig. 1. SEM micrographs of (a) the surface and (b) the cross section (cleavage) of a CIGS film (magnification, ×50000).

vacuum exhibited a mirror smooth surface and had a close-packed structure (Fig. 1a), which confirmed the single-phase character of the deposit revealed by the X-ray diffraction data. Examination of the transverse sections showed a dense structure composed of coherently packed crystallites with clear faceting and an average diameter of 0.1–0.3 μm (Fig. 1b). The direction of growth was perpendicular to the substrate plane. All CIGS films exhibited *p*-type conductivity; the resistivity of samples showed a clear tendency to decrease with increasing copper content (Table 1).

Surface barrier structures. The samples of surface barrier structures based on CIGS films were obtained by thermal deposition of a film of pure indium with a thickness of $d \approx 0.05$ mm. Even without any thermal treatment such In/CIGS structures exhibited rectifying properties. The rectification coefficient K determined as the ratio of forward and reverse currents at a bias voltage of $U \approx 50$ V we relatively low ($K \approx 5–20$). The forward current was passed in the direction corresponding to a positive polarity of the bias voltage on the CIGS film. We have also prepared surface barrier structures of the Ag/CIGS type. It is important to note that a system of spatially separated surface barrier structures with a width of about 0.7 mm formed on the same CIGS film showed a high local homogeneity of the photoelectric characteristics of such structures. This result confirms the data of the electron-probe microanalysis showing the lateral homogeneity of CIGS deposits.

Illumination of the In/CIGS structures gives rise to photo emf with a positive polarity typically on the CIGS film. The sign of the photo emf depends neither on the geometry of the exposure nor on the photon energy. The maximum voltage photoresponse of the best sample structures amounted to $S_U^m \approx 10^3$ V/W at $T = 300$ K and was usually observed for illumination from the barrier contact side.

Figure 2 (curve *1*) shows the typical spectrum of the quantum efficiency of photoconversion $\eta(\hbar\omega)$ for the surface barrier structures of the In/CIGS and Ag/CIGS types. As can be seen, η exhibits exponential growth for $\hbar\omega > 0.95$ eV with a slope of $S = \delta(\ln\eta)/\delta(\hbar\omega) \approx 29$ eV^{-1}. According to [4], such a high slope is indicative of the direct interband optical transitions. This conclusion agrees with the data reported previously for the bulk single crystals of CIGS solid solutions [3, 5].

At a photon energy of $\hbar\omega \approx 1.10$ eV, the $\eta(\hbar\omega)$ spectrum of the obtained surface barrier structures usually exhibits a change from exponential to parabolic behavior. At $\hbar\omega > 1.3$ eV, the photoresponse reaches a maximum level and remains virtually constant up to $\hbar\omega \approx 2.8$ eV. As can be seen from Fig. 2 (curve *2*), the long-wavelength photoresponse of the In/CIGS Schottky

Table 2. Room-temperature photoelectric characteristics of (In,Ag)/*p*-CIGS structures (formed on ZP2 film sample)

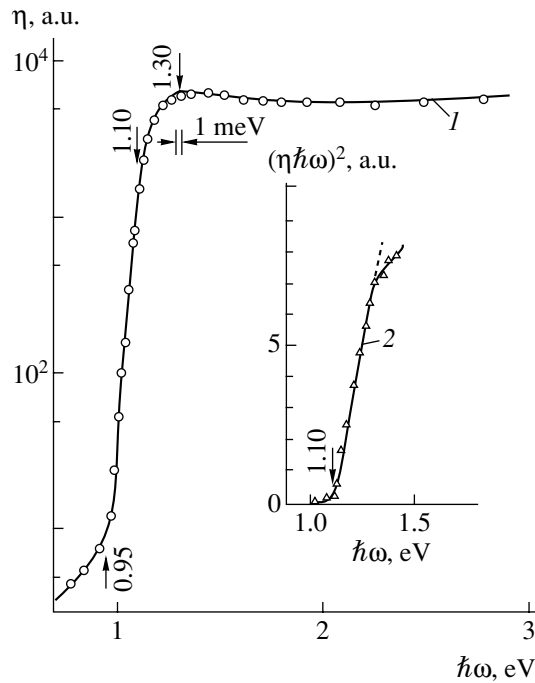| Structure	S_U^m, V/W	$\hbar\omega^m$, eV	E_g, eV
In/*p*-CuInGaSe$_2$	1000	1.3–2.7	1.10
Ag/*p*-CuInGaSe$_2$	350	1.3–2	1.10

Fig. 2. The spectrum of the relative quantum efficiency of photoconversion $\eta(\hbar\omega)$ (curve *1*) for the In/CIGS surface barrier structure (sample ZP2, $T = 300$ K) illuminated from the side of the barrier contact. The inset shows the plot of $(\eta\hbar\omega)^2$ versus $\hbar\omega$ (curve *2*).

barriers is linearized in the coordinates of $(\eta\hbar\omega)^2$ versus $\hbar\omega$. According to [4], this is evidence of the direct interband transitions. The extrapolation for $(\eta\hbar\omega)^2 \longrightarrow 0$ gives the bandgap width $E_g \approx 1.10$ eV at $T = 300$ K. This estimate is somewhat greater than the bandgap width

reported for an ordered stoichiometric CuInSe$_2$ [5], which is probably related to the formation of solid solutions. Analogous results were obtained from the study of the spectral photosensitivity of Ag/CIGS structures. Note that the Schottky structures studied are characterized by a broad spectral range of maximum photoresponse (Table 2).

Conclusions. On the whole, the obtained results demonstrate the possibility of using the process of codeposition in vacuum for obtaining photosensitive structures based on CIGS solid solutions. The results of investigation of the photoresponse of CIGS-based surface barrier structures obtained by this rapid method can be used for optimization of the CIGS film technology.

REFERENCES

1. *Current Topical in Photovoltaics*, Ed. by T. Coutts and J. Meakin (Academic Press, London, 1985; Mir, Moscow, 1988).

2. L. Kazmerski, Renew. Sustain. Energy Rev. **1** (1–2), 71 (1997).

3. U. Rau and H. W. Shock, Ser. Photoconversion Solar Energy **1**, 277 (2001).

4. J. I. Pankove, *Optical Processes in Semiconductors* (Prentice-Hall, Englewood Cliffs, N.J., 1971; Mir, Moscow, 1973).

5. T. J. Coutts, L. L. Kazmerski, and S. Wagner, *Copper Indium Diselenide for Photovoltaic Applications* (Pergamon, Amsterdam, 1986).

Translated by P. Pozdeev

Peculiarities of the MBE Growth of Nanowhiskers on GaAs(100) Substrates

I. P. Soshnikov[a], A. A. Tonkikh[b], G. E. Cirlin[a], Yu. B. Samsonenko[a], and V. M. Ustinov[a]

[a] Ioffe Physicotechnical Institute, Russian Academy of Sciences, St. Petersburg, Russia
[b] Institute of Analytical Instrument Building, Russian Academy of Sciences, St. Petersburg, Russia

Received March 26, 2004

Abstract—We have studied the formation of nanowhiskers (NWs) by molecular beam epitaxy (MBE) on GaAs(100) substrates. The MBE growth of NWs exhibits two stages (initial and developed) and leads to the formation of NWs with surface morphology of two types (nucleation and intergrowth). The stage of developed growth is characterized by the predominant formation of intergrown NWs oriented in the $\langle 111 \rangle$B direction, having (110) habit (including the NW tip surface) and hexagonal cross sections with a transverse size within 50–300 nm. It was found that the transverse size of a hexagonal NW may significantly differ from that of an Au–GaAs melt droplet. The ratio of longitudinal and transverse dimensions of intergrown NWs can be on the order of 150 and above. When the transverse size of NWs exceeds a certain value (about 200 nm), the crystal length exhibits a slight decrease. The existence of two types of morphology is indicative of inhomogeneous character of the NW growth on a GaAs(100) surface, which depends on the catalyst droplet size, effective thickness of the deposited GaAs layer, and the growth temperature. © 2004 MAIK "Nauka/Interperiodica".

Anisotropic semiconductor crystals—whiskers—are promising materials for opto- and microelectronic devices such as light-emitting diodes, photodiodes, microchromatographs, and multipoint electron emitters. The formation of whiskers was discovered in the 1950s [1]. A combined three-phase mechanism of whisker growth was originally proposed by Wagner and Ellis [2] and then developed by Givargizov and Chernov [3, 4] in the form of the vapor–liquid–crystal (VLC) model. Subsequently, the formation and physical properties of whiskers grown in various systems have been extensively studied [3, 5–7]. In the early stage of development of the whisker growth technology, it was impossible to ensure a regular growth of whiskers with a transverse size significantly below 1000 nm, which hindered the wide use of such crystals. The only method capable of providing filamentary nanostructures was based on the formation of whisker-like surface morphology in the course of ion beam etching of some crystals [8–10]. Investigations of the formation of this surface morphology were rather few and the developed approach was inapplicable to semiconductor materials such as GaAs and Si.

Considerable interest in nanowhiskers or nanowires (NWs) arose in the past two decades due to the development of new vapor phase epitaxy technologies such as chemical vapor deposition (CVD), in particular, metalorganic CVD (MOCVD), and molecular beam epitaxy (MBE). Using these methods, it is possible to obtain whiskers with characteristic transverse dimensions on the order of several tens of nanometers [11–13]. Previously [14], we studied the peculiarities and laws of the formation of NWs on a (111)B-oriented GaAs surface. This study, continuing these investigations, was aimed at determining the possibilities and peculiarities of NW formation on a GaAs(100) surface.

The experiments were performed on a commercial MBE setup of the EP-1203 type. The substrates were (100)-oriented single crystal GaAs plates. The substrates were placed into a growth chamber of the MBE setup, cleaned from native oxide layers by treatment at 610°C in a flow of As$_4$, and coated with a ~250-nm-thick buffer layer of GaAs at 550°C. Then, the sample surface was coated with a ~1-nm-thick protective layer of arsenic in order to prevent the formation of a natural oxide layer during the transfer of samples from the MBE setup to a VUP-5 vacuum system (Elektron Company, Ukraine) for gold deposition. In this vacuum system, the samples were heated to $T \sim 260$–270°C so as to evaporate arsenic, cooled to $T \sim 110$–140°C, and coated with gold. The gold layer thickness had a preset value in the interval from 0.6 to 1.2 nm, which was checked by measuring the optical transmission with an accuracy no worse than $\Delta I/I \sim 0.1\%$. This error corresponds to a film thickness uncertainty of ~0.2 nm (in the region of small Au layer thicknesses). The patterns of reflection high-energy electron diffraction (RHEED) obtained from gold-coated samples showed evidence of an amorphous structure, which could be indicative both of the amorphous state of the gold film and of the presence of an amorphous oxide layer.

After gold deposition, the samples were returned to the growth chamber of the MBE system and heated to $T \sim 610$°C in order to remove the oxide layer from the substrate surface and to form Au droplets containing dissolved GaAs. Then, the sample temperature was
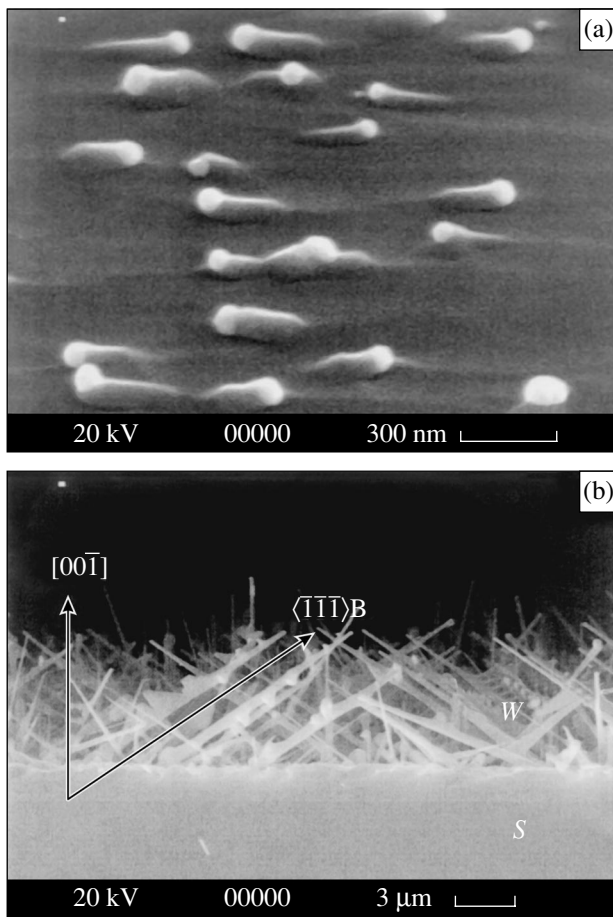
Fig. 1. Field-emission SEM images showing the surface morphology of samples after MBE growth of a GaAs layer with an effective thickness of (a) 500 nm (isometric projection) and (b) 1500 nm (cross section) on a Au–GaAs(100) surface (the samples are oriented along the (100) section; S and W are the substrate and whiskers, respectively).

reduced to 550°C and a GaAs layer was deposited, which corresponded to the stage of NW growth. The effective rate of GaAs deposition was 1 monolayer per second and the ratio of Ga and As_4 flow rates was such that the Ga/As flux density ratio was $J_{Ga}/J_{As} \sim 1$. The values of the effective thickness of deposited GaAs layers corresponds to the thickness of a layer formed during planar growth and may reflect the integral flow rate of the deposited material. Special tests showed that the planar growth rates on the (100) and $(\bar{1}\bar{1}\bar{1})B$ surfaces of GaAs were equal.

The process of NW formation was monitored *in situ* by measuring the RHEED patterns [15]. The RHEED data showed evidence of the epitaxial growth of NWs coherent with the substrate material. Analogous results were observed in other investigations of the NW growth [3–7].

The surface morphology of samples was studied in a CamScan S4-90FE scanning electron microscope

(SEM) with a field cathode, operating in the regime of secondary electron emission with a probing electron bean energy of 20 keV. The results of these investigations revealed two main types of the NW morphology as illustrated in Figs. 1a and 1b. The first type (Fig. 1a) corresponds to the formation of NW nuclei extended along the substrate surface in the $[1\bar{1}0]$ and $[\bar{1}10]$ directions. The characteristic longitudinal size of these nuclei is 200–300 nm and the transverse size is 50–150 nm. The ratio of the longitudinal to transverse size was approximately two. It should be noted that the transverse size of these NWs corresponds to that of Au–GaAs droplets. The surface number density of such NW nuclei was 5.3×10^8 cm^{-2}. The distribution of the Au–GaAs droplet size has a maximum in the region of 65 nm and the character of this distribution corresponds to the formation of droplets by mechanism of two-dimensional surface diffusion [16–18].

The second type of NW morphology (Fig. 1b) reflects the formation of intergrown NWs elongated in the $[1\bar{1}1]$ and $[\bar{1}11]$ directions and oriented in the $(1\bar{1}0)$ plane. The NWs also exhibited dendritic branching in the $\langle 111 \rangle B$ directions (Fig. 1b). The characteristic distance between branches was on the order of 2000 nm. Investigation of the morphology of intergrown NWs showed that they exhibit a (110) habit with a hexagonal cross section (Fig. 2a). Note that the NW tip surface also has a (110) faceting (Fig. 2b). As can be seen from Fig. 2, this tip surface carries a droplet of Au–GaAs melt. The characteristic dimensions of Au–GaAs droplets fall within 10–40 nm. The transverse size of NWs ranges from 80 to 200 nm. The NW length is on the order of 15000 nm, which is 10–20 times the effective thickness of deposited GaAs. The ratio of longitudinal and transverse dimensions of intergrown NWs can be on the order of 150 and above, while their surface number density reaches 3.5×10^7 cm^{-2}. It should be noted that the ratio of longitudinal and transverse dimensions of intergrown NWs varies in a nonmonotonic manner: for NWs with a transverse size below 200 nm, the longitudinal size increases; when the transverse exceeds a certain value of about 200 nm, the longitudinal size slightly decreases.

In addition to the NWs oriented in the (111)B direction, there is a certain fraction of NWs oriented in some other directions, usually low-index ones such as $\langle 100 \rangle$ and $\langle 112 \rangle$. The fraction of such NWs in their total amount is small. The NW structure (habit, tip shape) is analogous to that observed for NWs oriented in the $[\bar{1}\bar{1}\bar{1}]B$ direction upon a small change in the transverse size. In particular, the transverse size of NWs oriented in the $\langle 100 \rangle$ and $\langle 112 \rangle$ directions amounts to approximately 80–120 nm. The formation of NWs oriented in the directions other $[\bar{1}\bar{1}\bar{1}]B$ is probably related to the growth of extended defects emerging at the crystal surface.

The above results indicate that the formation of NWs in the course of MBE is significantly influenced by the crystallographic properties of the material. In this respect, the NWs grown by MBE substantially differ from those formed by ion etching [8–10]. Indeed, in the latter case, the filamentary elements of the surface morphology are oriented parallel to the direction of ion beam incidence and their characteristic dimensions depend on the exposure.

In the case of MBE growth of GaAs layers with an effective thickness of about 500 nm, only the structures with morphology of the first (nucleation) type are formed. When the effective GaAs layer thickness reaches 1500 nm, the samples predominantly exhibit morphology of the second (intergrowth) type. It should be noted that the growth rate of NWs of the second type is more than 15 times that of the epitaxial GaAs layers, which agrees with the model recently proposed in [19].

A comparison of the aforementioned morphological features is indicative of inhomogeneous character of the NW growth on a GaAs(100) surface. This process depends on the effective thickness of the deposited layer: the NW growth rate in the range of effective thicknesses below 500 nm is approximately equal to that of the planar epitaxial growth, while further increase in the effective thickness accelerates the NW growth by a factor of more than 15. It should be noted that the ratio of the growth rates of NWs (V_1) and planar crystals (V_2) was estimated as the ratio of changes in the characteristic NW size (ΔL_1) and the effective GaAs layer thickness (ΔD_2):

$$\frac{V_1}{V_2} = \frac{\Delta L_1}{\Delta D_2}.$$

It should also be noted that the region near the sample edge predominantly features the formation of NW nuclei. This character of the growth morphology can be explained by the influence of the temperature gradient developed in this region.

To summarize, we have demonstrated the possibility of growing oriented NWs on a GaAs(100) surface by means of MBE. It was established that the MBE growth of NWs exhibits two stages (initial and developed) and leads to the formation of NWs with the surface morphology of two types (nuclei and intergrown crystals). The stage of developed growth is characterized by the predominant formation of intergrown NWs oriented in the $\langle 111 \rangle$B direction, having ($1\bar{1}0$) habit (including the NW tip surface) and hexagonal cross sections with a transverse size within 50–300 nm. It was found that the transverse size of a hexagonal NW may significantly differ from that of a Au–GaAs melt droplet. The ratio of longitudinal and transverse dimensions of intergrown NWs can be on the order of 150 and above. When the transverse size of NWs exceeds a certain value (about 200 nm), the crystal length exhibits a slight decrease. The NW growth on a GaAs(100) surface exhibits inho-
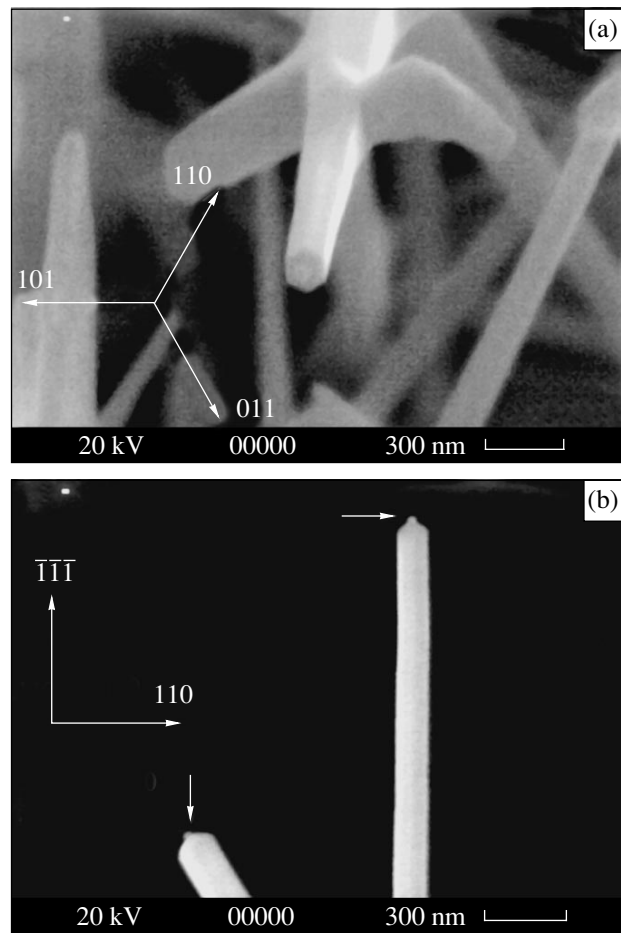

Fig. 2. SEM images of (a) the NW edge and (b) the NW tip (arrows indicate the Au–GaAs droplets).

mogeneous character, being dependent on the catalyst droplet size, effective thickness of the deposited GaAs layer, and the growth temperature.

REFERENCES

1. G. W. Sears, Acta Metall. **1**, 457 (1953).

2. R. S. Wagner and W. C. Ellis, Appl. Phys. Lett. **4** (5), 89 (1964).

3. E. I. Givargizov, *Vapor Phase Growth of Filamentary and Platelike Crystals* (Nauka, Moscow, 1977) [in Russian].

4. E. I. Givargizov, J. Cryst. Growth **31**, 20 (1975).

5. R. Notzel, J. Temmyo, T. Tamamura, *et al.*, Nature **369** (5), 131 (1994).

6. W. N. Borle, J. Appl. Phys. **41**, 3184 (1970).

7. E. I. Givargizov, Dokl. Akad. Nauk SSSR **222**, 319 (1975) [Sov. Phys. Dokl. **20**, 308 (1975)].

8. O. Wada, J. Phys. D **17**, 2429 (1984).

9. J. B. Malherbe, CRC Crit. Rev. Solid State Mater. Sci. **19** (3), 119 (1994).

10. I. P. Soshnikov, A. V. Lunev, M. E. Gaevski, *et al.*, Proc. SPIE **3048**, 404 (1997).

11. V. V. Mamutin, Pis'ma Zh. Tekh. Fiz. **25** (18), 55 (1999) [Tech. Phys. Lett. **25**, 741 (1999)].

12. Y. Cui, L. J. Lauhon, M. S. Gudiksen, *et al.*, Appl. Phys. Lett. **78**, 2214 (2001).

13. B. J. Ohlsson, M. T. Bjoerk, M. H. Magnusson, *et al.*, Appl. Phys. Lett. **79**, 3335 (2001).

14. A. A. Tonkikh, G. E. Cirlin, Yu. B. Samsonenko, *et al.*, Fiz. Tekh. Poluprovodn. (St. Petersburg) **38**, 1256 (2004) [Semiconductors **38**, 1217 (2004)].

15. G. M. Gur'yanov, V. N. Demidov, N. P. Korneeva, *et al.*, Zh. Tekh. Fiz. **67** (8), 111 (1997) [Tech. Phys. **42**, 956 (1997)].

16. Ya. E. Geguzin and Yu. S. Kaganovskiĭ, Usp. Fiz. Nauk **125**, 489 (1978) [Sov. Phys. Usp. **21**, 611 (1978)].

17. I. M. Lifshits and V. V. Slezov, Zh. Éksp. Teor. Fiz. **35**, 479 (1959) [Sov. Phys. JETP **8**, 331 (1959)].

18. S. A. Kukushkin and V. V. Slezov, *Disperse Systems on Solid Surfaces (Evolutionary Approach)* (Nauka, St. Petersburg, 1996).

19. V. G. Dubrovskiĭ, N. V. Sibirev, and G. E. Cirlin, Pis'ma Zh. Tekh. Fiz. **30** (16), 41 (2004) [Tech. Phys. Lett. **30**, 682 (2004)].

Translated by P. Pozdeev

Magnetoelectric Response of a Multilayer Ferrite–Piezoelectric Structure to Magnetic Field Pulses

A. Y. Ostashchenko[a], K. E. Kamentsev[a], Y. K. Fetisov[a],*, and G. Srinivasan[b]

[a] *Moscow Institute of Radio Engineering, Electronics, and Automation (Technical University),*
Moscow, 117454 Russia
[b] *Physics Department, Oakland University, Rochester, Michigan 48309, USA*
* e-mail: fetisov@mirea.ru
Received April 2, 2004

Abstract—Magnetoelectric (ME) response of a multilayer ferrite–piezoelectric structure to short magnetic field pulses has been measured. The frequency spectrum of the ME coefficient α_E of the structure in the range from several dozen hertz to 1 MHz has been determined by Fourier analysis of the ME response signal. The α_E value shows a general slow monotonic decrease with increasing frequency and exhibits a 7- to 30-fold resonance growth at certain frequencies, which is related to the excitation of intrinsic acoustic oscillations of the multilayer structure. In the low-frequency range, the ME coefficient has a maximum in the region of 1 kHz due to relaxation processes in the piezoelectric and ferrite layers. © *2004 MAIK "Nauka/Interperiodica".*

Multilayer planar structures consisting of ferrite and piezoelectric layers exhibit anomalously large magnetoelectric (ME) response, which makes such composites promising materials for magnetic field sensors and transducers [1–3]. The ME effect in these structures is due to a certain combination of properties of the component layers [4]. When a composite structure is magnetized by external magnetic field H, ferrite layers strained as a result of magnetostriction produce deformation of the mechanically coupled piezoelectric layers. This leads to a change in polarization of these layers and induces electric charge at the piezoelectric–ferrite interfaces, which results in the appearance of voltage U between surfaces of the structure. The effect is characterized by the ME coefficient $\alpha_E = U/Hd$, where d is the total thickness of piezoelectric layers in the structure.

The ME effect in multilayer structures has been previously studied by means of harmonic modulation of the field [1, 5], whereby a structure was placed between poles of a magnet creating a constant field H_0, an alternating field of small amplitude h and frequency f (variable from 0.1 to 10 kHz) was generated by modulating coils, and the response voltage U was measured at the modulation frequency. Using this technique, it is difficult to study the frequency characteristic of the ME effect in a broader frequency range, because an increase in the frequency is accompanied by a sharp drop (caused by the inductance of modulating coils) in amplitude of the modulation field and, hence, of the ME response signal.

In this study, we have measured for the first time the ME response of a multilayer structure to short magnetic field pulses. The results show that this pulse technique provides information about the frequency characteristic of the ME effect in multilayer structures in the range from several dozen hertz up to about 1 MHz.

The ME effect was studied on a multilayer planar structure comprising alternating layers of nickel ferrite $Ni_{0.7}Zn_{0.3}Fe_2O_4$ (NF) and lead zirconate titanate $PbZr_{0.52}Ti_{0.48}O_3$ (PZT) prepared using thick-film ceramic technology [1]. The structure consisted of 16 NF and 15 PZT layers, each 18 μm thick, and had the lateral dimensions 6.2×8.9 mm. The external surfaces were covered with a conducting silver paste.

The structure was polarized in external electric field with a strength of 30 kV/cm applied perpendicularly to the sample plane. Then, the structure was placed between poles of a magnet creating a constant field $H_0 = 0$–3 kOe tangent to the plane. Simultaneously, a pulsed magnetic field $h(t)$ was applied parallel to the constant field. The magnetic field pulses were generated by a coil wound on the sample. The coil was 8 mm in diameter, 10 mm long, and contained 10 turns of a wire with a diameter of 0.5 mm. The pulses were excited by rectangular current pulses with an amplitude of up to 30 A, a duration of 1–100 μs, a front width below 0.2 μs, and a repetition rate of 50 ms. At the maximum current amplitude, the amplitude of the magnetic pulse $h(t)$ in the sample was ~240 Oe. The ME response voltage $U(t)$ between metallized surfaces of the sample structure was measured with the aid of a digital oscillograph.

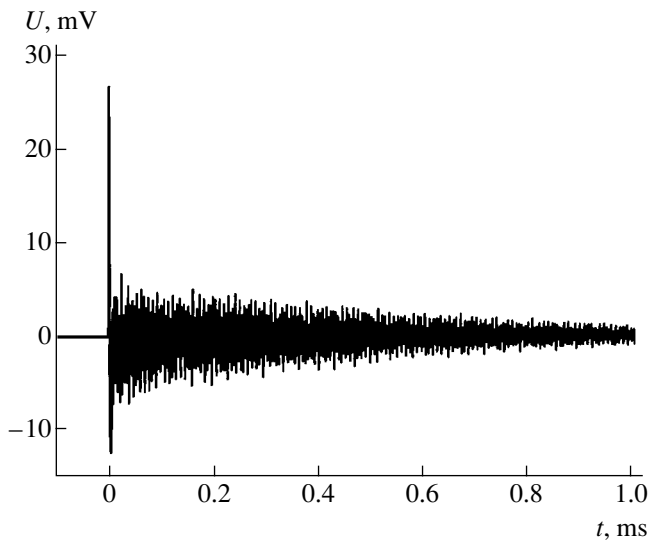**Fig. 1.** The typical ME response of a multilayer ferrite–piezoelectric structure to a 1-μs magnetic field pulse.
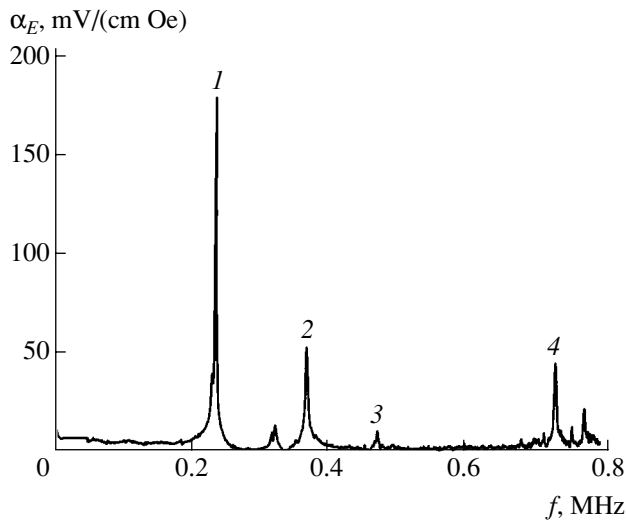

Fig. 2. The frequency dependence of the ME coefficient α_E of a multilayer ferrite–piezoelectric structure in a broad frequency range. The peaks correspond to the frequencies of intrinsic acoustic oscillations of the sample, representing the fundamental modes f_1 (*1*) and f_2 (*2*) and their second harmonics $2f_1$ (*3*) and $2f_2$ (*4*).

Figure 1 shows the typical oscillogram of an ME response signal measured upon application of 1-μs magnetic field pulse with an amplitude of $h \sim 240$ Oe. The measurement was performed in a constant field of $H_0 = 120$ Oe, for which the ME response was maximum. The narrow peak of positive polarity observed in the vicinity of $t = 0$ corresponds to the signal of direct electromagnetic induction and repeats the shape of the magnetic field pulse. When the field pulse terminates, the system features exponentially decaying oscillations of the ME voltage. The period of these oscillations is $T \approx 4.35$ μs and the characteristic amplitude decay time

is $\tau \approx 262$ μs, which corresponds to a resonator with the quality factor $Q = \pi\tau T \approx 189$. Figure 1 also reveals an additional modulation of the amplitude of decaying oscillations, which is indicative of the presence of beats at several frequencies in the resonator.

A more illustrative and complete notion of the frequency characteristic of the ME effect in a multilayer structure is provided by the Fourier analysis of the observed time series. Figure 2 shows a plot of the ME coefficient α_E versus frequency f for the structure studied. This plot is obtained by dividing the Fourier spectrum $U(f)$ of the signal by the Fourier spectrum $h(f)$ of the magnetic field pulse and the total thickness $d = 270$ μm of PZT layers in the sample structure. Use of a rather short field pulse (~1 μs) with the first zero in the vicinity of 1 MHz ensures the absence of nonphysical peaks in $\alpha_E(f)$ related to the division by a small quantity.

An analysis of the obtained frequency spectrum $\alpha_E(f)$ of the ME coefficient leads to the following main conclusions.

(i) For the multilayer NF–PZT structure studied, the α_E value weakly depends on the frequency and monotonically decreases from ~7 to ~4 mV/(Oe cm) as the frequency increases from several kilohertz to ~200 kHz.

(ii) There is a sharp (7- to 30-fold) increase in the α_E value at some frequencies. This is probably related to the excitation of intrinsic acoustic oscillations of the multilayer structure, leading to a resonance growth in the amplitude of deformation and, hence, in the ME signal amplitude [6]. The main resonances with maximum amplitudes correspond to $f_1 = 234.7$ kHz and $f_2 = 368.6$ kHz (Fig. 2). There are two smaller resonances at the second harmonics, $2f_1 \approx f_3 = 473.0$ kHz and $2f_2 \approx f_4 = 733.6$ kHz, and several weaker resonances at intermediate frequencies. The calculations [6] performed using the acoustical parameters of NF and PZT showed that oscillations corresponding to the standing waves in the plane of the structure fall precisely within the frequency range 200–400 kHz. In our case, the resonances at f_1 and f_2 correspond to the fundamental modes excited along and across the sample. This is confirmed by the ratio of frequencies of the main resonance peaks $f_1/f_2 = 0.64$, which is close to the ratio of width and length (~0.69) in the structure studied. The measured Q of the main resonances at f_1 and f_2 were $Q_1 = 186$ and $Q_2 = 112$, which approximately coincide with the values calculated using the characteristic time of decay of the ME signal. The beats between the resonance frequencies of the system lead to additional modulation of the ME response amplitude observed in Fig. 1. It should be noted that a rather large value of the α_E value at the second harmonic frequencies of the fundamental acoustic modes is evidence of a nonlinear character of the ME effect in the multilayer structure studied.

(iii) There is a broad local maximum in $\alpha_E(f)$ in the vicinity of 1 kHz, which is clearly pronounced when the spectrum is plotted on a greater frequency scale
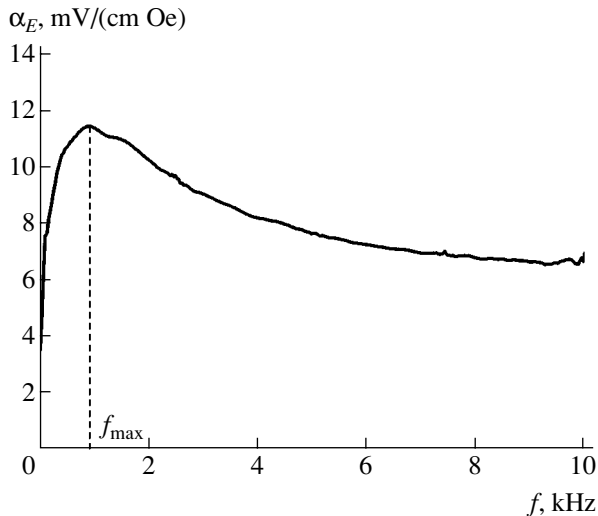
Fig. 3. The frequency dependence of the ME coefficient α_E of a multilayer ferrite–piezoelectric structure in the region of low frequencies.

field pulses. The ME coefficient α_E of the structure monotonically decreases with increasing frequency, exhibits a sharp increase at the frequencies of acoustic resonances of the sample, and has a local maximum in the low-frequency region.

(Fig. 3). The ME coefficient at $f_{max} = 0.9$ kHz reaches 11.4 mV/(Oe cm). An analogous maximum was observed in the frequency characteristics of the ME effect in the same structure studied by the harmonic field modulation technique [5]. A drop of the ME coefficient at frequencies below f_{max} is related to compensation of the induced charges caused by the finite conductivity of piezoelectric layers [7]. A decrease in $\alpha_E(f)$ at the frequencies above f_{max} is probably caused by relaxation processes in the ferrite layers.

Thus, we have studied the ME response of a multilayer ferrite–piezoelectric structure to short magnetic

REFERENCES

1. G. Srinivasan, E. T. Rasmussen, J. Gallegos, *et al.*, Phys. Rev. B **64**, 214408 (2001).

2. J. Ryu, S. Priya, K. Uchino, *et al.*, J. Electroceram. **8**, 107 (2002).

3. G. Srinivasan, E. T. Rasmussen, A. A. Bush, *et al.*, Appl. Phys. A **76**, 1 (2003).

4. J. van Suchtelen, Philips Res. Rep. **27**, 28 (1972).

5. A. Y. Ostashchenko, K. E. Kamentsev, Yu. K. Fetisov, and G. Srinivasan, in *Proceedings of the MEPI Scientific Conference* (MEPI, Moscow, 2003), Vol. 4, pp. 168–169.

6. D. A. Filippov, M. A. Bichurin, V. M. Petrov, *et al.*, Pis'ma Zh. Tekh. Fiz. **30** (1), 15 (2004) [Tech. Phys. Lett. **30**, 6 (2004)].

7. V. M. Petrov, M. I. Bichurin, and G. Srinivasan, Pis'ma Zh. Tekh. Fiz. **30** (8), 81 (2004) [Tech. Phys. Lett. **30**, 341 (2004)].

Translated by P. Pozdeev

Effect of the Initiating Pulse Energy on the Kinetics of Preexplosion Processes in Silver Azide

É. D. Aluker, A. G. Krechetov, A. Yu. Mitrofanov, and A. S. Pashpekin

Kemerovo State University, Kemerovo, Russia
e-mail: lira@kemsu.ru
Received March 29, 2004

Abstract—We have experimentally studied the dependence of the kinetics of preexplosion conductivity (σ) and luminescence intensity (I) on the energy of the initiating laser pulse. The rates of the σ and I buildup in the initial stage of the induction period increase with the laser pulse energy, while the values of preexplosion conductivity and luminescence intensity on the plateau are independent of this energy. © *2004 MAIK "Nauka/Interperiodica".*

Previously [1, 2], we studied the preexplosion phenomena (conductivity and luminescence) observed in the initial stages of the explosive decomposition of heavy metal azides, between the initiating pulse and the onset of sample destruction (i.e., during the so-called induction period). It was found that the kinetics of these processes reflects the kinetics of a chain reaction of the explosive decomposition [3].

Recently [4], a model of the initiation process has been proposed which relates the reaction onset to recharge of the trapping centers, providing an increase in the cross section of hole trapping on these centers and in the reaction rate. This model predicts an interesting kinetic effect [4], whereby the rate of the preexplosion conductivity (σ) and luminescence intensity (I) buildup in the initial stage must increase with the energy density in the initiating pulse. Then, σ and I must attain a plateau, where these values are independent of the initiating pulse energy.

Experimental observation of this nontrivial behavior would provide considerable evidence in favor of the proposed model [4]. This study was aimed at verification of the peculiarities in the kinetics of preexplosion processes predicted by the theory.

The experiments were performed with silver azide whiskers having the characteristic dimensions $100 \times 100 \times 1000$ μm. The explosion decomposition was initiated by picosecond pulses of a YAG:Nd^{3+} laser ($\lambda = 1064$ nm, $t \approx 30$ ps, $H = 15$–300 mJ/cm^2).

The signals due to preexplosion conductivity and photoluminescence were measured directly by oscillographs. Each output signal was fed via a matched T junction to the inputs of two high-speed S7-19 oscillographs. In one of these, the input signal was attenuated 1 : 10 and used for monitoring the whole induction period, including the stage where the response signal amplitude attained a plateau. The other oscillograph was used to monitor the kinetics of initial stages of the

preexplosion processes. This procedure allowed the dynamic range of measurements to be expanded by two orders of magnitude. The images from both oscillographs were recorded (by means of a videocamera and a video interface) into computer memory and stored in the form of graphical files. Subsequent processing of these files gave kinetic curves of the process.

The optical emission was detected by photomultipliers of the ELUF type, while the conductivity signal was detected using specially designed measuring cells. The time resolution was ~1 ns for the photoluminescence signal channel and ~0.3 ns for the conductivity signal channel. The time was measured from marker pulses generated in the response signal detectors upon arrival of the initiating laser pulse. The results of repeated
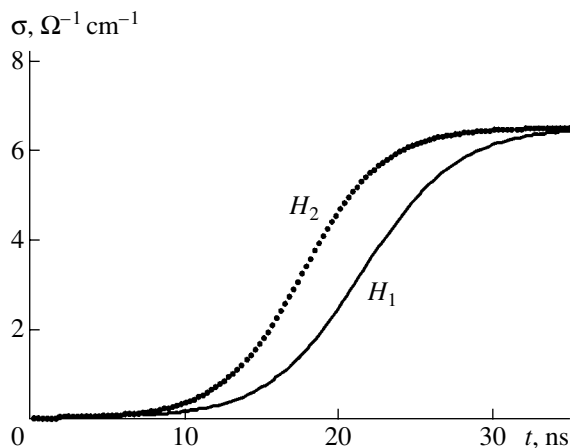

Fig. 1. Typical kinetics of the preexplosive conductivity in silver azide whiskers initiated by picosecond laser pulses with energy densities $H_1 \approx 100$ mJ/cm^2 and $H_2 \approx 250$ mJ/cm^2. The increase in H results in a higher σ buildup rate in the initial stage, while σ on the plateau is independent of H.
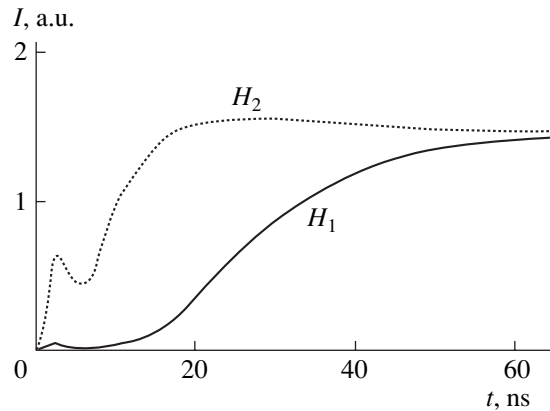
Fig. 2. Typical kinetics of the preexplosive luminescence from silver azide whiskers initiated by picosecond laser pulses with energy densities $H_1 \approx 15$ mJ/cm^2 and $H_2 \approx 100$ mJ/cm^2.

measurements showed that the time scale was accurate to within ±2 ns. The experimental techniques are described in mode detail elsewhere [3]. The experiments were performed on silver azide whiskers synthesized in one batch, with ten repetitions for each value of the initiating pulse energy density.

Figures 1 and 2 show the typical kinetic curves. As can be seen from these data, both the preexplosion conductivity (Fig. 1) and the preexplosion photoluminescence (Fig. 2) exhibit qualitatively similar behavior depending on the laser pulse energy. In the initial stages, an increase in the laser pulse energy density leads to a higher buildup rate of both the conductivity (Fig. 1) and the photoluminescence (Fig. 2) signals. At the late stages, both signal kinetics exhibit a plateau where the signals are independent of the laser pulse energy (Figs. 1, 2).

Thus, the observed results confirm the kinetic effects predicted by the model [4] and, hence, can be considered as considerable evidence in favor of this theory.

REFERENCES

1. B. P. Aduev, É. D. Aluker, G. M. Belokurov, and A. G. Krechetov, Pis'ma Zh. Éksp. Teor. Fiz. **62**, 203 (1995) [JETP Lett. **62**, 215 (1995)].

2. B. P. Aduev, É. D. Aluker, and A. G. Krechetov, Pis'ma Zh. Tekh. Fiz. **22** (6), 24 (1996) [Tech. Phys. Lett. **22**, 236 (1996)].

3. B. P. Aduev, É. D. Aluker, G. M. Belokurov, *et al.*, Zh. Éksp. Teor. Fiz. **116**, 1676 (1999) [JETP **89**, 906 (1999)].

4. B. P. Aduev, É. D. Aluker, and A. G. Krechetov, Fiz. Goreniya Vzryva, No. 2, 94 (2004).

Translated by P. Pozdeev

Peculiarities of the Kinetics of Explosive Decomposition of Silver Azide Initiated by a Pulsed Electron Beam

B. P. Aduev, G. M. Belokurov, S. S. Grechin, and E. V. Tupitsin

Kemerovo State University, Kemerovo, Russia
Institute of Solid State Chemistry and Mechanochemistry (Kemerovo Department), Siberian Division,
Russian Academy of Sciences, Kemerovo, Russia
e-mail: lira@kemsu.ru; filial@kemnet.ru
Received April 2, 2004

Abstract—We have studied the spectrum and kinetics of optical emission accompanying the explosive decomposition of silver azide crystals initiated by a nanosecond electron beam (0.25 MeV, 20 ns, 0.1–2 kA/cm^2). The emission kinetics reveals a component observed during the initiating pulse action, whose spectrum coincides with the spectrum of preexplosive luminescence observed in the subsequent stages of the initiation reaction. It is shown that the explosive decomposition reaction is initiated directly during the electron beam action and has a nonmonotonic kinetics. © 2004 MAIK "Nauka/Interperiodica".

Previously [1–3], it was demonstrated that the reaction of explosive decomposition in heavy metal azides initiated by nanosecond pulsed electron beams or picosecond laser pulses develops in the initial stage according to the chain mechanism. The development of this process is accompanied by optical emission characterized by a continuous spectrum, which does not obey the Planck formula and is referred to as the preexplosive luminescence [1–3]. In later stages, the emission has a linear spectrum related to the products of explosive decomposition [2, 3].

The kinetics of preexplosive luminescence reflects the kinetics of the explosive decomposition reaction and, hence, can be used for monitoring the initiation process. A model describing preexplosive optical emission and the chain reaction of decomposition was developed in [2]. A refined divacancy model of this reaction was recently proposed in [4].

The experiments described in [1–3] were performed using pulsed electron beams with a current density of ~200 A/cm^2. In such cases, the intensity of emission accompanying the initiation reaction increases within a time interval of ~0.5 μs and is virtually absent during the excitation pulse at $T = 300$ K [3]. However, subsequent experiments showed that this behavior changed as the electron beam current density was increased: there appeared an emission component observed immediately during the initiating beam pulse, followed by the continuous preexplosive luminescence and the linear emission from decomposition products.

This study was aimed at elucidating the nature of the first emission component.

The experiments were performed with $3 \times 1 \times 1$-mm silver azide single crystals. The samples were initiated by 20-ns pulses of a 0.25-MeV electron beam with a current density varied from 200 to 2000 A/cm^2. The samples were fixed on a massive metal substrate and placed into a vacuum chamber of the electron accelerator with a residual gas pressure of 10^{-3} Pa and a temperature of 300 K.

The emission from samples was monitored by a method described in detail elsewhere [3], using a setup based on a spectrograph and a streak chamber. Using this method, it is possible to perform spectral measurements during explosion of a single sample at a time resolution determined by the initiating pulse duration. The spectra can be measured in a wavelength interval from 550 to 1000 nm.

For initiating beam current densities above 1000 A/cm^2, the emission kinetics clearly revealed two components with continuous emission spectra, followed by a component possessing a linear spectrum. The intensity of the first component increased with the electron beam current density. Figure 1 shows the kinetics of explosive luminescence from a silver azide crystal measured at $\lambda = 770$ nm (coinciding with one line in the spectrum of decomposition products). Here, the leading front width of the first peak corresponds to the electron beam pulse duration. The amplitude, duration, and magnitude of the subsequent decay are determined by the excitation current density and individual features of each sample.

Figure 2 shows the continuous luminescence spectra of the first two kinetic components (with allowance for the spectral sensitivity of the measuring setup, normalized to the maximum intensity). The spectra virtually coincide with each other and with the spectrum of preexplosion luminescence observed previously [2] for significantly lower current densities of the exciting electron beam. The latter fact leads to the conclusion
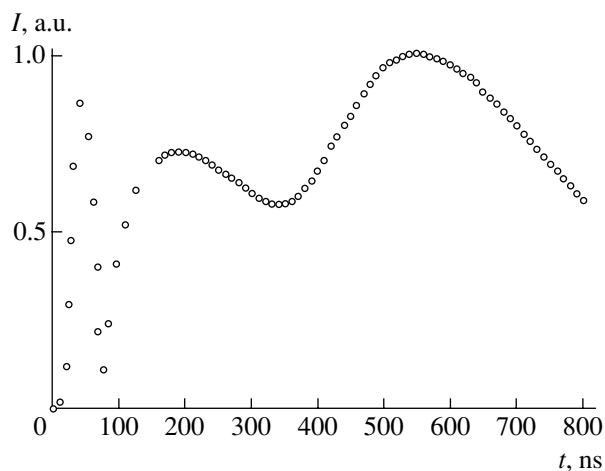
Fig. 1. Typical kinetics of the explosive luminescence at $\lambda = 770$ nm from silver azide single crystals initiated by an electron beam with a current density of 2000 A/cm^2 at $T = 300$ K. The first two components have continuous spectra, while the third component exhibits a line spectrum.
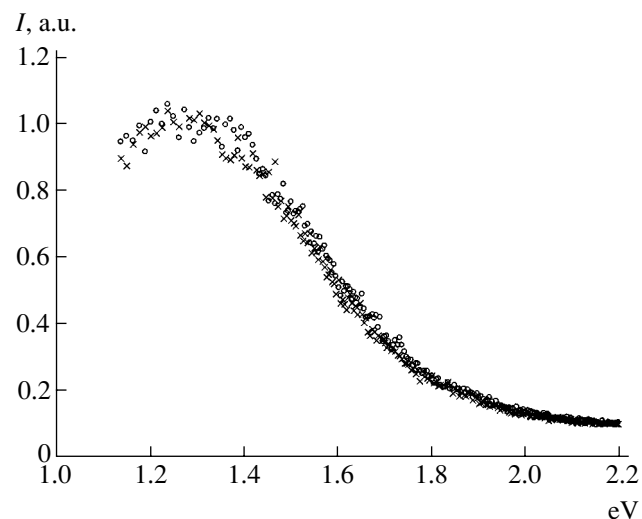

Fig. 2. The spectra of explosive luminescence from silver azide single crystals measured at various moments of time after the initiation pulse front (ns): (∘) 20 (first peak in Fig. 1); (×) 190 ns (second peak in Fig. 1).

that both emission components have the same nature related to the reaction of explosive decomposition of silver azide.

An analysis of the observed spectral and kinetic characteristics of the explosive emission, in combination with our previous results [1–4], leads to the following conclusions. The reaction of explosive decomposition is initiated immediately during the initiating electron beam pulse (Fig. 1, first luminescence peak). The following decay is related to the interplay of processes including the filling of traps and recombination centers and the multiplication of active species (holes). The kinetics of reaction in the next stage (Fig. 2, second luminescence peak) is described within the framework of the model proposed in [4].

It should also be noted that the results presented above do not conform to the concept of a thermal mechanism of development of the explosive decomposition of heavy metal azides.

REFERENCES

1. B. P. Aduev, É. D. Aluker, and A. G. Krechetov, Pis'ma Zh. Tekh. Fiz. **22** (6), 24 (1996) [Tech. Phys. Lett. **22**, 236 (1996)].

2. B. P. Aduev, É. D. Aluker, G. M. Belokurov, *et al.*, Zh. Éksp. Teor. Fiz. **116**, 1676 (1999) [JETP **89**, 906 (1999)].

3. B. P. Aduev, É. D. Aluker, and G. M. Belokurov, *Preexplosion Phenomena in Azides of Heavy Metals* (Khimmash, Moscow, 2002) [in Russian].

4. B. P. Aduev, É. D. Aluker, and A. G. Krechetov, Fiz. Goreniya Vzryva, No. 2, 94 (2004).

Translated by P. Pozdeev

Obtaining a Dispersed Liquid–Gas Mixture Using a Piston Machine: Method and Possible Applications

Yu. V. Alekhanov, A. E. Levushov, A. A. Logvinov, S. A. Lomtev, and E. E. Meshkov

Institute of Experimental Physics, Russian Federal Nuclear Center, Sarov, Russia
Sarov Physicotechnical Institute, Sarov, Russia
e-mail: root@gdd.vniief.ru; meshkov@sarfti.sarov.ru
Received April 5, 2004

Abstract—Experiments confirm the possibility of obtaining a dispersed liquid–gas mixture with the aid of a piston machine. The mixture is formed as a result of the Rayleigh–Taylor instability development and the turbulent mixing in a very thin layer of a liquid at the end of a piston moving with deceleration. The possibility of using this phenomenon for (i) obtaining dispersed water–air mixtures for extinguishing fires and (ii) preparing fuel–air mixtures in internal combustion engines is discussed. © *2004 MAIK "Nauka/Interperiodica".*

Introduction. The motion of a piston in the piston machine [1] is described by the relations $x = r\cos\gamma t + \text{const}$, $v = -r\gamma\sin\gamma t$, and $a = -r\gamma^2\cos\gamma t$, where x is the path traveled by the piston, r is the pin radius of the crankshaft, γ is the angular speed of the crankshaft (the angle measured from the top dead center), and v and a are the linear velocity and acceleration of the piston, respectively. In the interval of crankshaft angles $\pi/2 < \gamma t < 3\pi/2$, the accelerated piston exhibits additional artificial gravity and a small amount of liquid occurring at the flat piston end spreads on this surface to form a thin layer. In the interval of angles $3\pi/2 < \gamma t < 2\pi$, the piston moves with deceleration and the boundary between the liquid layer on the piston surface and the gas compressed by the piston occurs in an unstable state. Here, the Rayleigh–Taylor instability [2, 3] is developed and a zone of turbulent mixing is formed [1].

We have developed a method for the investigation of this process and performed experiments which confirmed the possibility of obtaining a dispersed liquid–gas mixture with the aid of a piston machine as proposed in [1].

Previously [4], the development of a zone of turbulent mixing at the boundary of a thin liquid layer accelerated by a compressed gas was experimentally studied in the "compressed gas–liquid layer–compressed gas–hard wall" geometry. It would also be important to study the development of the Rayleigh–Taylor instability in a very thin liquid layer at a hard wall, that is, in the "hard wall–liquid layer–compressed gas–hard wall" geometry, which is of interest for both basic knowledge and applications. Below, we describe the results of such experiments.

Experimental. The experiments were performed using a scheme of the "hard wall–compressed gas (driver)–piston (with a thin liquid layer)–compressed gas–hard wall" type. The piston (20.5-mm-thick caprolon) moved in a cylindrical channel of constant cross section with a diameter of 50 mm. Initially, the piston moves with acceleration under the action of compressed gas (the products of detonation of an acetylene–oxygen mixture at a pressure of ~1 MPa) and then it is decelerated by increasing pressure of a compressed gas (air at the initial atmospheric pressure). This scheme qualitatively reproduces the dynamics observed in the piston machine. The perimeter of the upper piston surface had a circular barrier with a height of 0.4 mm and a width of ~20 mm, so that a ~0.4-mm-deep well with a diameter of 10 mm was at the center, in which a drop of water (~35 mg) was placed.

The explosive gas mixture in the chamber was initiated by electric spark discharge. The acceleration and deceleration of the piston were monitored by a high-speed camera of the SFR type with pulsed illumination from an IFK-120 lamp. The light passed through a transparent wall at the end of the acceleration channel and illuminated the zone of turbulent mixing.

Results. Figure 1 shows a photochronogram illustrating the acceleration and deceleration of the piston. In the initial stage ($t < 1.4$ ms), the piston moves with acceleration and the water–gas interface is stable. Water (initially, in the form of a drop) exhibits oscillations on the piston surface. In the stage of deceleration of the piston ($t > 1.4$ ms), photographs reveal rapid growth of the zone of turbulent mixing, which arises almost simultaneously over the entire width of the liquid layer. This zone is visualized due to the light scattering ion water. After impact on the channel end ($t = 2.29$ and 2.45 ms) the cloud of dispersed water exhibits flattening and spreading. If water initially covered the whole piston surface, the entire channel volume would be filled with dispersed water–air mixture.
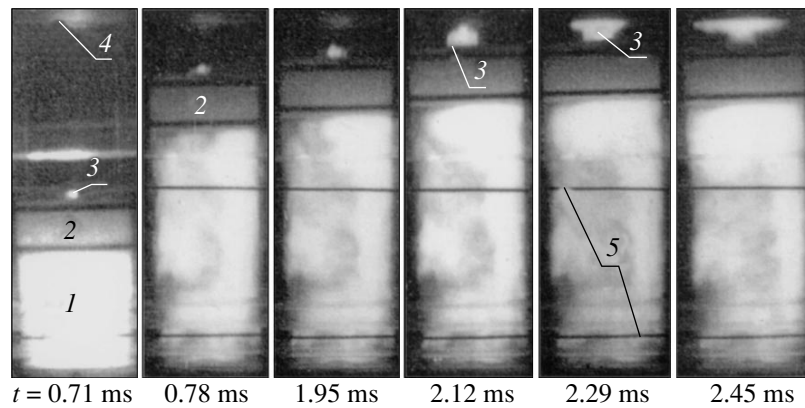
Fig. 1. The photochronogram of an experiment in a cylindrical channel (initial height $l = 22$ mm; length $L = 74.5$ mm) with acetylene–oxygen explosive gas mixture: (*1*) optical emission from products of the gas mixture detonation; (*2*) piston; (*3*) water layer (after the onset of deceleration, the zone of turbulent mixing of water and air); (*4*) end of the accelerating channel; (*5*) reference marks. The time is counted from the moment of initiation of the explosive gas mixture.

Figure 2 shows plots of the coordinate X versus time t for the upper surfaces of the piston and the zone of turbulent mixing. Figure 3 shows variation of the width of the zone of turbulent mixing with the time measured from the moment of detonation of the explosive gas mixture.

The experimental data were processed by approximating the $X(t)$ curve of the upper piston surface using a fourth-order polynomial and by differentiating this curve. This treatment provided information about the scale of acceleration ($a \sim 2 \times 10^4$–10^5 m/s^2) and velocity ($v \sim 30$–40 m/s) reached in our experiments. The compression of the mixture of air with dispersed liquid in the channel did not exceed $\sigma_1 \approx 7.5$ during the period of time from the onset of motion to the moment of maxi-

mum compression, and $\sigma_2 \approx 3$ during the period of time from the onset of piston deceleration to the moment of maximum compression.

Discussion. The results of our experiments confirmed the possibility of obtaining a dispersed liquid–gas mixture with the aid of a piston machine. This method can be used, in particular, for (i) continuous preparation of dispersed water-air dispersed water–air mixtures in large volumes (for example, for extinguishing fires and localization of armful aerosols) and (ii) preparation of dispersed fuel–air mixtures in diesel engines (without using fuel injectors).

The process of extinguishing fires by dispersed (or sprayed) water with a droplet size below 100 μm is much more effective than the use of a compact stream [5]. Cre-
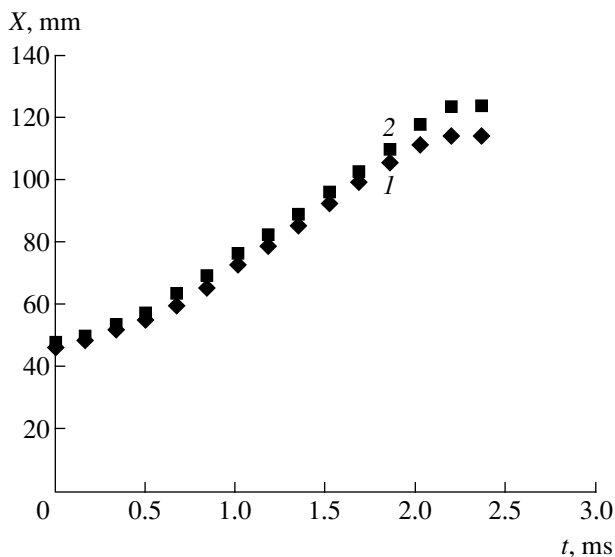

Fig. 2. Plots of the coordinate X versus time t for (*1*) the upper surface of the piston and (*2*) the upper boundary of the zone of turbulent mixing.
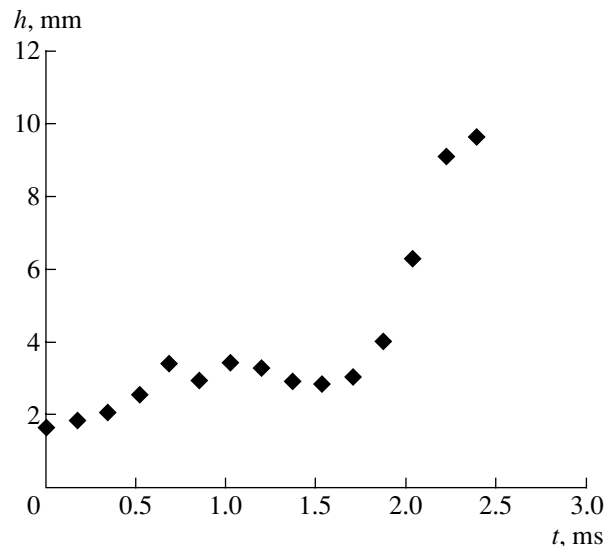

Fig. 3. Time variation of the width of the zone of turbulent mixing. In the stage of piston acceleration ($t \leq 1.4$ ms), the visible thickness of the water layer is determined by oscillations of the water surface and is slightly greater than the average layer thickness (~ 0.4 mm).

ation of a water aerosol cloud ensures the use of water with a 100% efficiency (for the traditional method of extinguishing fires, this value is on the order of 5%) [6].

Short-lived dispersed water aerosols precipitating onto the ground surface can also be effectively used for absorbing aerosols, harmful gases, dust, etc., formed in clouds upon explosions. Mixing with dispersed water–air mixture will significantly restrict the area of contamination around the center of explosion [7, 8]. Liquid dispersion technologies are also widely used in some other fields, such as spray drying, application of coatings, fog sprinkling, and dust trapping.

The proposed method [1] can also be used for the continuous preparation of large volumes of dispersed water–air mixtures. The crankshaft of the piston machine can be driven by any motor (electric, internal combustion, etc.). A piston machine intended for this purpose must only be equipped with a device injecting the required amount of water at the stage when artificial gravity is developed on the piston surface. Each cylinder of the piston machine must also be provided with a valve opening at a time close to the moment of maximum compression. The dispersed water–air mixture is driven to the output by its own pressure and then distributed in desired directions.

The results of our experiments also confirmed the possibility of using the proposed method [1] for preparing fuel–air mixtures in internal combustion engines. For example, consider a situation when the piston machine is an internal combustion engine with a crankshaft pin radius of $r = 47$ mm and angular speed of $\gamma = 800$–4200 rpm. The maximum piston velocity is $v = 3.9$–20.7 m/s and the acceleration $a = 330$–9100 m/s^2 (depending on the crankshaft angular speed). These values of the velocity and acceleration are close to those used in our experiments.

REFERENCES

1. E. E. Meshkov and N. V. Nevmerzhitskiĭ, Patent Appl. No. 2 001 123 009, Russia (27 June 2003); Byull. Izobret., No. 18, Part. 1, p. 90.
2. Lord Rayleigh, Proc. London Math. Soc. **14**, 170 (1883).
3. G. I. Taylor, Proc. R. Soc. London, Ser. A **201**, 192 (1950).
4. E. E. Meshkov and N. V. Nevmerzhitskiĭ, Pis'ma Zh. Tekh. Fiz. **28** (8), 34 (2002) [Tech. Phys. Lett. **28**, 323 (2002)].
5. Ya. S. Povzik, *Fire Tactics* (Spetstekhnika, Moscow, 1999) [in Russian], p. 39.
6. A. Ya. Korol'chenko, Pozharovzryvobezopasnost, No. 2, 3 (2001).
7. G. M. Korovchenko, *Blaster–Expert* (Nedra, Moscow, 1972), pp. 175–177 [in Russian].
8. J. H. Parkes and S. H. Salter, GB Patent No. 2,294,105 (1996).

Translated by P. Pozdeev

Synchronization of Spectral Components
of Coupled Chaotic Oscillators

A. A. Koronovskiĭ*, O. I. Moskalenko, and A. E. Hramov**

State Scientific Center "College," Saratov State University, Saratov, Russia
*e-mail: * alkor@cas.ssu.runnet.ru; ** aeh@cas.ssu.runnet.ru*
Received March 24, 2004

Abstract—The process of chaotic synchronization of two coupled dynamical systems with slightly different parameters has been studied. The transition from phase to lag synchronization regime is related to the fact that an increasing number of spectral components in the Fourier spectra of the coupled oscillators are synchronized. For this reason, it is possible to introduce the notion of the degree of phase synchronization. A method of description of the degree of phase synchronization is proposed and it is shown that this value increases with the coupling parameter. © 2004 MAIK "Nauka/Interperiodica".

The phase synchronization of systems in the regime of dynamical chaos is among the important problems in the modern theory of nonlinear oscillations [1, 2]. This phenomenon is described and analyzed using the concept of the phase $\phi(t)$ of a chaotic signal [1–6]. The phase synchronization implies that the phases of chaotic signals are mutually entrained, while their amplitudes remain uncorrelated and appear chaotic. The entrainment of phases leads to the coincidence of frequencies of the two signals. The frequency of a chaotic signal is defined as the average rate of phase variation,

$$\Omega = \langle \dot{\phi}(t) \rangle. \qquad (1)$$

At the same time, in some cases (in particular, for the so-called systems with poorly defined phase [3, 5]), attempts at describing the phenomenon of phase synchronization in terms of the phase $\phi(t)$ may lead to incorrect results [7]. This is related to the fact that the chaotic time series for such systems is characterized by a Fourier spectrum containing no clearly pronounced main spectral component (or there are several such components). In the case when a chaotic signal spectrum has a single pronounced frequency component, the phase $\phi(t)$ of this signal is in fact associated with this main frequency and, hence, chaotic signal frequency (1) must coincide with the main frequency (see [7]).

If there is no dominating frequency component in the spectrum, the phase $\phi(t)$ of a chaotic signal cannot adequately describe the system dynamics. For such systems, we have recently [8, 9] suggested to use a family of phases $\phi_s(t)$ introduced using a continuous wavelet transform [10] so that each particular phase $\phi_s(t)$ is associated with its own time scale s. In this case, the phenomenon of phase synchronization is manifested by a synchronous behavior of the phases of coupled cha-

otic oscillators observed on certain synchronized time scales s, for which

$$|\phi_{s1}(t) - \phi_{s2}(t)| < \text{const}. \qquad (2)$$

It was demonstrated [8] that the range of synchronized scales s increases with the coupling parameter until all time scales are synchronized. This corresponds to the state of lag synchronization [11], whereby the coinciding states of interacting oscillators are shifted in time relative to each other: $\mathbf{x}_1(t - \tau) \simeq \mathbf{x}_2(t)$. Further increase in the coupling parameter leads to a decrease in the time shift τ. The oscillators tend to the regime of complete (full) synchronization, $x_1(t) \simeq x_2(t)$, and the phase difference $\phi_{s1}(t) - \phi_{s2}(t)$ tends to zero on all time scales.

Thus, the family of phases introduced by a wavelet transform for a chaotic signal allows the regime of phase synchronization of coupled oscillator to be effectively revealed. On the other hand, the continuous wavelet transform is characterized by a lower frequency resolution than the Fourier transform (see [10]). The continuous wavelet transform appears to smoothen the Fourier spectrum, whereby the dynamics on a time scale s is determined not only by the spectral component $f = 1/s$ of the Fourier spectrum. This dynamics is also influenced by the neighboring components as well, the degree of this influence being dependent both on their positions in the Fourier spectrum and on the intensities. Thus, the fact that coupled chaotic oscillators exhibit synchronization on a time scale s of the wavelet spectrum by no means implies that the corresponding component $f = 1/s$ of the Fourier spectrum of these systems is also synchronized.

This study was aimed at elucidating the question as to how the synchronization of separate spectral components in the Fourier spectra of coupled chaotic oscilla-

tors proceeds depending on the coupling parameter in the phase synchronization regime.

Let $x_1(t)$ and $x_2(t)$ be the time series generated by the first and second coupled chaotic oscillators, respectively. The corresponding Fourier spectra are determined by the relations

$$S_{1,2}(f) = \int_{-\infty}^{+\infty} x_{1,2}(t)e^{-i2\pi ft}dt. \qquad (3)$$

Accordingly, each spectral component f of the Fourier spectrum $S(f)$ can be brought into correspondence with an instantaneous phase $\phi_f(t) = \phi_{f0} + 2\pi ft$. However, since the phase $\phi_f(t)$ corresponding to the frequency f of the Fourier spectrum $S(f)$ linearly increases with the time, the phase difference of the interacting oscillators at this frequency, $\phi_{f1}(t) - \phi_{f2}(t) = \phi_{f01} - \phi_{f02}$, is always limited and, hence, the traditional condition of phase entrainment (used for determining the phase synchronization regime),

$$|\phi_1(t) - \phi_2(t)| < \text{const}, \qquad (4)$$

is useless. Apparently, a different criterion should be used to define the phase synchronization of coupled oscillators at a given frequency f.

In the regime of lag synchronization, the behavior of coupled oscillators is synchronized on all time scales s of the wavelet transform (see [8]). Therefore, we may expect that all frequency components of the Fourier spectra of the systems under consideration should be synchronized as well. In this case, $x_1(t - \tau) \simeq x_2(t)$ and, hence, by virtue of (3), we must have $S_2(f) \simeq S_1(f)\exp(i2\pi\tau f)$. Thus, in the case of coupled chaotic oscillators occurring in the regime of lag synchroniza-

tion, their instantaneous phases corresponding to the spectral component f of the Fourier spectra $S_{1,2}(f)$ will be related as $\phi_{f2}(t) \simeq \phi_{f1}(t) + 2\pi\tau f$ and, hence, the phase difference $\phi_{f2}(t) - \phi_{f1}(t)$ must obey the relation

$$\Delta\phi_f = \phi_{f1} - \phi_{f2}(t) = 2\pi\tau f. \qquad (5)$$

According to this, the points corresponding to the phase difference of the spectral components of chaotic oscillators in the regime of lag synchronization on the $(f, \Delta\phi_f)$ plane must fit to a straight line sloped at $k = 2\pi\tau$ (see also [12]).[1]

It was demonstrated [8] that breakage of the lag synchronization regime (e.g., as a result of decrease in the coupling of oscillators) and transition to the regime of phase synchronization results in the loss of synchronism for a part of time scales s of the wavelet spectra. Accordingly, we may expect some of the spectral components of the Fourier spectra in the phase synchronization regime will also lose synchronism and the points on the $(f, \Delta\phi_f)$ plane will deviate from the aforementioned straight line. It is natural to assume that synchronism will be lost primarily for the spectral components accounting for a small fraction of energy, while the components corresponding to a greater energy fraction will remain synchronized and the corresponding points on the $(f, \Delta\phi_f)$ plane will be situated at the straight line. As the coupling parameter further decreases, an increasing part of the spectral components will deviate from synchronism. However, as long as the most "energetic" components remain synchronized, the coupled systems will exhibit the regime of phase synchronization.

Let us introduce a quantitative characteristic of the number of spectral components of the Fourier spectra $S_{1,2}(f)$ occurring in the regime of synchronism,

$$\sigma_L = \frac{\displaystyle\int_0^{+\infty} H(S_1(f) - L)H(S_2(f) - L)(\Delta\phi_{f_j} - 2\pi\tau f_j)^2 df}{\displaystyle\int_0^{+\infty} H(S_1(f) - L)H(S_2(f) - L)df}, \qquad (6)$$

where $H(\xi)$ is the Heaviside function, L is the threshold power level (in dB) above which the spectral components are taken into account, and τ is determined by the time shift of the most energetic frequency component (f_m) in the Fourier spectra $S_{1,2}(f)$: $\tau = (\phi_{f_m2} - \phi_{f_m1})/(2\pi f_m)$. The quantity σ_L provides a measure of the degree of phase synchronization. This characteristic tends to zero in the regimes of complete and lag synchronization. In the case of phase synchronization, σ_L

increases with the number of desynchronized spectral component of the Fourier spectra $S_{1,2}(f)$ of coupled oscillators.

Real data are usually represented by discrete time series of a finite length. In such cases, continuous Fou-

---

[1] It is obvious that, in the regime of complete synchronization, $\mathbf{x}_1(t)f \simeq \mathbf{x}_2(t)$, the phase difference $\Delta\phi_f$ is zero for all components f of the Fourier spectrum.
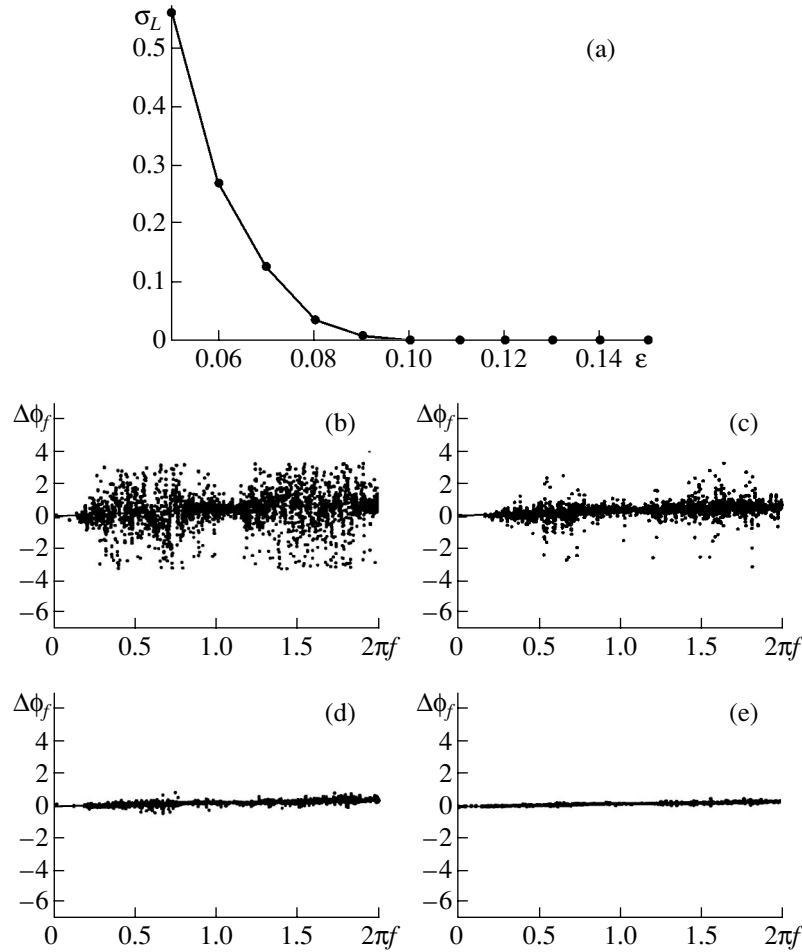
Fig. 1. (a) Plot of the degree of phase synchronization σ_L versus coupling parameter ε and (b–e) the phase difference $\Delta\phi_f$ of various spectral components f of the Fourier spectra $S_{1,2}(f)$ of two coupled Rössler systems for $\varepsilon = 0.05$ (b), 0.08 (c), 0.1 (d), and 0.15 (e) at a power level of $L = -40$ dB. The plots are constructed for the time series $x(t)$ with a length of 2000 dimensionless time units at a discretization step of $h = 0.2$. The results were averaged over 150 time series.

rier transform (3) has to be replaced by its discrete analogue, and integral (6), by the sum

$$\sigma_L = \frac{1}{N}\sum_{j=1}^{N}(\Delta\phi_{f_j} - 2\pi\tau f_j)^2 \qquad (7)$$

taken over all spectral components of the Fourier spectra $S_{1,2}(f)$ with powers above L. In calculating σ_L, it is expedient to perform averaging over a set of time series [12, 13].

In order to illustrate the approach proposed above, let us consider two coupled Rössler systems in the vortex chaos regime,

$$\dot{x}_{1,2} = -\omega_{1,2}y_{1,2} - z_{1,2} + \varepsilon(x_{2,1} - x_{1,2}),$$
$$\dot{y}_{1,2} = \omega_{1,2}x_{1,2} + ay_{1,2} + \varepsilon(y_{2,1} - y_{1,2}), \qquad (8)$$
$$\dot{z}_{1,2} = p + z_{1,2}(x_{1,2} - c),$$

where ε is the coupling parameter, $\omega_1 = 0.98$, and $\omega_2 = 1.03$. By analogy with the case studied in [14], the val-

ues of control parameters were selected as follows: $a = 0.22$, $p = 0.1$, and $c = 8.5$. It is known [14] that two coupled Rössler systems with $\varepsilon = 0.05$ occur in the regime of phase synchronization. For $\varepsilon = 0.15$, the same systems exhibit lag synchronization.

Figure 1a shows a plot of the degree of phase synchronization σ_L versus coupling parameter ε. As can be seen, σ_L tends to zero when the coupling parameter increases, which is indicative of the transition from phase to lag synchronization. Figures 1b–1e illustrate the increase in the number of synchronized spectral components of the Fourier spectra $S_{1,2}(f)$ of the two coupled systems with increasing ε. Indeed, Fig. 1b corresponds to the case of weak phase synchronization ($\varepsilon = 0.05$), when this regime has just appeared; Figs. 1c and 1d show well-pronounced phase synchronism ($\varepsilon = 0.08$ and 0.1, respectively); and Fig. 1e reflects the state of lag synchronization ($\varepsilon = 0.15$), whereby all spectral components are synchronized.
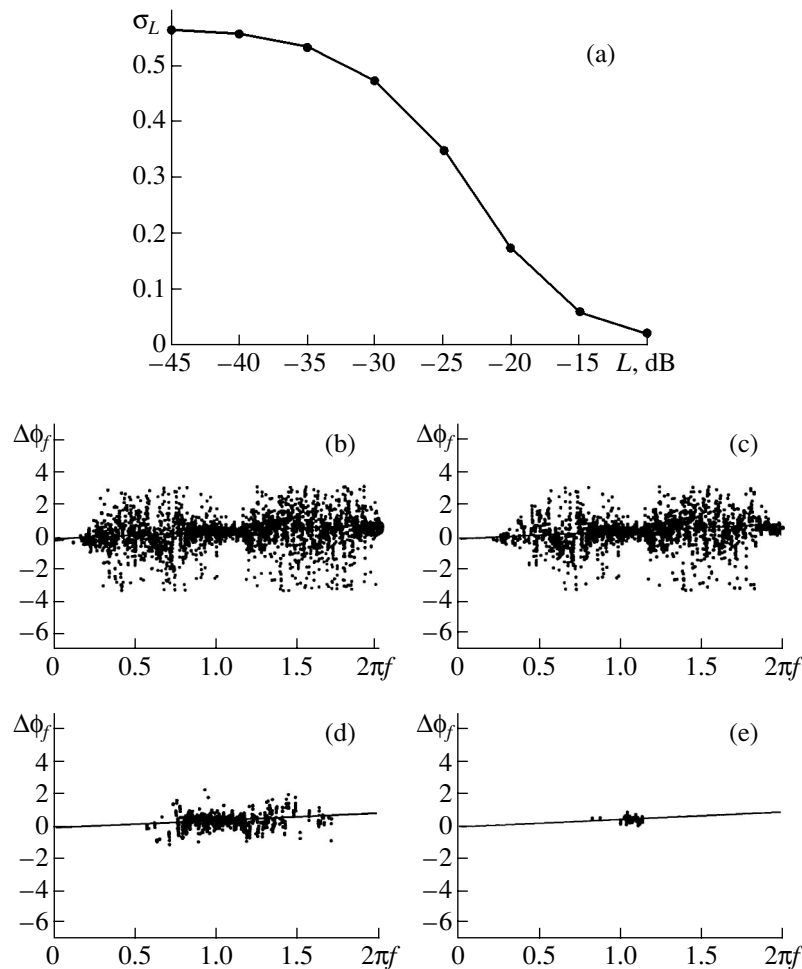
Fig. 2. (a) Plot of the degree of phase synchronization σ_L versus power L at which the spectral components f_j of the Fourier spectra $S_{1,2}(f)$ are taken into account in the formula for σ_L and (b–e) the spectra of phase difference $\Delta\phi_f$ of various spectral components f of the Fourier spectra $S_{1,2}(f)$ of two coupled Rössler systems for various power levels $L = -40$ dB (b), -30 dB (c), -20 dB (d), and -10 dB (e) for $\varepsilon = 0.05$.

Another important question is which spectral components of the Fourier spectra of interacting chaotic oscillators are synchronized first and which are last. Figure 2a shows a plot of the degree of phase synchronization σ_L for $\varepsilon = 0.05$ (corresponding to weak phase synchronization) versus power L at which the spectral components f_j of the Fourier spectra $S_{1,2}(f)$ are taken into account in formula (7). As can be seen, "truncation" of the spectral components possessing small energies leads to a decrease in σ_L. Figures 1b–1e illustrate the distribution of the phase difference $\Delta\phi_f$ of the spectral components f with the power exceeding the preset level L. The data in Fig. 2 show that the most "energetic" spectral components are first synchronized upon the onset of phase synchronization. On the contrary, the components with low energies first go out of synchronism upon breakage of the lag synchronization regime.

REFERENCES

1. M. G. Rosenblum, A. S. Pikovsky, and J. Kurths, Phys. Rev. Lett. **76**, 1804 (1996).

2. G. V. Osipov, A. S. Pikovsky, M. G. Rosenblum, and J. Kurths, Phys. Rev. E **55**, 2353 (1997).

3. A. Pikovsky, M. Rosenblum, and J. Kurths, Int. J. Bifurcation Chaos Appl. Sci. Eng. **10**, 2291 (2000).

4. V. S. Anishchenko and T. E. Vadivasova, Radiotekh. Élektron. (Moscow) **17**, 133 (2002).

5. A. Pikovsky, M. Rosenblum, and J. Kurths, *Synchronization: A Universal Concept in Nonlinear Sciences* (Cambridge Univ. Press, Cambridge, 2001).

6. V. S. Anishchenko, V. Astakhov, A. Neiman, T. Vadivasova, and L. Schimansky-Geier, *Nonlinear Dynamics of Chaotic and Stochastic Systems. Tutorial and Modern Developments* (Springer-Verlag, Heidelberg, 2001).

7. T. E. Vadivasova and V. S. Anishchenko, Radiotekh. Élektron. (Moscow) **49**, 76 (2004).

8. A. A. Koronovskiĭ, D. I. Trubetskov, and A. E. Hramov, Dokl. Akad. Nauk **395**, 40 (2004) [Dokl. Phys. **49**, 143 (2004)].

9. A. A. Koronovskiĭ and A. E. Hramov, Pis'ma Zh. Éksp. Teor. Fiz. **79**, 391 (2004) [JETP Lett. **79**, 316 (2004)].

10. A. A. Koronovskiĭ and A. E. Hramov, *Continuous Wavelet Analysis and Its Applications* (Fizmatlit, Moscow, 2003) [in Russian].

11. M. Rosenblum, A. S. Pikovsky, and J. Kurths, Phys. Rev. Lett. **78**, 4193 (1997).

12. V. S. Anishchenko, T. E. Vadivasova, D. E. Postnov, and M. A. Safonova, Int. J. Bifurcation Chaos Appl. Sci. Eng. **2**, 633 (1992).

13. V. S. Anishchenko, T. E. Vadivasova, and V. V. Astakhov, *Nonlinear Dynamics of Chaotic and Stochastic Systems* (Saratov. Gos. Univ., Saratov, 1999) [in Russian].

14. M. G. Rosenblum, A. Pikovsky, J. Kurths, *et al.*, Phys. Rev. Lett. **89**, 264102 (2002).

Translated by P. Pozdeev

High-Intensity X-ray Microbeams
Obtained Using a Cylindrical Polycapillary Structure

A. Yu. Romanov* and I. V. Dmitriev

Institute for Roentgen Optics, Moscow, Russia
* e-mail: androm2@yandex.ru
Received March 24, 2004

Abstract—High-intensity quasi-parallel X-ray microbeams with a radiation flux density on the order of 10^{10} photon/(s mm^2) and a divergence of several milliradians, which is close to the parameters of synchrotron radiation, were obtained using a microfocus source based on a transmission-type X-ray tube. The divergent X-ray radiation was converted into a quasi-parallel beam using a cylindrical structure of Kumakhov polycapillary optics with a micron channel diameter. © *2004 MAIK "Nauka/Interperiodica".*

Solving some problems of X-ray microanalysis requires using high-intensity microbeams. In addition, some applications pose limitations with respect to the radiation beam divergence [1]. The problem of obtaining high-flux-density X-ray radiation beams under laboratory conditions is important because conventional high-intensity radiation sources such as synchrotrons and water-cooled X-ray tubes with rotating anode are expensive and not readily accessible. Additional requirements concerning quasi-parallel microbeams make the task even more difficult. A possible solution is offered by X-ray systems implementing Kumakhov polycapillary optics in combination with usual X-ray tubes of the transmission and reflection types. In this way, it is possible to obtain X-ray microbeams with required parameters even using low-power X-ray tubes [2–4].

The possibility of using Kumakhov semilenses for obtaining quasi-parallel beams is well known [2–4]. Using microfocus semilenses with focal distances below 1 mm, it is possible to obtain X-ray sources with a beam divergence on a level of the critical total external reflection angle and a flux density on the order of 10^{10} photon/(s mm^2) for monochromatic radiation (e.g., CuK$_\alpha$) based on usual X-ray tubes without water cooling [2]. However, the cross-section area of the X-ray beam is determined by the output diameter of a semilens, which is typically on the order of a millimeter. Such dimensions are not suited for some applications of X-ray microanalysis, while placing a diaphragm restricting the beam size past this system significantly decreases the radiation intensity.

There are two possible ways to decrease the beam cross section and increase the radiation flux density in quasi-parallel microbeams. The first way is via improvement of the optical element, and the second, via modification of the X-ray source. We have achieved the desired result by combining both methods. The new

possibilities were provided, first, by the development of special microfocus X-ray sources enabling ultimate approach to the focal spot [4] and, second, by the development of a technology of cylindrical polycapillary structures with micron channels [2].

This study was aimed at experimental verification of the possibility to obtain high-intensity quasi-parallel X-ray microbeams using the aforementioned microfocus X-ray source and a polycapillary optical element.

The essence of the proposed method is as follows. The optimized cylindrical polycapillary structure is placed maximally close to the focal spot of a specially modified X-ray tube. An intense X-ray quasi-parallel microbeam is obtained at the output of the polycapillary structure [5]. The experimental optical scheme is depicted in the figure, where d_0 is the focal spot size of the X-ray tube, f_{in} is the focal distance (maximum approach to the focal spot), d_{in} is the input diameter (exposed spot), and d_{out} is the output diameter (output beam size). Using this scheme, it is possible to obtain beams with a diameter determined by the size of the effective focal spot of the X-ray tube and a distance from the focal spot to the input of the polycapillary structure $d_{in} = d_{out} = d_0 + 2f\theta_c$, where θ_c is the angle of critical total external reflection from the inner capillary
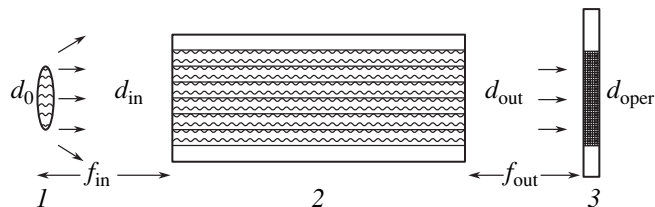
Schematic diagram illustrating the formation of an X-ray microbeam using a polycapillary structure: (*1*) focal spot; (*2*) polycapillary stricture; (*3*) detector.

walls. Since the critical angles are small, the increase in the output beam diameter as a result of the divergence of a beam passing through the polycapillary structure is not large. For example, at the distance achieved in our experiments (200 μm) and a radiation energy of 8 keV ($\theta_c \cong 4 \times 10^{-3}$ rad), the corresponding divergence is as small as $d_{incr} = 2\theta_c f_{in} = 2 \times 4 \times 10^{-3} \times 200 = 1.6$ μm. The operating beam diameter is also determined by the divergence and the distance to an object: $d_{oper} = d_{out} + 2\theta_c f_{out}$. The divergence of obtained beams was on the order of double critical total external reflection angle. Moreover, according to some data [6], the real divergence is even smaller due to the considerable role of the wave properties in submicron channels.

Owing to the maximum proximity of the polycapillary structure to the X-ray source (in our case, a transmission-type X-ray tube), the input radiation flux density increases and the output beam diameter d_{out} is equal to the diameter of the working zone of a polycapillary structure (exposed spot) d_{in} of a straight-wall cylindrical capillary structure (i.e., the spot size is transmitted without changes) [5]. The straight-wall cylindrical capillary structure provides for a greater transmission than that of a structure with bent channels (such as a semilens). Thus, the polycapillary cylindrical structure (column) with the minimum possible channel size is, probably, among the optimum structures for obtaining high-intensity quasi-parallel X-ray microbeams due to the maximum approach to the focal spot.

The microfocus X-ray source (designed and developed at the Institute for Roentgen Optics, Moscow) was specially optimized for use with polycapillary optics. The source makes use of a BS-11 transmission-type X-ray tube. The electron beam is focused by a system of magnetic lenses. The thickness of a beryllium foil in the exit window was 200 μm. The tube design provides for the maximum approach to the anode: a polycapillary structure can be situated at a distance of $f_{in} \approx 200$ μm from the focal spot.

The polycapillary cylindrical structure (also developed at the Institute for Roentgen Optics, Moscow) had a minimum column length necessary only for a small-angle collimation (involving several reflections). For example, a column with a capillary diameter of 1 μm provides for 4 reflections of CuK_α radiation over a length of 1 mm, but such short columns are not convenient in use. We used a 1-cm-long column with a capillary diameter of 2 μm and a total structure diameter of 2 mm.

The experiments were performed using an X-ray tube with a copper anode. The maximum tube power for operation without any risk of damaging a target is 10 W. The tube was operated at 25 keV and a current of 10 μA. The measured radiation beam intensity at the output of the polycapillary cylindrical structure was 3×10^5 photon/s. Measurements of the beam size showed that the full width at half maximum intensity was 20 μm. It was established that the tube exhibits a direct dependence of the intensity on the current; for this reason, the intensity was extrapolated to a value per unit power (1 W).

The radiation flux density calculated using the results of measurements was 10^9 photon/(s mm^2) per 1 W of electron beam. Increasing the tube power to 10 W yields 10^{10} photon/(s mm^2), which is comparable with the values for synchrotron radiation sources. For example, FOP synchrotron (ESRF) provides for a flux density of 5×10^{10} photon/(s mm^2) in the energy range from 7 to 21 keV, while ANKA synchrotron (Karlsruhe) yields 10^{12} photon/(s mm^2) in the 4–20 keV range.

Thus, we have obtained high-intensity quasi-parallel X-ray microbeams with a cross-section diameter on the order of 10 μm and a radiation flux density on the order of 10^{10} photon/(s mm^2). The laboratory source is based on a usual transmission-type X-ray tube without water cooling. Additional optimization of the scheme and components will provide for a further increase in the radiation flux density in the beam up to 10^{12}–10^{13} photon/(s mm^2).

REFERENCES

1. P. Dhez, P. Chevallier, T. B. Lucatorto, and C. Tarrio, Rev. Sci. Instrum. **70**, 1907 (1999).
2. M. A. Kumakhov, Proc. SPIE **4765**, 20 (2002).
3. A. Yu. Romanov, I. V. Dmitriev, and A. Yu. Akulov, Inzh. Fiz., No. 1 (2004).
4. O. M. Mikhin, M. A. Kumakhov, N. S. Ibraimov, and V. D. Gelever, Proc. SPIE **4765**, 194 (2002).
5. A. Yu. Romanov, Izmer. Tekh. (2004) (in press).
6. G. Cappucio and S. B. Dabagov, Proc. SPIE **4765**, 99 (2002).

Translated by P. Pozdeev

Interplay of Surface Effects
in a Thin Nematic Liquid Crystal Layer

S. L. Lopatnikov and G. Gillespie, Jr.

Center for Composite Materials, Department of Environmental and Civil Engineering, University of Delaware,
Newark, Delaware 19716, USA

Center for Composite Materials, Department of Materials Science, University of Delaware,
Newark, Delaware 19716, USA

Received November 24, 2003; in final form, March 12, 2004

Abstract—Manifestations of the competition of surface effects in a thin nematic liquid crystal (LC) layer are considered. It is shown that the LC director field lines remain straight irrespective of the preferred anchoring angles at the LC boundary surfaces. The angle between the director field lines and the plane of the LC layer depends on these preferred anchoring angles and on the Rapini–Papoular energy ratio at the boundary surfaces. There are two possible director orientations differing by 90°. Switching between these states can be induced by chemical factors or by external fields. In contrast to the well-known Fréedericksz transition, the work required for such switching is partly performed by the competing surfaces. Hence, the LC layer switching only requires overcoming the difference between the Rapini–Papoular energies, which can be rendered small by properly selecting LC–substrate pairs. © *2004 MAIK "Nauka/Interperiodica".*

This paper considers orientation of a liquid crystal (LC) in a layer of thickness smaller than the correlation length, whereby the two LC boundaries exhibit a competitive action upon the LC state. To the best of our knowledge, this problem was only briefly and not quite correctly touched upon in the monograph of de Gennes and Prost [1, Ch. 3.1.4.2, p. 112], while thorough analysis has not been performed so far.

However, such an analysis leads to interesting and nontrivial conclusions. In particular, it turns out that the LC director field lines in a thin LC layer virtually remain straight irrespective of the preferred angles of orientation (anchoring) of the LC molecules at the boundary surfaces and of the corresponding surface energies W_0 and W_1. Moreover, for the given preferred anchoring angles, there are two possible stationary LC orientations, only one of which corresponds to the absolute minimum of energy of the LC layer. By changing the ratio of W_0 and W_1 values, it is possible to switch the LC from one state to another. This transition is to a certain extent analogous to the well-known Fréedericksz transition, but the role of an "external field" is played by one boundary with respect to another.

Free energy of a planar LC layer. In the absence of external fields, the free energy of a nematic LC layer can be represented as a sum of the bulk and surface components:

$$F = F_{LC} + F_S. \qquad (1)$$

Here, F_{LC} is the LC volume free energy and F_S is the energy of interaction between the LC and the layer boundaries.

Considering a flat LC layer and assuming that the director field depends only on the transverse coordinate z (and is independent of the coordinates x and y in the layer plane), we can write the Frank (Frank–Oseen–Zohar) energy [1] as

$$
F_{LC} = \frac{K_3}{2}\int\left[(1 - \gamma\sin^2\Theta)\left(\frac{\partial\Theta}{\partial z}\right)^2 \right.
$$
$$
\left. + \sin^2\Theta(1 - \beta\sin^2\Theta)\left(\frac{\partial\Psi}{\partial z}\right)^2\right]d\Omega, \qquad (2)
$$

where K_1, K_2, and K_3 are the Frank coefficients characterizing "elasticity" of the nematic LC; Ω is the LC volume; Θ and Ψ are the polar and azimuthal angles of the LC director at a given point, respectively; $\gamma = (K_3 - K_1)/K_3$; and $\beta = (K_3 - K_2)/K_3$ ($|\gamma|$, $|\beta| < 1$).

The surface energy consists of two parts. The first part is the saddle-splay energy

$$
F_{S1} = -\int_S \frac{1}{2}K_{SS}[(\mathbf{n}\,\mathrm{div}\,\mathbf{n} + \mathbf{n}\times\nabla\times\mathbf{n})\cdot\mathbf{N}]dS. \qquad (3)
$$

The second part describes the interaction between LC molecules and the surface. We will use a simple model of this interaction described by the Rapini–Papoular energy

$$
F_{S2} = \int_S \frac{1}{2}W(1 - ((\mathbf{n}\cdot\boldsymbol{\eta}))^2)dS. \qquad (4)
$$

Here, **n** is the unit vector of the director field, **η** is the unit vector determining preferred LC orientation at the surface, and W is the characteristic of "stiffness" of this orientation. Vector **η** is described in terms of the polar (ϑ) and azimuthal (φ) angles. Where necessary, the angles are provided with subscripts 0 and 1, indicating the two surfaces (layer boundaries).

Nematic LC without twist. With a view to further analysis of the general case with arbitrary preferred orientation angles, let us first study the structure of the director field inside the LC layer. We use the complete system of equations for the polar and azimuthal angles and characterize arbitrary director orientations at the boundaries by the polar and azimuthal angles (Θ_0, Ψ_0 for one surface and Θ_1, Ψ_1 for the other surface). Minimizing the volume Frank energy, we obtain two Euler's equations

$$\frac{d}{dz}\left[(1-\gamma\sin^2\Theta)\frac{d\Theta}{dz}\right] + \gamma\sin\Theta\cos\Theta\left(\frac{d\Theta}{dz}\right)^2$$
$$- \sin\Theta\cos\Theta(1-2\beta\sin^2\Theta)\left(\frac{\partial\Psi}{dz}\right)^2 = 0, \tag{5}$$

$$\frac{d}{dz}\left(\sin^2\Theta(1-\beta\sin^2\Theta)\frac{d\Psi}{dz}\right) = 0. \tag{6}$$

Equation (6) yields the relation

$$\frac{d\Psi}{dz} = \frac{C}{\sin^2\Theta(1-\beta\sin^2\Theta)}, \tag{7}$$

where C is a constant determined from the boundary conditions for the azimuthal angles

$$C = \frac{\Psi_1-\Psi_0}{\int_0^H \frac{dz}{\sin^2\Theta(1-\beta\sin^2\Theta)}}. \tag{8}$$

As can be seen, this constant characterizes the "twist" of the nematic LC. Eliminating the derivative $d\Psi/dz$ from Eq. (5) with the aid of formula (7), we obtain an equation for the polar angle

$$\frac{d}{dz}\left[(1-\gamma\sin^2\Theta)\frac{d\Theta}{dz}\right] + \gamma\sin\Theta\cos\Theta\left(\frac{d\Theta}{dz}\right)^2$$
$$- \frac{\cos\Theta(1-2\beta\sin^2\Theta)C^2}{\sin^3\Theta(1-\beta\sin^2\Theta)^2} = 0. \tag{9}$$

Equation (9) appears rather awkward.[1] However, it can be simplified and readily solved in the absence of

---

[1] In fact, this equation has an analytical solution, but it has a complicated form hindering insight into the physics of the problem and is not presented here.

twist, which corresponds to $C = 0$. Restricting the consideration to this particular case and introducing a new variable $q(\Theta) = \int_0^\Theta \sqrt{1-\gamma\sin^2\Theta}\,d\Theta \equiv E(\Theta|\gamma)$, where $E(\Theta|\gamma)$ is an incomplete elliptic integral of the second kind, we obtain

$$\frac{d^2q(\Theta)}{dz^2} = 0. \tag{10}$$

This equation has an evident solution

$$q(z) \equiv E(Q|\gamma) = Az + B, \tag{11}$$

where A and B are constants determined from the boundary conditions:

$$A = \frac{E(\Theta_1|\gamma)-E(\Theta_0|\gamma)}{H}, \quad B = E(\Theta_0|\gamma). \tag{12}$$

Thus, the general solution for $\Theta(z)$ inside the LC layer without twist in the implicit form appears as

$$E(\Theta(z)|\gamma) = \frac{E(\Theta_1|\gamma)-E(\Theta_0|\gamma)}{H}z + E(\Theta_0|\gamma). \tag{13}$$

Now, let us consider the surface contribution to the free energy. As can be readily shown, the saddle-splay energy F_{S1} in the case under consideration is zero and only the Rapini–Papoular energies have to be taken into account. Since vectors **η**$_0$ and **η**$_1$ have equal azimuthal angles, we select a coordinate system in which these angles are zero and obtain

$$F_{S2} = \bar{F}_{S2} + \int_S \frac{1}{2}[W_0\cos^2(\Theta_0-\vartheta_0)$$
$$+ W_1\cos^2(\Theta_1-\vartheta_1)]ds, \tag{14}$$

where ϑ_0 and ϑ_1 are the polar angles of vectors **η**$_0$ and **η**$_1$, respectively, and $\bar{F}_{S2}$ is the angle-independent part of the energy.

The final expression for the energy of the nematic LC layer is

$$F = \bar{F}_0 + \frac{1}{2}\int_S\left[K_3\frac{(E(\Theta_1|\gamma)-E(\Theta_0|\gamma))^2}{H}\right.$$
$$+ [W_0\cos^2(\Theta_0-\vartheta_0) + W_1\cos^2(\Theta_1-\vartheta_1)]dS. \tag{15}$$

By minimizing the total energy, we obtain two equa-

tions for the boundary angles Θ_0 and Θ_1:

$$(E(\Theta_1|\gamma) - E(\Theta_0|\gamma))\sqrt{1 - \gamma\sin^2\Theta_0}$$
$$+ \kappa_0\cos(\Theta_0 - \vartheta_0)\sin(\Theta_0 - \vartheta_0) = 0, \tag{16}$$

$$(E(\Theta_1|\gamma) - E(\Theta_0|\gamma))\sqrt{1 - \gamma\sin^2\Theta_1}$$
$$- \kappa_1\cos(\Theta_1 - \vartheta_1)\sin(\Theta_1 - \vartheta_1) = 0, \tag{17}$$

where

$$\kappa_0 = \frac{W_0 H}{K_3}; \quad \kappa_1 = \frac{W_1 H}{K_3}. \tag{18}$$

In the special case when $\vartheta_0 = \vartheta_1 = \vartheta$, Eqs. (16) and (17) have a trivial solution $\Theta_0 = \Theta_1 = \vartheta$ which is independent of the parameters κ_0 and κ_1. The form of relation (13) shows that, as can be expected, the current polar angle Θ in this case is independent of z and equal to ϑ. Following [1, 2], let us introduce the characteristic (extrapolation) lengths, $L_0 = K_3/W_0$ and $L_1 = K_3/W_1$. These quantities characterize the relative contributions of the surface and bulk effects. In terms of L_0 and L_1, the coefficients κ_0 and κ_1 can be expressed as $\kappa_0 = H/L_0$ and $\kappa_1 = H/L_1$.

The general solution to the problem of equilibrium distribution of the LC director is given by relation (13), where the angles Θ_0 and Θ_1 are determined as solutions of the system of Eqs. (16) and (17). The general solution has the following form:

$$E(\Theta(z)|\gamma) = E(\Theta_0(\vartheta_0, \vartheta_1, W_0, W_1, H)|\gamma)$$
$$+ (E(\Theta_1(\vartheta_0, \vartheta_1, W_0, W_1, H)|\gamma)$$
$$- E(\Theta_0(\vartheta_0, \vartheta_1, W_0, W_1, H)|\gamma))\frac{z - z_0}{H}. \tag{19}$$

This solution can be studied analytically, but we will consider here only two limiting cases, corresponding to the "thick" and "thin" LC layers.

If the LC layer is thick, whereby κ_0 and $\kappa_1 \gg 1$, we may neglect the first terms in Eqs. (16) and (17). This yields a trivial solution

$$\Theta_0 \approx \vartheta_0; \quad \Theta_1 \approx \vartheta_1. \tag{20}$$

In this case, the director field is determined by relation (13) where the angles Θ_0 and Θ_1 are replaced by ϑ_0 and ϑ_1:

$$E(\Theta(z)|\gamma) = E(\vartheta_0|\gamma)$$
$$+ (E(\vartheta_1|\gamma) - E(\vartheta_0|\gamma))\frac{z - z_0}{H}. \tag{21}$$

In other words, this situation corresponds to so-called strong anchoring. In this context, it should be noted that (in contrast to widely spread opinion) the "strong" or "weak" anchoring is not merely a characteristic of the LC–substrate interaction but also depends on the system dimensions.

Equilibrium of a thin LC layer. In this case, corresponding to κ_0, $\kappa_1 \ll 1$, Eqs. (16) and (17) immediately show that Θ_0 and Θ_1 must have close values irrespective of the preferred angles ϑ_0 and ϑ_1, since the difference $E(\Theta_1|\gamma) - E(\Theta_0|\gamma)$ is as small as $\kappa_0 \sim \kappa_1 \sim H/L$. Taking this into account, we can expand this difference into Taylor series. Retaining the main term in this expansion, we have

$$E(\Theta_1|\gamma) - E(\Theta_0|\gamma) \approx \left(\frac{dE(\Theta|\gamma)}{dz}\right)_0 \Delta\Theta$$
$$= \Delta\Theta\sqrt{1 - \gamma\sin^2\Theta_0}, \tag{22}$$

where $\Delta\Theta = \Theta_1 - \Theta_0$. Substituting this expression into Eqs. (16) and (17), we obtain

$$\Delta\Theta \approx -\kappa_0\frac{\sin 2(\Theta_0 - \vartheta_0)}{2(1 - \gamma\sin^2\Theta_0)}, \tag{23}$$

$$\Theta_0 = \frac{1}{2}\arctan\left(\frac{W_0\sin 2\vartheta_0 + W_1\sin 2\vartheta_1}{W_0\cos 2\vartheta_0 + W_1\cos 2\vartheta_1}\right) \pm \frac{\pi k}{2}, \tag{24}$$

where k is an arbitrary integer. However, since rotation of the director by π returns LC back to the initial state, we may consider only the two angles corresponding to $k = 0$ and 1.

Thus, there are only two significant values of the angle Θ_0, which differ by $\pi/2$. Both these values correspond to extrema of the total energy of the LC layer. The dependence of the resultant effective slope of the director on the preferred director orientation angles on the boundaries for both branches of the solution at various values of the ratio $\tau = W_1/W_2$ is presented in the figure. As can be seen, the main effective angle tends to the preferred boundary angle corresponding to a greater energy, and the other branch differs by $\pi/2$.

The question as to which of the two possible Θ_0 values brings the global energy minimum is most simply solved by directly comparing the total energies for the boundary angles Θ_0 and $\Theta_0 + \pi/2$.

Orientational phase transition in a thin LC layer. Let us consider another particular case, assuming that the preferred orientation angle for one surface is $\Theta_0 = \pi/2$, that on the other surface is $\Theta_1 = 0$, and $W_0 \neq W_1$. In this case,

$$\Theta_0 = \frac{1}{2}\arctan\left(\frac{0}{W_1 - W_0}\right) = 0 \text{ or } \frac{\pi}{2},$$
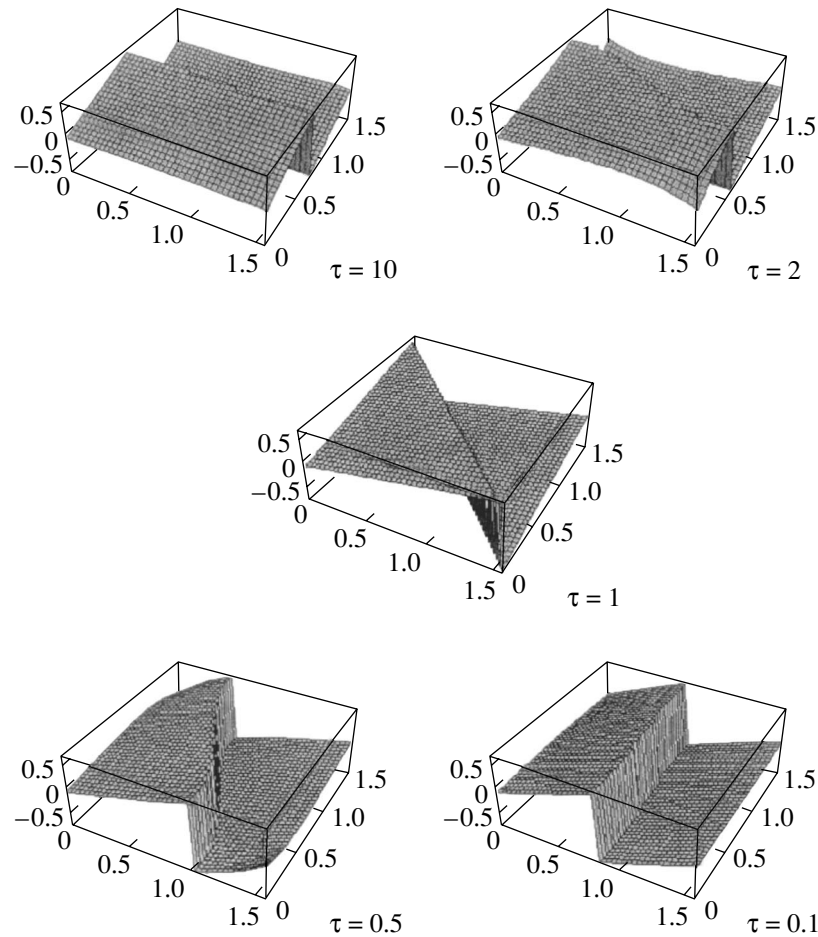
Resultant effective slope of the director in a thin LC layer as a function of the preferred director orientation angles on the boundaries for various values of the ratio $\tau = W_1/W_0$. The upper branch corresponds to the main value of expression (24), while the lower branch represents the other stationary value (differing by $\pi/2$). Which of the two solutions is realized depends on the ratio of surface energies $\tau = W_1/W_0$.

which implies that one of the two possibilities can be realized, whereby the LC layer occurs either in a homeotropic or in a homogeneous state. Which of the two states is practically realized? Comparing the layer energies, we readily establish that the global energy minimum is provided by an angle corresponding to the surface with a greater value of the Rapini–Papoular energy, that is, a stronger boundary alone (it should be recalled that the director field lies are straight) determines the LC orientation throughout the layer. The director is oriented parallel to the layer plane for $W_0 > W_1$, and it is oriented in the perpendicular direction for the opposite relation between the surface energies. The configurations are switched at $W_0 = W_1$. At this point, the director field orientation is undetermined.

Switching of the LC director orientation can be considered as a special phase transition induced by the competition of surface effects and mediated by the LC long-range order. This phase transition has a physical nature substantially different from that of the purely surface phenomena such as the jumplike change in the anchoring type, the Kosterlitz–Thouless phase transition, and quasi-critical surface energy behavior. It can be rather compared to the well-known Fréedericksz transition [3] induced by an external field but, in the case under consideration, the role of the external field is played by the stress field induced by a competing boundary.

On the other hand, the phase transition described above differs from the Fréedericksz transition in one important respect. In order to switch the LC layer between the states with different orientations in the case of the Fréedericksz transition, it is necessary to perform work, roughly speaking, against the total energy W_0 or W_1. In contrast, for such a switching in the case under consideration, it suffices to perform work only against the energy difference $W_0 - W_1$, which can be significantly smaller than either of the W_0 or W_1 val-

ues. A part of the work is performed by the competing boundary of the LC layer.

The properties of thin LC layers described in this paper can be used for the development of chemical and physical sensors.

REFERENCES

1. P. G. de Gennes and J. Prost, in *The Physics of Liquid Crystals,* Vol. 83 of the *International Series of Monographs on Physics* (Clarendon Press, Oxford, 1993).

2. L. M. Blinov, A. Y. Kabayenkov, and A. A. Sonin, Liq. Cryst. **5**, 645 (1989).

3. V. Fréedericksz and V. Zolin, Trans. Faraday Soc. **29**, 919 (1933).

Translated by P. Pozdeev

A Modified Kolmogorov Model and the Growth Rate of a Crystal Face of Arbitrary Size

N. V. Sibirev[a] and V. G. Dubrovskii[b]

[a] Ioffe Physicotechnical Institute, Russian Academy of Sciences, St. Petersburg, 194021 Russia
[b] St. Petersburg State University, St. Petersburg, Russia
Received April 9, 2004

Abstract—A modification of the geometric-probabilistic Kolmogorov model of crystallization is proposed which allows a finite size of the system to be taken into account. A generalized equation is obtained which describes the degree of filling of a finite system as a function of the time. The results are used to determine the growth rate of a crystal face of an arbitrary size in the case of lateral growth. It is shown that small crystal faces grow at a lower rate than large faces. The general expression for the normal growth rate asymptotically yields the well-known formulas in the limiting cases of very large and very small crystal faces. © *2004 MAIK "Nauka/Interperiodica".*

The process of crystal growth from molecular beams, vapor phase, and liquid solutions and melts is widely encountered in the technology of synthetic materials [1]. In many important cases, the growth of crystals proceeds layer by layer (lateral growth). One of the most important characteristics of the crystal growth process is the rate of the normal growth $V_H = dH/dt$, where H is the film thickness (below, H is expressed in units of the monolayer thickness). The main characteristics of the lateral growth of a crystal monolayer on a singular face are [1, 2] the intensity I of appearance of two-dimensional nuclei (nucleation rate), the rate of their lateral growth $v = dr/dt$ (r is the radius of the nucleus), and the crystal face size R. In the general case, the normal growth rate V_H depends on all these quantities, $V_H = V_H(I, v, R)$.

However, to the best of our knowledge, this dependence is still not determined for a crystal face of arbitrary size. Only expressions for the growth rate of very large and very small faces are known, which are derived as follows [1]. Consider a crystal face having the shape of a circle of radius R, let the nuclei have the shape of disks of radius r and a monoatomic height, and assume that the functions I and v are independent of the time ($I = I_0$, $v = v_0$). The time required for a growing nucleus to cover the entire face is R/v_0, and the time between two sequential nucleation events on the face is $1/(\pi R^2 I_0)$. The ratio of these quantities yields a dimensionless parameter

$$\alpha \equiv \frac{\pi I_0 R^3}{v_0}. \tag{1}$$

For $\alpha \ll 1$ (small crystal face), the nucleus will cover the entire face before the next nucleus appears (one-

center nucleation). In this case, the normal growth rate $V_H = \pi R^2 I_0$ is independent of v_0. When $\alpha \gg 1$ (large crystal face), the growth proceeds with polycenter nucleation, whereby many nuclei simultaneously occur on the crystal surface and a continuous layer is formed as a result of their coalescence. The normal growth rate in this case $V_H = (\pi v^2 I/3)^{1/3}$ is independent of R. Thus, crystal growth rate in the two known limiting cases is [1]

$$V_H = \begin{cases} \pi R^2 I_0, & \alpha \ll 1, \\ (\pi v_0^2 I_0/3)^{1/3}, & \alpha \gg 1. \end{cases} \tag{2}$$

This study was aimed at obtaining and analyzing a modified expression for the crystal growth rate generalizing formulas (2) to the case of arbitrary crystal face.

The original geometric-probabilistic model of crystallization proposed by Kolmogorov in 1937 [3] is widely used for the description of processes involving the growth of crystalline films [1, 2, 4, 5]. Let us consider the two-dimensional growth of a layer on a round crystal face of radius R under the following assumptions [4]: (i) nucleation obeys the Poisson law; (ii) the linear growth rate v of a nucleus is independent of its size r; (iii) all nuclei have the same round shape; (iv) the coalescence of nuclei proceeds by the solid state sintering mechanism; (v) spatial homogeneity: although, in contrast to the case of an infinite system (to which the Kolmogorov formula [3] is only applicable), we will take into account the finite size R, but it will be assumed that I and v are independent of the distance to the boundary.

Let us denote by $q(t)$ the probability for a certain point A on the surface to remain uncovered by the growing layer at the time t. Following [3], we introduce the concept of aggressor—a nucleus capable of reach-
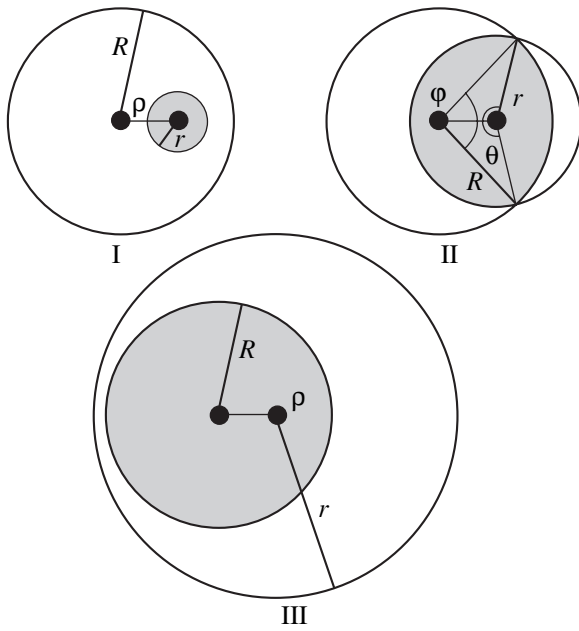
Fig. 1. Schematic diagrams illustrating determination of the area S on which an aggressor nucleus can appear. In case I, the crystal face is large and $S = \pi r^2$ irrespective of R and ρ; in the opposite case III, the crystal face is small and $S = \pi R^2$ irrespective of r an ρ; in the intermediate case II, the area S depends on the three variables r, ρ, and R.

ing the point A by the time t. With allowance for conditions (i) and (iv), the appearance of an aggressor automatically implies that the point A will be covered, On the contrary, the absence of such aggressor means that the point A will remain uncovered. Indeed, an aggressor can be prevented from reaching the point A only by the appearance of another nucleus, but the latter will automatically become the aggressor itself. Let us denote by $q(t, t')$ the probability of the absence of aggressors at the time t' $[q(t, t) \equiv q(t)]$ and by $\mu(t, t')$ the probability for an aggressor to appear at the time t' (with allowance for the finite size of the crystal face). Then, the probability that an aggressor does not appear at $t' + dt'$ is equal to the product of the probability of its absence before t' and the probability that it does not appear within the interval $(t', t' + dt')$: $q(t, t' + dt') = q(t, t')[l - \mu(t, t')dt']$. This relation leads to a differential equation $dq = -q\mu(t, t')dt'$ whose solution yields the Kolmogorov exponent [3, 4]. In terms of the crystallized surface fraction, $g(t) = l - q(t)$, the result appears as

$$g(t) = 1 - \exp\left(-\int_0^t \mu(t, t')dt'\right). \qquad (3)$$

If the above assumptions (i)–(v) are valid, the probability for an aggressor to appear at the moment t' is

$$\mu(t, t') = I(t')S(r(t, t'), \mathbf{x}, R), \qquad (4)$$

where

$$r(t, t') = \int_{t'}^t v(t'')dt'' \qquad (5)$$

is the current size of a nucleus appearing at t' and $S(r, \mathbf{x}, R)$ is the area of the surface on which an aggressor may appear at the time t' (this area depends on the coordinate $\mathbf{x}$ on the growth surface and on the face size R). Substituting expression (4) into Eq. (3), we obtain

$$g(t) = 1 - \exp\left(-\int_0^t I(t')S(r(t, t'), \mathbf{x}, R)dt'\right). \qquad (6)$$

In the system geometry under consideration, the area $S(r, \mathbf{x}, R)$ depends only on the distance $\rho = \mathbf{x}$. There are three possible situations as depicted in Fig. 1. In case I, the crystal face size is large and $S = \pi r^2$ irrespective of R and ρ. In the opposite case III, the crystal face is small and, hence, any nucleus is an aggressor and $S = \pi R^2$ irrespective of r an ρ. In the intermediate case II, the area S depends on the three variables r, ρ, and R. According to Fig. 1,

$$S(r, \rho, R) = \begin{cases} \pi r^2, & r \leq R - \rho, \\ R^2(\theta/2 - \sin\theta/2) + r^2(\varphi/2 - \sin\varphi/2), \\ \quad R - \rho < r < R + \rho, \qquad (7) \\ \pi R^2, & r \geq R + \rho, \end{cases}$$

where $\theta = 2\arctan[(R^2 + \rho^2 - r^2)/2R\rho]$ and $\varphi = 2\arccos[(r^2 + \rho^2 - R^2)/2r\rho]$. Substituting Eq. (6) into relations (7) yields the modified Kolmogorov formula, which is valid for the growth on a face of arbitrary size.

Formulas (6) and (7) are not convenient for calculations and analysis, because expression (6) for the degree of filling retains the coordinate dependence and expression (7) contains trigonometric functions. In order to obtain simplified expressions, let us average $S(r, \mathbf{x}, R)$ over the surface,

$$S(r(t, t'), R) = \frac{2}{R^2}\int_0^R S(r(t, t'), \rho, R)\rho\,d\rho, \qquad (8)$$

and substitute the result into (6). This procedure introduces some uncertainty, since we must, strictly speaking, average the filling g rather than the area S. However, for a small face, the loss of accuracy related to this substitution is not large, while for a large face, we are averaging an almost constant quantity. Detailed analysis of expression (7) shows that the function $S(r, R)$ calculated using Eqs. (7) and (8) for $r < 2R$ is approxi-

mated with a good accuracy by a polynomial of the fifth power (Fig. 2)

$$S(y, R) = \pi R^2 f(y),$$

$$f(y) = \begin{cases} y^2 - (3/8)y^3 - (1/16)y^4 + (1/32)y^5, & y \leq 2, \\ 1, & y > 2, \end{cases} \quad (9)$$

where $y(t, t') = r(t, t)/R$. Thus, a simplified formula for the degree of filling appears as

$$g(t) = 1 - \exp\left(-\pi R^2 \int_0^t I(t')f(y(t, t'))dt''\right), \quad (10)$$

where $f(y)$ is defined in Eq. (9).

For the constant values of $I = I_0$ and $v = v_0$, expression (10) simplifies to

$$g(t) = g(y) = 1 - \exp[-\alpha F(y)], \quad (11)$$

where $y = v_0 t/R$ is the dimensionless time, $\alpha = \text{const}$ is the parameters defined by formula (1), and $F(y)$ is the function defined as

$$F(y) = \begin{cases} (1/3)y^3 - (3/32)y^4 - (1/80)y^5 + (1/192)y^6, \\ y \leq 2, \\ y - 0.9, \quad y > 2. \end{cases} \quad (12)$$

According to formula (11), the characteristic time of face covering is $t_* = Ry_*/v_0$, where y_* is a solution of the transcendental equation

$$\alpha F(y) = 1. \quad (13)$$

The normal growth rate $V_H = 1/t_*$ can be expressed as

$$V_H = \frac{v}{Ry_*(\alpha)}. \quad (14)$$

Formulas (12)–(14) solve the problem of obtaining a modified expression for the growth rate on a finite crystal face of an arbitrary size. This expression yields correct asymptotic behavior for very small and very large faces. Indeed, for small α, (Fig. 3) $f(y) \approx y \gg 1$ and we obtain $y_* \approx 1/\alpha$. For large α, $f(y) \approx y^3/3 \ll 1$ and, hence, $y_* \approx (3/\alpha)^{1/3}$ that yields formula (2). The plot of V_H/V_0 versus r/R_0 (Fig. 3) constructed using Eqs. (12)–(14) and formula (1) for fixed I_0 and v_0 shows an
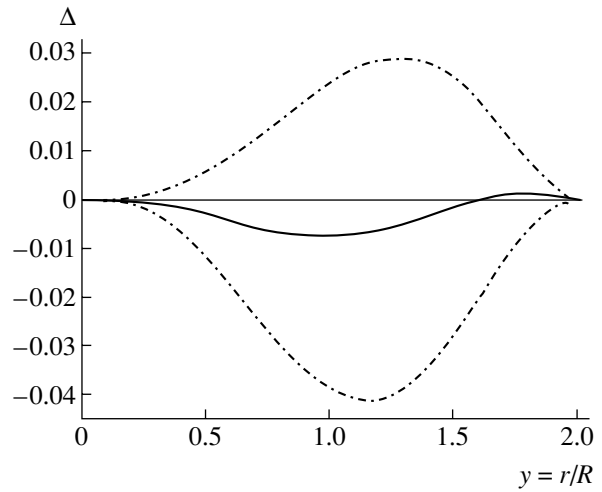

Fig. 2. A plot of the relative error $\Delta = (f - f_i)/f$ with respect to the exact solution $f(y) = S(R, y)/\pi R^2$ ($y = r/R$) obtained using Eqs. (7) and (8) approximated by polynomials $f_4(y) = y^2 - (1/2)y^3 + (1/6)y^4$, $f_5(y) = y^2 - (1/4)y^3 - (3/16)y^4 + (1/32)y^5$, and $f_{4-5}(y) = [f_4(y) + f_5(y)]/2$: (dashed curve) Δ_4; (dash–dot curve) Δ_5; (solid curve) Δ_{4-5}. The f_4 polynomial was constructed so that its value and the first and second derivatives at zero, as well as the value and the first derivative at $y = 2$, would coincide with the corresponding values and derivatives of f. The f_5 polynomial was constructed so that its value and the first and second derivatives at zero and at $y = 2$ would coincide with the corresponding values and derivatives of f.
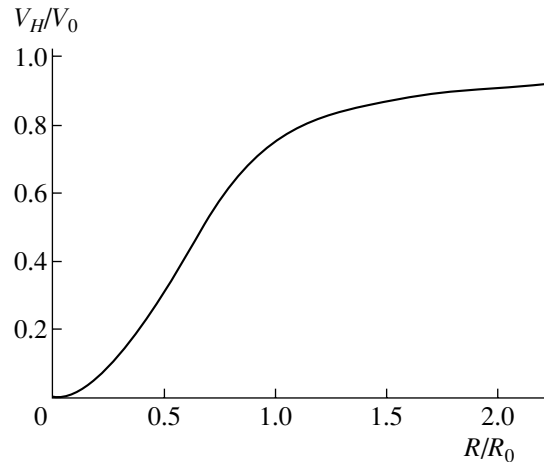

Fig. 3. A plot of the reduced normal growth rate V_H/V_0 versus reduced lateral face size R/R_0; $V_0 = (3\pi l v^2)^{1/3}$; $R_0 = (v/\pi l)^{1/3}$.

increase in the normal growth rate with increasing crystal face size.

The theory developed above can be used for studying the formation of nanodimensional crystals, in particular, nanowhiskers grown by the vapor–liquid–crystal mechanism [6], and for solving other problems

encountering dimensional effects related to small sizes of growing crystals.

REFERENCES

1. A. A. Chernov, E. I. Givargizov, Kh. S. Bagdasarov, V. A. Kuznetsov, L. N. Dem'yanets, and A. N. Lobachev, *Modern Crystallography,* Vol. 3: *The Formation of Crystals*, Ed. by B. K. Vainshtein (Nauka, Moscow, 1980) [in Russian].

2. S. A. Kukushkin and A. V. Osipov, Usp. Fiz. Nauk **168**, 1083 (1998) [Phys. Usp. **41**, 983 (1998)].

3. A. N. Kolmogorov, Izv. Akad. Nauk SSSR, Ser. Mat., No. 3, 355 (1937).

4. V. Z. Belen'kiĭ, *Geometric-Probabilistic Models of Crystallization* (Nauka, Moscow, 1989) [in Russian].

5. V. G. Dubrovskiĭ, Phys. Status Solidi B **171**, 345 (1992).

6. B. J. Ohlsson, M. T. Björk, M. H. Magnusson, *et al.*, Appl. Phys. Lett. **79**, 3335 (2001).

Translated by P. Pozdeev

Electron Transport Effects in the IR Photoconductivity of InGaAs/GaAs Structures with Quantum Dots

V. M. Danil'tsev, M. N. Drozdov, L. D. Moldavskaya, V. I. Shashkin, A. V. Germanenko, G. M. Min'kov, and A. A. Sherstobitov

Institute for Physics of Microstructures, Russian Academy of Sciences, Nizhni Novgorod, Russia
Ural State Technical University, Yekaterinburg, Russia
e-mail: lmd@ipm.sci-nnov.ru
Received April 26, 2004

Abstract—We have studied the temperature dependence of the Hall effects in multilayer selectively doped InGaAs/GaAs heterostructures with quantum dots (QDs). It was found that structures possessing photoconductivity in the IR range exhibit a sharp (nearly exponential) growth of the conductivity and Hall mobility in the temperature interval from 8 to 30 K at a virtually constant Hall coefficient and electron density. A new mechanism of the lateral photoconductivity in the structures with QDs is proposed which is related to the change in the electron mobility in the two-dimensional channel as a result of a decrease in the Coulomb scattering on charged QDs. © 2004 MAIK "Nauka/Interperiodica".

Introduction. In recent years, there has been extensive investigation of the possibility of using semiconductor heterostructures with quantum dots (QDs) as detectors for the middle and far infrared (IR) range. Owing to the zero-dimensional character of the dimensional quantization, the IR detectors based on QD heterostructures (in contrast to those with quantum wells) are capable of detecting radiation of any polarization at normal incidence. In addition, the QD structures may exhibit reduced electron scattering on phonons, which significantly increases the lifetime of photoexcited carriers—one of the main parameters determining the responsivity of IR photodetectors—and gives hopes for the possibility to operate at elevated temperatures.

Initially, the photoconductivity of QD heterostructures were performed in the vertical electron transport geometry standard for structures with quantum wells. The possibility of detecting radiation in the middle and far IR range (4–20 μm) using InGaAs/GaAs structures with QDs of various dimensions at normal incidence was demonstrated in [1–7]. The lateral IR photoconductivity of such structures was studied more recently [2, 8–11]. In heterostructures with quantum wells, this geometry is impossible because the lateral conductivity is shunted by strongly doped layers. It was pointed out [8, 10] that the systems with lateral charge transport may be expected to possess greater lifetimes of photoexcited electrons and, hence, higher quantum efficiencies than the structures with vertical transport. In the lateral geometry, the transfer of photoexcited electrons from QDs mostly proceeds via wetting layers or parallel high-conductivity channels. The record photosensitivity of such structures with QDs achieved at present is 11 A/W at 30 K [10]. It should be noted that both lateral and vertical current transfer in QD structures is considered within the framework of a single mechanism of IR photoconductivity based on a change of the sample resistance as a result of increase in the density of free charge carriers as a result of the photoexcitation of electrons trapped on QD levels.

This paper is aimed at attracting attention to a new mechanism of the photoconductivity in QD structures with lateral electron transport, which is based on a change of the charge carrier mobility under the action of IR radiation. Such a possibility is evidenced by the results [12–14] showing a considerable change in the mobility of carriers in two-dimensional (2D) channels situated near a QD layer, depending on the QD population and the distance to this layer. This implies that the scattering of 2D electrons near the QD layer is determined to a considerable degree by the Coulomb scattering on charged QDs and, hence, the carrier mobility will increase as a result of neutralization of these QDs. Since the lifetime of photoexcited carriers in QD structures are usually much greater compared to the momentum relaxation times, it is obvious that such phenomena can also be observed in the study of the lateral IR photoconductivity.

Recently [15], we have studied the IR photoconductivity of multilayer selectively doped InGaAs/GaAs heterostructures with QDs and observed two peaks at 5 and 16 μm, with rapid quenching of the long-wavelength line at $T > 40$ K. This paper presents the results of investigation of the lateral electron transport in such heterostructures at low temperatures.

Growth of InGaAs/GaAs heterostructures with QDs. Multilayer selectively doped InGaAs/GaAs heterostructures with 10 QD layers (Fig. 1) were grown by
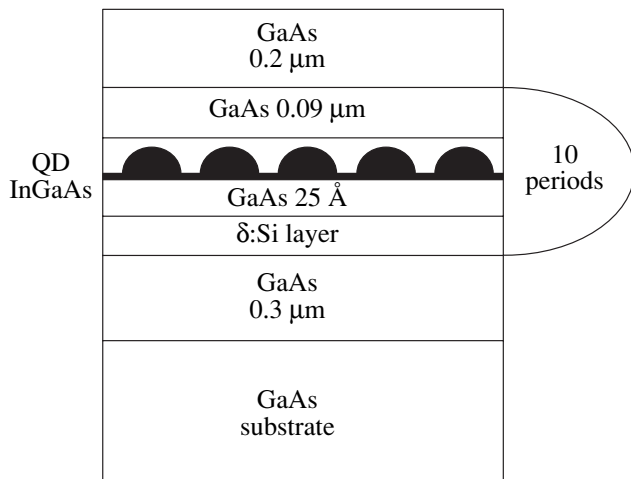
Fig. 1. Schematic diagram of a InGaAs/GaAs heterostructure with 10 layers of selectively doped QDs.
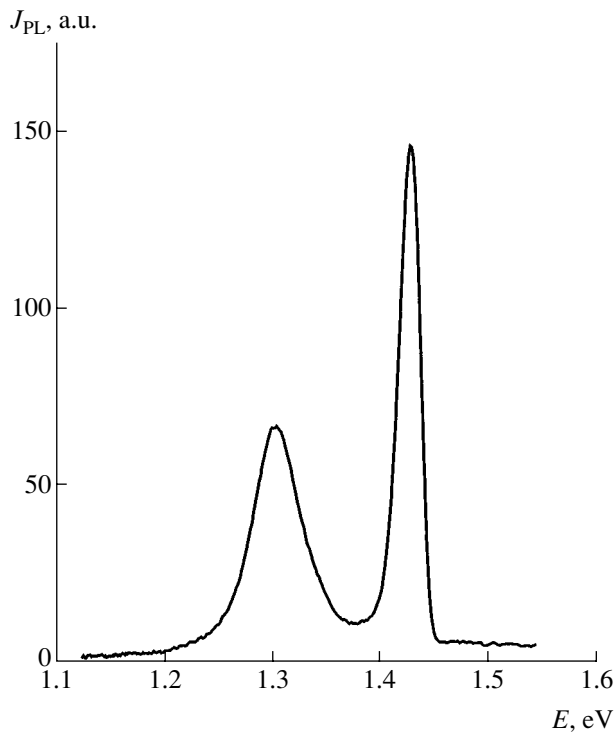

Fig. 2. PL spectrum of a InGaAs/GaAs heterostructure with 10 layers of QDs measured at 4 K.

metalorganic vapor phase epitaxy technique. The QD and interlayer growth procedure is described in detail elsewhere [15]. The QD layers were selectively doped by depositing 2-nm-thick δ:Si layers beneath each QD layer. Analysis of the transmission electron microscopy images of the transverse section of the heterostructure showed that QDs had a height of 3 nm and a lateral size of 20 nm. A characteristic feature of the structures under consideration is the presence of a clearly pronounced wetting layer. The results of photolumines-

cence (PL) measurements (Fig. 2) confirmed a high quality of crystal structure in the wetting layer (the peak intensity of PL from the wetting layer exceeds that from QDs) and provided information on the energy states in the quantum well formed by the wetting layer. At $T = 4.2$ K, the energy of the main transition in the wetting layer differs by 100 meV from the bandgap width of GaAs; the PL line width was about 20 meV.

The lateral transport was studied in a sample structure doped to 1.2×10^{11} cm^{-2} for each QD layer, which corresponds to two to four electrons per QD. For this reason, all QDs are populated at low temperatures and a considerable fraction of electrons occur in the wetting layer. This provides for the absence of electron freezing even at the lowest temperatures employed.

Results. Figure 3 shows the temperature dependence of the sample resistance R and the surface density of electrons determined as $n_H = 1/eR_H$, where e is the electron charge and R_H is the Hall coefficient. In the temperature interval from 8 to 30 K, the resistance exhibits a strong (nearly exponential) temperature dependence, $R = R_0 \exp(T_0/T)$, where $T_0 = 29$ K. This dependence is even stronger than that observed [16] for the lateral transport in InAs/GaAs heterostructures with QDs, $\sim \exp(T_1/T)^{1/3}$, which corresponded to the Mott law for the hopping conductivity (the peak of PL from the wetting layer was not observed in [16]). Since the Hall coefficient R_H and the electron density n_H in this temperature interval varied rather slightly (Fig. 3), the change in the resistance was accompanied by an analogous (nearly exponential) change in the Hall mobility.

Application of a magnetic field perpendicular to the sample surface gave rise to a negative magnetoresistance (Fig. 4, curve *2*) characteristic of the weak localization effects. For a magnetic field applied along the surface, we observed the usual positive magnetoresistance (Fig. 4, curve *1*). We believe that the observed anisotropy of the magnetoresistance confirms the assumption concerning a 2D character of the electron transport in the temperature interval studied.

Discussion. As the temperature is increased in the entire interval studied (1.5–40 K), a certain fraction of electrons trapped in QDs is transferred to the ground state in the wetting layer, while their thermal ejection from this layer is low probable. Since a change in the total density of free electrons is small (because of a high doping level), the observed considerable variation of the resistance is indicative of changes in the scattering of 2D electrons or in the conditions of their localization at random potential fluctuations in the wetting layer. In the wetting layer, 2D electrons exhibit strong Coulomb scattering on charged QDs. We attribute a sharp increase in the Hall mobility $\mu_H(T)$ of 2D electrons in the quantum well formed by the wetting layer to a decrease in the number of effectively scattering charged QDs as a result of their neutralization upon thermal ejection of bound electrons caused by increasing temperature. A similar effect was considered
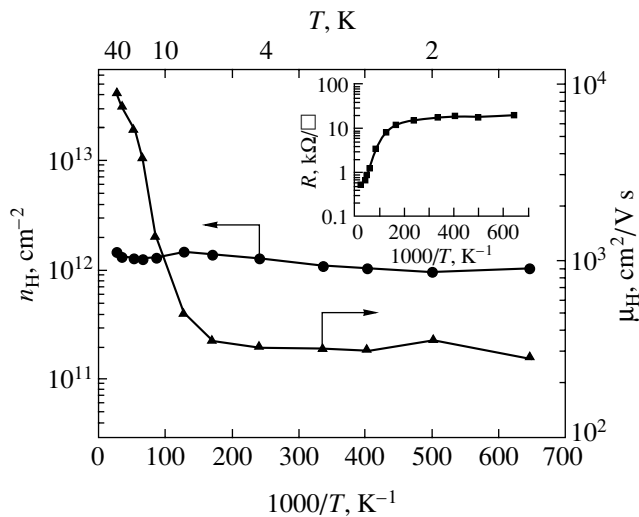
Fig. 3. The temperature dependence of the surface electron density n_H and the Hall mobility μ_H in a InGaAs/GaAs heterostructure with 10 layers of QD. The inset shows the temperature dependence of the sample resistance R.

Fig. 4. Magnetoresistance of a InGaAs/GaAs heterostructure with 10 layers of QD in a magnetic field oriented (*1*) parallel and (*2*) perpendicularly to the sample surface.

in [12–14] for 2D electrons in the channels of heterojunctions near QD layers. On the other hand, analogous behavior of $\mu_H(T)$ was observed for 2D carriers in the inversion channels at the $Si–SiO_2$ interface [17] in the interval of temperatures $T = 1.5–8$ K. This behavior was explained by the localization of carriers in the 2D channel on the random potential fluctuations related to the oxide charging. In the QD–wetting layer system, charged QDs play the same role as do the charges in SiO_2. However, the QD structures exhibit a significant difference from the $Si–SiO_2$ structures, which is related to a change in the number of charged QDs depending on the temperature. Apparently, the two possible explanations presented above for the observed behavior of $R(T)$, $n_H(T)$, and $\mu_H(T)$ are equiprobable.

It should be emphasized that, for the lifetime of photoexcited electrons exceeding the momentum relaxation times (which is characteristic of the structures with QDs), the same temperature dependence takes place for the effective mobility of photoexcited electrons. The photoexcitation of carriers from QDs under the action of IR radiation will give rise to a significant photocurrent due to a change in the effective mobility even at small variations in the total density of free electrons. The maximum variation of mobility in the QD structures studied was observed in the interval of temperatures from 8 to 30 K. In the same interval, we have previously observed the maximum IR photosensitivity [15] of the given structure with QDs. We believe that this coincidence is not accidental; preliminary discussion of the photoconductivity mechanism can be found in [15].

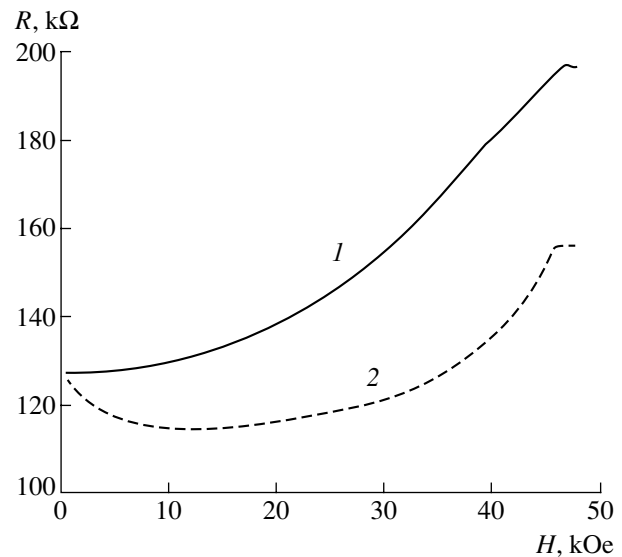It should be noted that in this study we deal with a structure in which the wetting layer plays the role of a 2D channel. Evidently, analogous effects must be observed in the IR detectors with additionally formed 2D channels and a deeper potential well. We believe that, by varying the band structure in such quantum dot–quantum well structures, it is possible to expand toward higher temperatures the interval in which the proposed photoconductivity mechanism is operative.

Conclusions. We have studied the phenomena related to the lateral electron transport in multilayer selectively doped InGaAs/GaAs heterostructures with QDs. It was demonstrated that the electron transport in these structures in the region of temperatures from 1.5 to 40 K proceeds via 2D channels formed by the wetting layers. As the temperature increases from 8 to 40 K, the electron mobility exhibits exponential growth at a slight increase in the electron density, which is related to a decrease in the influence of random scattering fields of charged QDs as a result of their neutralization. Using this mechanism, it is possible to provide for a significant increase in the sensitivity of IR photodetectors employing QD structures with lateral electron transport in comparison to the systems featuring the well-known concentration mechanism of photoconductivity.

REFERENCES

1. E. Finkman, S. Maimon, V. Immer, *et al.*, Phys. Rev. B **63**, 045323 (2001).
2. S. Maimon, E. Finkman, G. Bahir, *et al.*, Appl. Phys. Lett. **73**, 2003 (1998).

3. H. C. Liu, M. Gao, J. McCaffey, *et al.*, Appl. Phys. Lett. **78**, 79 (2001).

4. D. Pan, E. Towe, and S. Kennerly, Appl. Phys. Lett. **75**, 2719 (1999).

5. D. Pan, E. Towe, and S. Kennerly, Appl. Phys. Lett. **73**, 1937 (1998).

6. S. Kim, H. Mohseni, M. Erdtmann, *et al.*, Appl. Phys. Lett. **73**, 963 (1998).

7. J. Phillips, K. Kamath, and P. Bhattacharya, Appl. Phys. Lett. **72**, 2020 (1998).

8. S.-V. Lee, K. Hirakawa, and Y. Shimada, Physica E **7**, 499 (2000).

9. L. Chu, A. Zrenner, G. Bohm, and G. Abstreiter, Appl. Phys. Lett. **76**, 1944 (2000).

10. L. Chu, A. Zrenner, M. Bichter, and G. Abstreiter, Appl. Phys. Lett. **79**, 2249 (2001).

11. L. Chu, A. Zrenner, D. Bougeard, *et al.*, Physica E **13**, 301 (2002).

12. H. Sakaki, G. Yusa, T. Someya, *et al.*, Appl. Phys. Lett. **67**, 3444 (1995).

13. C. Metzner, G. Yusa, and H. Sakaki, Superlattices Microstruct. **25**, 537 (1999).

14. B. E. Kardynal, A. J. Shieds, M. P. O'Sullivan, *et al.*, Meas. Sci. Technol. **13**, 1721 (2002).

15. L. D. Moldavskaya, V. I. Shashkin, M. N. Drozdov, *et al.*, Physica E **17**, 634 (2003).

16. V. A. Kul'bachinskiĭ, R. A. Lunin, V. A. Rogozin, *et al.*, Fiz. Tekh. Poluprovodn. (St. Petersburg) **37**, 70 (2003) [Semiconductors **37**, 70 (2003)].

17. E. Arnold, Appl. Phys. Lett. **25**, 705 (1974).

Translated by P. Pozdeev